PROBING MICROPLASTIC DEFORMATION IN METALLIC MATERIALS

Thesis by

Xiaoyue Ni

In Partial Fulfillment of the Requirements for
the degree of
Doctor of Philosophy

CALIFORNIA INSTITUTE OF TECHNOLOGY
Pasadena, California

2018
(Defended October 4, 2017)

Xiaoyue Ni
ORCID: 0000-0002-1822-1122

ACKNOWLEDGEMENTS

Thanks to Caltech for hosting me for a happy PhD experience. I would like to thank my research advisor, Julia R Greer, who always stands by my side and supports me in every way. Her boundless trust has made my graduate life more enjoyable and fruitful than I would ever have asked.

Thanks also to my co-advisor, Rana Adhikari, who has provided me the chance to work on crackling noise projects with LIGO. I benefited a lot from all the rigorous trainings on scientific thinking he pushed me through, e.g. writing Elogs. My special gratitude to Gabriele Vajente, *an anonymous scientist from XX century*, who has spent endless amount of time mentoring me on almost everything about experimental physics with endless patience. He has been a role model for me in almost all aspects.

Thanks to all the past and present members of the Greer Group and LIGOX members for making my everyday life a blessing. Thanks to Xiaoxing Xia, Ottman Tertuliano, Alessandro Maggi, and Heng Yang, etc., who have made my time at Steele productive and entertaining through their ability to switch between in-depth scientific discussions and hear-to-heart conversations. I would like to thank Haolu Zhang for helping me wrap up my projects before graduation. Thanks to Seok-woo Lee and Zach Aitken for training me on nanoindentation and FIB. Very special thanks to Koji Arai for explaining locking loop and noise hunting in detail to me, and for all the surprising tricks and insightful suggestions I got from him. Thanks to Eric Quintero, Eric Gufstason, and Norna Robertson for always providing insightful suggestions and help at the crackle meetings. Thanks to the LIGO collaboration for all the intellectual and instrumental supports, for the pizza, coffee and donuts, and softball games. This thesis would not have been completed without the help and support of everyone in the group.

To my collaborator Prof. Stefanos Papanikolaou, Prof. James P. Sethna, Prof. Karin A. Dahmen, Dr. Danilo Liarte, and Prof. Sherry Xian Chen, thank you for all the discussions and Skype meetings in which I learned more than I ever wanted to know about materials, mechanics, and physics. I want to also thank Seiji Kawamura for all the useful discussions on crackling noise experiments.

Thanks to Chi Ma for the help with EBSD. Thanks to Prof. Sergio Pellegrino for allowing me to use the Instron loading frame in his group and to Yuchen Wei for helping with the

tests. I want to thank Bov Ann and Mike Roy for the help on all kinds of machining work. I want to thank everyone at Hysitron, especially for those who have taken my phone calls and provided real-time support when bad things happened.

I would like to thank my present and past roommates, Tingting Zhou, Liuyan Zhao, and Sijia Dong, for sharing either happy or sad moments with me. Thanks to my friends Yu Zhang, Qihui Zhao, Fengwan Wang, Shanshan Chen, Cong Wang, for always listening to me and making my holidays and vacations a great time. Lastly, I would like to thank my family, especially my parents Murong Li and Keqin Ni, for their endless love and understanding.

ABSTRACT

Metallic materials deform through discrete displacement bursts that are commonly associated with abrupt dislocation activities, *i.e.* avalanches, during plastic flow. Dislocations might be active prior to the textbook yielding, but it is unclear whether these activities can be discerned as smaller strain events, *i.e.* microplasticity. Novel experimental approaches involving nanomechanical experiments are developed to detect and to quantify microplastic deformation that occurs during compression of micron- and sub-micron sized single crystalline copper nano-pillars. The experiment, focusing on metals' pre-yield regime, reveals an evolving dissipation component in the storage and loss moduli that likely corresponds to a smooth transition from perfect elasticity to avalanche-dominated plastic deformation. This experimental investigation is corroborated by mesoscopic plasticity simulations, which apply to a minimal model that combines fast avalanche dynamics and slow relaxation processes of dislocations. The model's predictions are consistent with the microscopic experiments and provide constitutive relationship predicting microplastic crackling noise being upconverted by small stress perturbations. Another experimental investigation on unload-reload cyclic behavior of copper nano-pillars post yielding shows a decaying microplastic hysteresis with emergent power laws and scaling features, which signifies an ever-explored reversible-to-irreversible transitions in metal deformation, as seen in other nonequilibrium systems. To study microplasticity in macroscopic metallic samples, an instrument is custom-built based on Michelson interferometer and achieves unprecedented high displacement noise resolution of $10^{-14}\mathrm{m}/\sqrt{\mathrm{Hz}}$ in the frequency range of 10 – 1000 Hz. The macroscopic experiment has resolved a driving-modulated microplastic noise in bulk cantilever steel

samples under nominal elastic loading. The characteristics of the noise resemble those of the microplastic noise predicted from the micromechanical simulations developed from microscopic experiments.

PUBLISHED CONTENT AND CONTRIBUTIONS

Xiaoyue Ni, Stefanos Papanikolaou, Gabriele Vajente, Rana X Adhikari, and Julia R. Greer (2017). "Probing microplasticity in small-scale FCC crystals via Dynamic Mechanical Analysis". In: *Phys. Rev. Lett.* 18.155501. doi:10.1103/PhysRevLett.118.155501.
X.N. participated in the conception of the project, took the measurements, prepared and analyzed the data, ran the simulations, and participated in the writing of the manuscript.

Xiaoyue Ni, Haolu Zhang, Danilo Liarte, Louis W. McFaul, Karin A. Dahmen, James P. Sethna, Julia R. Greer (Submitted). "Precursor dislocation avalanches in small crystals: the irreversible transition".
X.N. participated in the conception of the project, took the measurements, analyzed the data, and participated in the writing of the manuscript.

James P. Sethna, Matthew K. Bierbaum, Karin A. Dahmen, Carl P. Goodrich, Julia R. Greer, Lorien X Hayden, Jaron P. Kent-Dobias, Edward D. Lee, Danilo B. Liarte, **Xiaoyue Ni**, Katherine N. Quinn, Archishman Raju, D. Zeb Rocklin, Ashivni Shekhawat, and Stefano Zapperi (2017). "Deformation of crystals: Connections with statistical physics". In: *Annu. Rev. Mater. Res.* 47:14.1–14.30. doi:10.1146/annurev-matsci-070115-032036
X.N. participated in the writing of the manuscript.

Xiaoyue Ni, Gabriele Vajente, Eric Quintero, Koji Arai, Eric Gustafson, Norna Robertson, Julia R. Greer and Rana X Adhikari (In preparation). "Experimental characterization of crackling noise in microplastic regime of bulk metallic materials".
X.N. participated in the conception of the project, co-built the experimental setup, took the measurements, analyzed the data, and participated in the writing of the manuscript.

Gabriele Vajente, Eric Quintero, **Xiaoyue Ni**, Koji Arai, Eric Gustafson, Norna Robertson, Julia R. Greer and Rana X Adhikari (2016). "An instrument to measure mechanical up-

conversion phenomena in metals in the elastic regime". In: *Rev. Sci. Instr.* 87, 065107. doi:10.1063/1.4953114.

X.N. participated in the conception of the project, co-built the experimental setup, and participated in preparing the data the writing of the manuscript.

Xiaoyue Ni, Julia R. Greer, Kaushik Bhattacharya, Richard D. James, and Xian Chen, (2016). "Exceptional Resilience of Small-Scale $Au_{30}Cu_{25}Zn_{45}$ under Cyclic Stress-Induced Phase Transformation". In: *Nano Lett.*, 16 (12), pp 7621–7625. doi: 10.1021/acs.nanolett.6b03555.

X.N. participated in the conception of the project, performed the experiments, took the measurements, and participated in the writing of the manuscript.

TABLE OF CONTENTS

FIGURE AND TABLE LIST

Chapter 1: Introduction

1.1 Summary

Microplasticity is firstly defined in a macroscopic context in Section 1.2.1 as the pre-yield non-linear deviation from the linear behavior of metallic materials below the *yielding stress*, which, in the textbook description, strictly separates the irreversible plastic regime from the reversible elastic regime of deformation. The evidence for the presence of microplasticity can be found in many traditional mechanical behaviors of bulk metallic materials, such as creep and fatigue (Section 1.2.2), internal friction (Section 1.2.3), and Bauschinger effect (Section 1.2.4).

In order to study the microscopic physics of microplasticity, Section 1.3 discusses the nature of dislocation-limited plasticity revealed in small-scale metals. Section 1.3.1 introduces the difference between macroscopic and microscopic metals deformation. Section 1.3.2 reviews the primary experimental methodology for small-scale study of dislocation plasticity – the uniaxial compression tests on single crystalline micro- and nanopillars. Section 1.3.3 examines the characteristics of microplasticity envisioned from the statistical physics point of view. The novelty and significance of the statistical study on dislocation avalanches are discussed in this subsection with a focus on their connections to microplastic deformation of metallic materials.

Section 1.4 discusses an important motivation of this thesis work, i.e. noise study for advanced LIGO. Section 1.4.1 introduces some background, *i.e.* how advanced LIGO works and why mechanical noise can be a problem. Section 1.4.2 introduces the basics

of Michelson interferometer configuration, based on which advanced LIGO achieves ultra-high differential displacement resolution. The interferometry methodology also serve as the basis for the macroscopic experimental study on microplasticity.

1.2 Microplasticity in Macroscopic Deformation of Metals

1.2.1 Engineering Yielding and Dislocation Plasticity

Metallic materials are used in many mechanical systems. It is normally assumed that they behave elastically, that is, the exhibited strain is proportional to the applied stress. The mechanical behavior follows Hookean relationship due to stretching of atomic bonds. Upon elastic loading, there is no permanent shape change and the deformation is completely and instantaneously recoverable. However, elastic loading cannot go forever. Irreversible deformation of the materials, signified by a non-linear deviation in the mechanical response, occurs when loading exceeds certain limit. Polycrystalline materials, which include most metal and metal alloys, show more strain with incremental stress beyond the elastic regime, a behavior called plastic deformation. Figure 1.1 (a) shows a schematic of the stress-strain response for typical polycrystalline materials. The distinction between elasticity and plasticity is not crisp. The loading stress separating the two regimes, i.e. the *yield stress*, is conventionally defined by a 0.2% strain offset criterion as illustrated in Figure 1.1 (a).

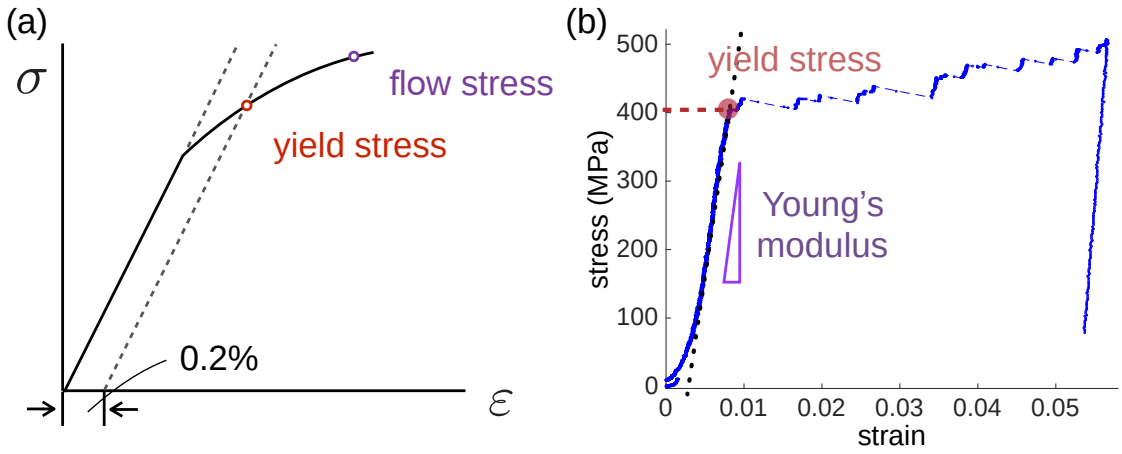

Figure 1.1 The stress-strain response of quasi-static uniaxial compression tests on metallic materials. (a) An illustration of typical mechanical response of polycrystalline materials, (b) Sample compression test data for a single-crystalline copper nanopillar (with diameter of 500 nm and nominal aspect ratio of 3:1).

Early on, Frenkel (1924) assumed that the plastic deviation is caused by shearing of atomic planes off each other[1]. Based on this assumption, the estimated yield strength $\tau \approx \frac{\mu}{2\pi}$, where μ is the shear modulus of the materials, turns out to be order of magnitudes (~100x) larger than the experimental observations. Later, Polayni[2], Taylor[3], and Orowan[4] (1934) independently found that the flow of dislocations – the topological disjunctions in periodic lattices – should be responsible for the 'weaker-than-expected' strength observed experimentally in crystalline materials. These lattice mismatches act as weak spots that can easily carry strain by hopping mechanism. The deformation picture of metallic materials therefore has to incorporate the complex behavior of dislocation flow rather than simple atomic-bond stretching and breaking.

The dislocations were first mathematically described by two vectors. One is the burger vector $\boldsymbol{b}$ describing the resulting displacement in a perfect lattice because of the presence of a dislocation, and the other is the sense vector $\boldsymbol{\xi}$. The dislocations shear under stress.

The stress can be both external and internal. In the simplest case, an applied uniaxial loading stress σ is projected to a resolved shear stress τ_{rss} acting on the dislocation as $\tau_{rss} = m\sigma$. The project factor $m = \cos(\theta)\cos(\phi)$ is the *Schmid factor*, where θ and ϕ are the angles between the loading direction and the Burgers vector and the slip plane normal. The force acted on the dislocation per unit length is τb. A more general expression for the force $\boldsymbol{F}_1$ acting on a dislocation with sense vector $\boldsymbol{\xi}_1$ and burger vector $\boldsymbol{b}_1$ induced by an arbitrary stress σ_{ij} is known as the *Peach-Kohler formula*,

$$\boldsymbol{F}_1 = \boldsymbol{\xi}_1 \times (\sigma_{ij} \cdot \boldsymbol{b}_1). \tag{1.1}$$

The stress can also be internal. Dislocation and dislocation interact through the elastic field induced by lattice distortion due to their presence. The internal interactions of dislocations play crucial role in deformation process of bulk metallic materials. For example, it leads to the plain-old *Taylor hardening* explanation for work hardening[1], that is, the flow stress of a metallic sample increases over deformation simply because of an increase in dislocation density – the dislocations have to overcome stronger mutual elastic interaction to be able to move through the more clustered network. The stress required to force two dislocations with spacing l to pass each other against their interaction is $\tau = \alpha Gb/l$, where α is a constant, G is the shear modulus, and b is the magnitude of burger vector. For a network with dislocation line density ρ, the spacing between dislocations can be approximated as $l \sim \rho^{-1/2}$. The hardening stress will simply increase with the dislocation density,

$$\tau \sim \alpha Gb\sqrt{\rho}. \tag{1.2}$$

The Taylor hardening explanation is clearly over simplified, but it reveals the important role the complex collective behavior of dislocations can play in plastic deformation.

With the presence of dislocations, an authentic elastic deformation of crystal lattices (recoverable and instantaneous) under finite applied stress is questionable. This suspicion is reinforced by the ambiguity in the definition of engineering yielding. Prior to this arbitrarily defined threshold stress, there could be nonlinear deviation from elastic-linear deformation behavior due to dislocation activities. From high-resolution extensometry, etch-pit studies, or x-ray topography, signatures of micro-deformation have been reported at stresses significantly below the engineering yield stress in bulk single crystalline materials[5–8], but the microscopic physics of these emergent pre-yield deformation have not been well-captured[9,10].

The characteristics of microplasticity are not only of importance to improve the precise functional materials design. They also provide a pathway to resolve the defect ensemble evolution while the material is approaching a 'failure' transition, which can result in in-depth understanding of the microscopic origins of plasticity, or other macroscopic mechanical properties of metallic materials involving non-linear dislocation activities under small stress or stress perturbation.

1.2.2 Creep and Fatigue

Plastic strain that occurs at low stress has been studied in the context of *creep* and *fatigue* in metals. Under macroscopic stress below the critical stress, dislocations can overcome

the bowing stress threshold occasionally and move infrequently due to thermal or athermal excitations. In thermal creep, the fraction of 'active' dislocations decreases over time, corroborated by the observation that the creep rate dies away quickly under constant stress and temperature[4,11]. In fatigue test, damage accumulates over cyclic loading and can finally lead to catastrophic failure of the materials[12].

Both creep and fatigue can be viewed as the manifestation of the microplasticity in metallic materials over long-term. The tests do not resolve microscopic pre-yield dislocation activities but an accumulation of the infinitesimal microplastic strains.

1.2.3 Internal Friction

Plasticity is usually associated to energy dissipation. Under elastic stress excitations (usually at high frequencies), metallic materials exhibit internal friction (IF)[13]. IF is energy dissipation associated with deviation from Hooke's Law, and usually manifested as stress-strain hysteresis in cyclic loading. IF is usually measured as energy loss factor $Q^{-1} = \frac{\Delta W}{2\pi W}$, where ΔW is the energy dissipated per cycle and W is the maximum elastic energy stored during a cycle.

In the fully recoverable regime, *Anelastic Relaxation* mechanisms are considered to be the main source of IF. Anelasticity manifests as a formation of a closed loop in mechanical response upon unloading and is typically modeled by standard linear solid composed of ideal (Hookean) elastic solid component, a spring with stiffness *k*, and an ideal (Newtonian) liquid component, a dashpot with damping factor η. Anelastic relaxation usually occurs when the cyclic driving amplitude is small. Since there is a relaxation time-

scale associated to the dynamics, the energy dissipation has a frequency dependent peak at critical damping. The underlying mechanism of anelasticity is found to be point defect, dislocation, interface, or thermo-elastic related relaxation [13].

Dislocation-Related Amplitude-Dependent Internal Friction (ADIF) is a non-linear damping mechanism, which is amplitude-dependent, and frequency independent, and is more relevant in the aspect of stress-modulated mechanical noise. This type of hysteretic behaviors were reported to occur in the plastic regime. The amplitude dependence can be very sensitive to the microstructures of the sample, which makes it difficult to collect data with meaningful statistics to compare between different ADIF studies.

1.2.4 Bauschinger Effect

Polycrystalline material commonly exhibits hysteresis behavior due to *Bauschinger effect* (BE): the dislocations pile up at internal interfaces under loading, forming stable cell structure, but will slip back upon reverse loading with aid of backstress[14]. BE is usually observed when loading direction is reversed. In the uni-directional loading, stress ratcheting[15,16] has been observed in polycrystalline materials, or other experiment on single-crystalline metals but with the presence of large strain gradients, such as torsion of micron scale metallic wires[17]. In the uni-directional and uniaxial loading tests on macroscopic single crystals, little or no recoverable plasticity was found, except for specific small-scale systems with unusual microstructures such as passivated thin-films and nanopillars[18–20], freestanding nanocrystalline film[21,22], or pentatwinned silver nanowires[23]. Unidirectional BE is usually named “anomalous” or “unusual” BE.

There is no good explanation why unidirectional BE does not show up ubiquitously in crystal deformation. From a microscopic view, under an arbitrary hardening stress, some dislocations can be marginally stable due to their complex long-range interactions. During unloading the local backstress can become large enough to facilitate reverse motion of these dislocations[24,25]. Reversible plasticity might be a subgroup of pre-yield microplasticity that has not been resolved or examined carefully.

1.3 Microplasticity in Small Scale Mechanics

1.3.1 Dislocation Limited Plasticity in Small-scale Metals

Mechanical deformation of materials is usually described by smooth stress-strain relations; for examples, see textbook Ref[26,27] and an illustration in Figure 1.1 (a). For a long time, the plastic dislocation flow in metals was considered fundamentally continuous and deterministic. Acoustic emission tests have pioneered in resolving stochastic and discrete events in macroscopic samples. The *acoustic emission* (AE) tests on single-crystalline ice have revealed intermittent sound events at resolved shear stress far below the yielding stress[28]. In the experiments with ice, high signal to noise ratio is achieved by freezing the microphones into the sample to obtain necessarily rigid mechanical contact, and acoustic signals due to dissipation events not correlated with dislocation activities, like micro-cracks, can be distinguished by investigating the transparent bulk of the sample. The results obtained from this methodology is size and materials-wise limited.

Uchic et al. first applied the uniaxial compression methodology on focused ion beam (FIB)-machined Ni micro-pillars[29]. Greer and Nix then extended it to Au nanopillars[30], and since then the discrete and stochastic nature of plasticity, manifested as the step-like

serrations in the loading curves shown by the sample stress-strain data from Ni micro-pillars[31], has been ubiquitously observed in small-scale single-crystalline metals, with smaller samples exhibiting higher stresses [31–34].

The emergent size effect in strength has been studied in the framework of dislocation starvation[35], which is on the contrary to the Taylor hardening mechanism in bulk metallic materials (see Section 1.2.1, Equation 1.2). This source-limited strengthening[36] has mainly been attributed to the unique nanoscale plasticity mechanisms, where the operation of individual dislocation sources, single arm or surface, governs deformation and strength[37,38].

These serrations in deformation found their origin in the stochastic nature of dislocations, where these large intermittent events have been intensively studied in small scale as dislocation avalanches, that is the slip of one dislocation triggers sequent slips of other dislocations, like a domino effect. In large sample, avalanches exhibit smaller size fluctuations[39,40] and the large number of avalanche events will be globally smoothed. In micromechanical tests, the coherent drive on a small number of dislocations allows the large local stochastic strain bursts to be observed. The revealed dislocation dynamics in small-scale plasticity is not trivial and highly nonlinear.

The in-situ TEM indentation on micron-sized Al grains and compression on 160 nm diameter Ni pillars show incipient dislocation motion upon loading, way before any discernible strain events are triggered[36,41]. These microplasticity events should be reflected in the loading curve but they are buried in machine noise. The in-situ TEM cyclic loading test shows dislocations healing through constant low amplitude stress cycles[24].

The in-situ TEM observations are insightful regarding preyield dislocation activities, but the conclusion is limited to a small-scale system – the sample has to be small enough to allow electron transparency. A constitutive relation characterizing microplastic stress-strain response needs to be applied and tested in macroscopic samples.

1.3.2 Uniaxial Compression Experiments

Uniaxial compression on FIB machined small-scale single crystalline <111> orientated copper is chosen to be the primary experimental methodology for dislocation plasticity study for multiple reasons. First of all, the uniaxial loading on single crystalline crystals prohibits the presence of strain gradients. FCC crystals are an easy-glide system: with the well-defined slip planes the dislocation dynamics can be reduced to a 2-dimensional problem. The <111> oriented FCC crystal is loaded in the high-symmetry direction, where multi-slips are simultaneously excited to avoid single-slip-induced unidirectional-displaced surface steps that can foster stress concentration and promote a bending mode during the plastic deformation. The sample is limited to small-scale pillars with submicron or few-micron diameters with a relatively small number of mobile dislocation sources. Last but not the least, the specific system – <111> orientated single crystalline copper nanopillars – has been intensively studied in earlier work[42,43], and benchmarked with microstructural characterization, materials properties, and mechanical behaviors under quasi-static displacement- and load-controlled loading conditions for comparison and sanity check.

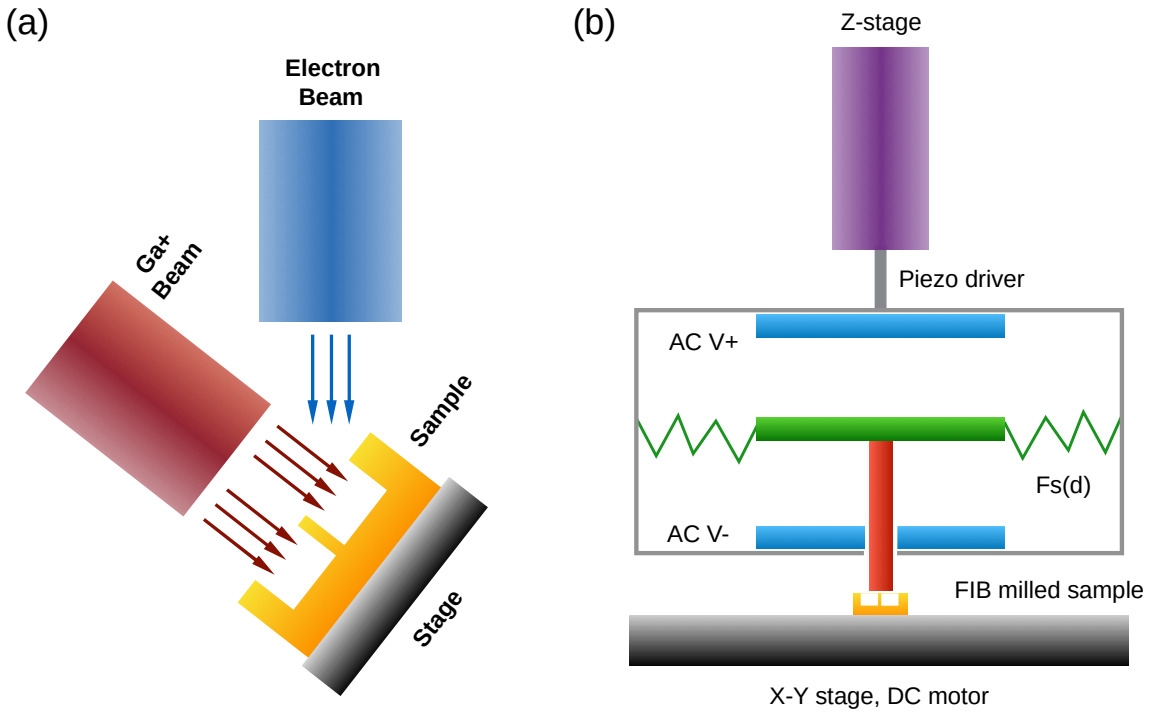

Figure 1.2 Schematics demonstrating the fabrication process and nanomechanical testing. (a) Nanopillar samples are fabricated via Focused Ion Beam (FIB) milling. (b) The Hysitron nanoindenter transduces voltage to a force applied to the sample via the three-plate assembly and measures the displacement of the tip mounted on the central plate through antenna.

The micro- or nanopillars were machined by Focused Ion Beam (FIB) with FEI dual-beam (high voltage electron beam for imaging and ion beam for milling) Versa 3D instrument, as illustrated in Figure 1.2 (a). The pillars with an aimed aspect ratio of 3:1 are fabricated following a concentric-circles top-down methodology using a Galium ion beam[40,44,45] under operative voltage of 30 kV. The samples are milled from a bulk single crystalline sample (>99.9999% purity) with one side polished to a <30 Å rms roughness, oriented in <111> direction. The ion current starts with 5 nA for outer-rings milling, and is reduced in steps to 30 pA for the final finish-up in order to minimize gallium ion implantation to the pillars and the sidewall tapering issue. Although it is known that FIB can introduce surface damage to the pillars by forming small dislocation loops or an amorphous layer[46],

the deformation mechanism of small-scale fcc metals are dominantly determined by the initial microstructure rather than the fabrication technique[42].

The nano-compression experiments were carried out in a nanoindenter (Triboindenter, Hysitron) equipped with a custom-made flat punch 8 μm-diameter diameter diamond tip. Figure 1.2 (b) is a schematic illustration of the transducer assembly in a three-plate configuration. The tip is mounted to the charged central plate. The central plate is suspended by compliant leaf springs. Alternate-current (AC) voltages with equal amplitudes are applied to the upper and lower plates 180 degree out of phase for independent measurement of central-plate displacement. An additional direct-current (DC) voltage is applied to the lower plate to drive the central plate via capacitive force.

The tip alignment with respect to the sample stage is carefully calibrated to ensure centered contact with sample surface and uniaxial loading. For nanomechanical testing, the instrumental drift is a commonly present problem. The nanoindenter assumes a constant drifting rate throughout single test and actuate to correct for it accordingly. The drift rate is measured as the displacement rate of tip with a 2 μN load held on the sample surface.

1.3.3 Statistical Physics in Crystal Deformation

In nanomechanical experiments on single crystalline micro- or nanopillars, large strain bursts are unambiguously distinguished as serrations in the stress-strain curves as shown in Figure 1.1 (b). The extent of these strain bursts usually ranges from nanometers to a few microns[29,31,47–49]. The analysis of strain bursts shows that the slip size distributions follow power laws spanning orders of magnitudes:

$$D(S) \sim S^{-\kappa}, \tag{1.3}$$

where S denotes the slip size. κ is the universal scaling exponent and is found to be $\kappa = 1.5$ [28,50]. The emergent power-law and scaling indicate that dislocations in crystals at yielding transition are a driven nonequilibrium system, which shares similarities with other nonequilibrium systems exhibiting *crackling noise* such as magnetics, charge density waves, and earthquakes[25,51].

Plastic deformation of crystals has been described by a depinning picture[52,53], in which dislocations can be pinned at random defect points that are randomly distributed throughout the sample. These defect points serve as quenched pinning sites and attribute threshold stresses locally to the dislocations. The dislocation can depin and slip when the total stress acted on it exceeds the pinning threshold. Under external loading, dislocation lines are driven though pinning disorders. The driving force, long-range coupling force, and local pinning force together on the dislocations compete in a complex manner. The dislocations behave collectively as elastic manifold undergoing depinning transition and produce scale-invariant avalanches[54,55].

The depinning description of crystal deformation is challenged by a jamming picture, in which intermittent strains can arise with no presence of immobile pinning sites, but from mutual long-range elastic interactions of dislocations, *i.e.* dislocations can jam themselves through entanglements and behave collectively[28,56–58]. The dislocation dynamics simulation based on the jamming mechanism shows that the same scaling of strain bursts holds for very small stresses far below the yielding threshold[59], and that the cyclic stress

with stress amplitude smaller than the yield stress can excite intermittent events at stress peaks[60].

A minimal micromechanical model has predicted a stress-tuned critical behavior in crystal plasticity: the power-law slip size distributions are shown to have stress-dependent cutoffs,

$$D(S) \sim S^{-\kappa} f_S\left[S(\tau_c - \tau)^{1/\sigma}\right], \tag{1.4}$$

where $\kappa = 1.5$, $\sigma = 0.5$, τ_c is the critical failure stress, and $f_S(x)$ is an exponentially decaying universal scaling function[61]. The proposed stress-tuned criticality has been validated in micromechanical experiments by analyzing the large post-yield avalanche size distribution[47]. It is unclear whether smaller strain bursts, undetected by the instrument, are present in the deformation of such micro- and nanosized single crystals, especially prior to the yield point, which is commonly defined as the start of the first detected burst.

1.4 Macroscopic Experiment

1.4.1 Mechanical Noise in Advanced LIGO

The mechanical noises induced by dislocation slips can be a potential source of noise for instruments that require ultra-high strain resolutions, for example, the Advanced Laser Interferometer Gravitational-wave Observatory (LIGO) detectors[62,63].

Advanced LIGO aims to detect gravitational wave signal using Michelson Interferometer techniques[64] (For details about the basics of Michelson Interferometer, see Section 1.4.2). A gravitational wave propagating to the detector can squeeze and stretch the space during one half-cycle of the wave, which has an effect of lengthening one Michelson arm and

shortening the other. Split laser beams travel through the two 4 km arms and recombine at the beam splitter. In an ideal configuration, the gravitational wave differential strain induces a phase shift between the two interfering beams that can be detected by the photodetectors a laser power change.

Advanced LIGO has aimed and achieved an ultra-high strain resolution on an order of $10^{-22}/\sqrt{\text{Hz}}$ near the frequency of the signal detection (20-2000 Hz), that is, a displacement resolution of order $10^{-19}\text{m}/\sqrt{\text{Hz}}$ at the low frequency end of the range (10-20 Hz)[64]. In order to achieve the unprecedented strain resolution, all sources of environmental or instrumental noises that can induce differential displacement of the Michelson arms have to be considered. For example, seismic noise can couple to the Michelson signal through asymmetry of the interferometer. The test masses (TMs, the end mirrors of the Michelson Interferometer) are suspended by a quadruple pendulum (QUAD) for horizontal isolation and three stages of maraging steel for vertical isolation[65], as shown in Figure 1.3. The suspension system gives ~ 10 billion times suppression of the ground motion in the high frequency regime. However, below the last stage of maraging steel blades, called the upper intermediate mass (UIM), there is no more spring blade damping. Any mechanical noise arising in the UIM subjected to the residual seismic modulation can propagate down to the TM, couple to its horizontal motion through earth curvature, and give rise to noise that can contaminate the gravitational wave signal.

.

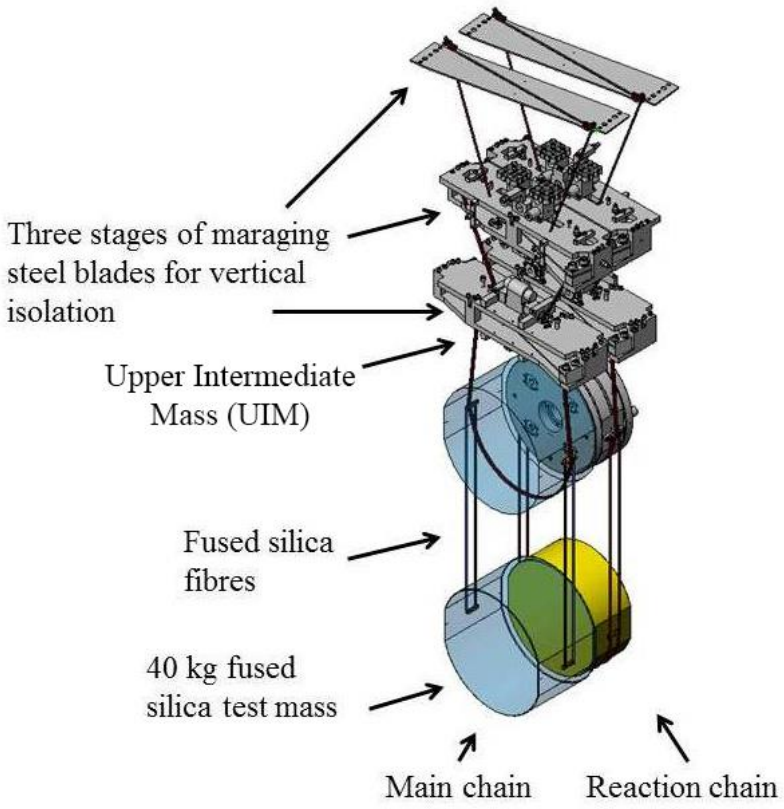

Figure 1.3 The aLIGO test mass suspension system consists of a quadruple pendulum incorporating 3 stages of maraging steel cantilever springs. Drawing adapted from Ref. [65].

A major part of this thesis work is devoted to address the following questions about this potential mechanical noise: first, the existence of this type of noise is hypothetical – Does mechanical noise rise in the bulk metals' elastic functioning regime? If so, how does the noise depend on external stress? What is the magnitude of this noise reflected in advanced LIGO sensitivity? These questions can be potentially addressed by advanced experiments with ultra-high displacement sensitivity.

1.4.2 Michelson Interferometer Configuration

Advanced LIGO bases its detection on Michelson Interferometer configuration. Figure 1.4 demonstrates a simplified scheme of Michelson Interferometer. The beam entering

from the symmetric port is divided by the beam splitter into two parts, reflected by the end mirrors, and existed from symmetric and asymmetric ports.

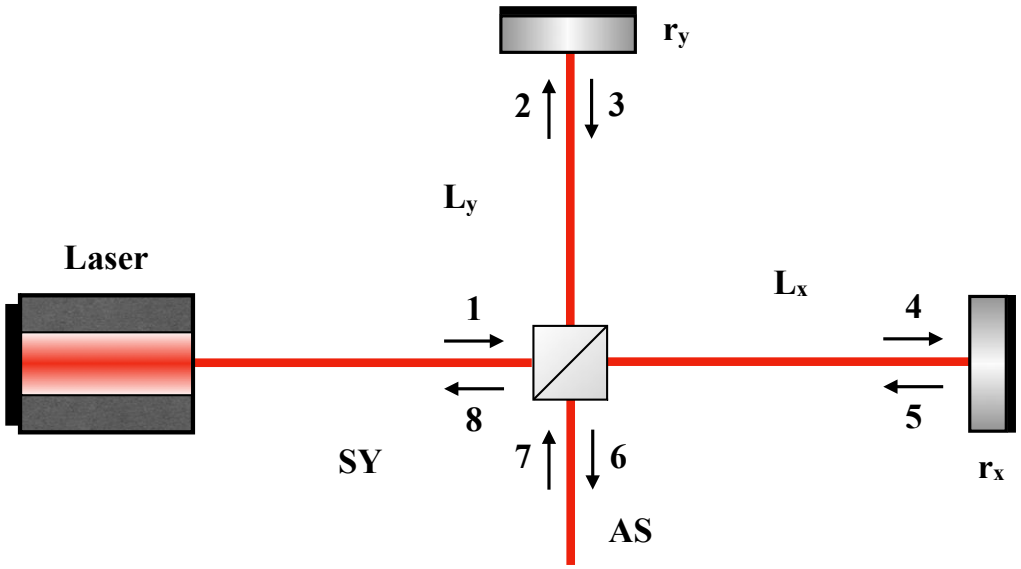

Figure 1.4 Simplified schematics of a typical Michelson interferometer configuration indicating field propagations through symmetric (SY) and asymmetric (AS) arms.

Following the convention of field representations, the reflected and transmitted beams can be expressed given the incoming beam ψ_{input}, reflectivity r, and transmissivity t,,

$$\psi_r = ir\psi_{input}, \tag{1.5a}$$

$$\psi_t = t\psi_{input}. \tag{1.5b},$$

The beam propagating through the two Michelson arms can be tracked from the input beam $\psi_{input} = \psi_1$. The fields at the asymmetric (AS) and symmetric (SY) ports, $\psi_{AS} = \psi_6$, $\psi_{SP} = \psi_8$ can be calculated,

$$\psi_{AS} = -\psi_1\left(e^{-2i\kappa x_1} r_1\sqrt{r_{BS}}\sqrt{t_{BS}} + e^{-2i\kappa x_2} r_2\sqrt{r_{BS}}\sqrt{t_{BS}}\right), \tag{1.6a}$$

$$\psi_{SY} = i\psi_1\left(e^{-2i\kappa x_1} r_1\sqrt{t_{BS}}\sqrt{t_{BS}} - e^{-2i\kappa x_2} r_2\sqrt{r_{BS}}\sqrt{r_{BS}}\right), \tag{1.6b}$$

where r_{BS} and t_{BS} are the reflectivity and transmissivity of the beam splitter; the degrees of freedom can be reduced by exploiting the relation $t_{BS} = 1 - r_{BS}$. κ is the wavenumber of input laser. r_1 and r_2 are reflectivity of end mirror 1 and 2. Ideally the reflectivity of two mirrors would be identical. In reality, they might defer by small amount,

$$r_1 = r + \frac{\delta r}{2}, \tag{1.7a}$$

$$r_2 = r - \frac{\delta r}{2}. \tag{1.7b}$$

Similarly, x_1 and x_2, the beam path lengths of the two Michelson arms, can have different values,

$$x_1 = x + \frac{\delta x}{2}, \tag{1.8a}$$

$$x_2 = x - \frac{\delta x}{2}. \tag{1.8b}$$

The photodetector has no sensitivity to any phase information but only the beam power. Substituting everything,

$$I_{AS} = \psi_{AS}\psi_{AS} = \psi_1\psi_1(1 - r_{BS})r_{BS}[\delta r^2 + (4r^2 - \delta r^2)\cos^2(\kappa\delta L)], \tag{1.9a}$$

$$I_{SY} = \psi_{SY}\psi_{SY} = \frac{1}{4}\psi_1\psi_1[(2r + \delta r - 2r_{BS}\delta r)^2 - 4(4r^2 - \delta r^2)(1 - r_{BS})r_{BS}\cos^2(\kappa\delta L)]. \tag{1.9b}$$

From the above equations for beam power, the contrast defect $C = I_{min}/I_{avg}$ can be calculated with varying δL, by knowing that $\cos^2(\kappa\delta L) \in [0,1]$ and $< \cos^2(\kappa\delta L) > = \frac{1}{2}$:

$$C_{AS} = \frac{\delta r^2}{\delta r^2 + \frac{1}{2}(4r^2 - \delta r^2)}$$

$$= \frac{2\delta r^2}{\delta r^2 + 4r^2}, \qquad (1.10a)$$

$$C_{SY} = \frac{(\delta r + 2r - 2r_{BS}\delta r)^2 - 4(4r^2 - \delta r^2)(1 - r_{BS})r_{BS}}{(\delta r + 2r - 2r_{BS}\delta r)^2 - \frac{1}{2}4(4r^2 - \delta r^2)(1 - r_{BS})r_{BS}}$$

$$= \frac{\left(\delta r + 2r(1 - 2r_{BS})\right)^2}{(\delta r + 2r)^2(1 - 2r_{BS}) + 2(\delta r^2 + 4r^2)r_{BS}^2}\ . \qquad (1.10b)$$

The differential signal d is the differential variation, $\delta L = \delta L_0 + d$. The common mode signal c is $L = L_0 + c$. As such, the sensitivity, or the *optical gain*, for differential and common mode signals are $\frac{dI_i}{d\delta L}$ and $\frac{dI_i}{dL}$, where i represents either the antisymmetric or symmetric ports. I_i has no dependence on dL, which means that theoretically the rejection for the common mode signal is perfect. Then the sensitivity g_i for the differential displacement signal dL becomes,

$$g_{AS} = \frac{dI_{AS}}{d\delta L} = -I_{input}\kappa(4r^2 - \delta r^2)(1 - r_{BS})r_{BS}\sin(2\kappa\delta L), \qquad (1.11a)$$

$$g_{AS} = \frac{dI_{SY}}{d\delta L} = I_{input}\kappa(4r^2 - \delta r^2)(1 - r_{BS})r_{BS}\sin(2\kappa\delta L)\,. \qquad (1.11b)$$

Using Equation (1.9a, 1.9b) and based on the error propagation theory, how the input laser power noise, *a.k.a.* laser intensity noise[66], is coupled to the Michelson signal can be computed as,

$$\frac{\delta I_{AS}}{\delta I_{input}} = \frac{I_{AS}}{I_{input}}$$
$$= (1 - r_{BS}) r_{BS} [\delta r^2 + (4r^2 - \delta r^2) \cos^2(\kappa \delta L)], \quad (1.12a)$$

$$\frac{\delta I_{SY}}{\delta I_{input}} = \frac{I_{SY}}{I_{input}}$$
$$= \frac{1}{4} [(\delta r + 2r - 2r_{BS}\delta r)^2 - 4(4r^2 - \delta r^2)(1 - r_{BS}) r_{BS} \cos^2(\kappa \delta L)]. \quad (1.12b)$$

For frequency noise coupling[66], the noise goes in as a fluctuation of the wave number $\kappa = 2\pi\nu/c$, where ν is the laser frequency and c denotes speed of light,

$$\delta I_{AS} = \frac{\partial I_{AS}}{\partial \kappa} \frac{\partial \kappa}{\partial \nu} \delta \nu$$
$$= -\frac{2\pi}{c} I_{input} \delta L (4r^2 - \delta r^2)(1 - r_{BS}) r_{BS} \, sin(2\kappa \delta L) \delta \nu = g_{AS} \delta L \frac{\delta \nu}{\nu}, \quad (1.13a)$$

$$\delta I_{SY} = \frac{\partial I_{SY}}{\partial \kappa} \frac{\partial \kappa}{\partial \nu} \delta \nu$$
$$= \frac{2\pi}{c} I_{input} \delta L (4r^2 - \delta r^2)(1 - r_{BS}) r_{BS} \, sin(2\kappa \delta L) \delta \nu = g_{SY} \delta L \frac{\delta \nu}{\nu}. \quad (1.13b)$$

Divided by its corresponding optical gain g_i, the signal can be converted to an equivalent displacement noise. Conventionally, the laser intensity or frequency noise are represented in percentage form,

$$\delta(\delta L)_i = \frac{I_i}{g_i} \left(\frac{\delta I_{input}}{I_{input}} \right) + \delta L \left(\frac{\delta \nu}{\nu} \right). \quad (1.14)$$

If all optical elements in the interferometer configuration are ideal, that is, the reflectivity equals the transmissivity of the beam splitter $r_{BS} = t_{BS} = \frac{1}{2}$, and the end mirrors have perfect reflectivity, $r_1 = r_2 = 1$, the fields can be rewritten in terms of the sum and difference of the arm lengths,

$$\psi_{AS} = -\psi_i \left(\frac{e^{-2i\kappa x_1} + e^{-2i\kappa x_2}}{2} \right) = i\psi_i e^{-ik(x_1+x_2)} \sin\big(\kappa(x_1 - x_2)\big), \qquad (1.15a)$$

$$\psi_{SY} = -\psi_i \left(\frac{e^{-2i\kappa x_1} - e^{-2i\kappa x_2}}{2i} \right) = \psi_i e^{-ik(x_1+x_2)} \cos\big(\kappa(x_1 - x_2)\big). \qquad (1.15b)$$

How the optical gain varies with different parameters, *i.e.* Michelson balance tuning δL, input laser power I_{input}, difference in end mirror reflectivity δr, and beam splitter reflectivity r_{BS}, can be numerically investigated. Default values are set for the simulation parameters as shown in Table 1.1.

I_{input}	λ	r_{BS}	r_{avg}	δr	δL
10 mW	1064 nm	0.5	0.9	0.0	$\pm\frac{1}{8}\lambda$

Table 1.1 Default parameter values for Michelson Interferometer configuration simulation.

Based on the default set of parameters, the optical gain can be simulated using Equation (1.11a) and (1.11b). Figure 1.5 shows how the optical gain changes versus each parameter tuning.

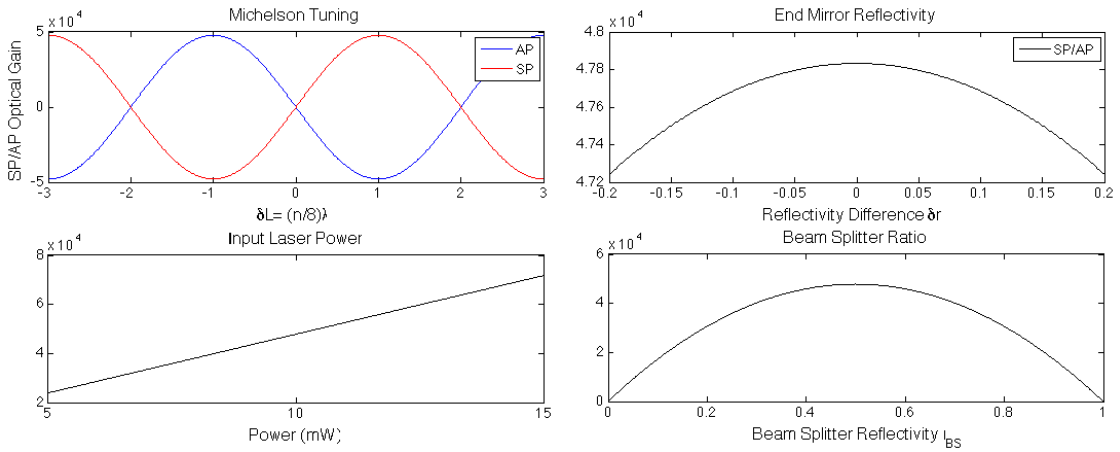

Figure 1.5 Simulation results showing how the optical gain g_i changes with different Michelson parameters, *i.e.* Michelson balance tuning, difference in end mirror reflectivity, input laser power, and beam splitter reflectivity.

with all other parameters held constant, tuning the microscopic length difference δL of the two arms gives interference fringes at both ports. The bright fringe tuning is set to $-\lambda$ for symmetric and $+\lambda$ for asymmetric ports. Independently, the end mirror reflectivity difference is tested from -0.2 to 0.2, input laser power from 5 to 15 mW, and beam splitter reflectivity from 0 to 1; the corresponding optical gain variations with the expected trend or symmetry are shown in Figure 1.5.

1.5 Objectives and Outline

Existing experiments studying microplastic deviations from a perfect elastic behavior in metals usually apply to a quasi-static loading condition. The work in this thesis focuses specifically on the microplastic events that can be excited by prescribed slow-varying stress perturbations. No such mechanically up-converted noise has been explicitly resolved far below the conventionally-defined yield stress. The first question is whether the noise can be unambiguously detected and quantified.

One consequential interest of this thesis work is to investigate the physics and mechanism of microplasticity. Is microplastic deformation simply smaller plastic deformation? Does microplasticity serve as a precursor to elastic-to-plastic or other sorts of failure transitions?

Another intriguing direction is to study microplasticity across the scale. Acoustic emission (AE) tests have resolved large dissipation events in macroscopic metallic samples[67–72], which have been correlated to dislocation dynamics in the plastic regime[71], but the experimental resolution is yet high enough to resolve small pre-yield events like those observed in the ice samples[28,73]. One interesting question is whether the microplastic events studied in the small-scale metals would show up in the bulk metallic samples as a simple statistical averaging from stacks of microscopic-volume response.

This thesis is devoted to answer the questions raised above and is outlined as follows: Chapter 1 gives a review of the former studies that are closely related to microplasticity behavior of metallic materials. Chapter 2 discusses the explicit probing of microplastic deformation in the pre-yield regime of single-crystalline copper nanopillars. Chapter 3 extends the discussion of microplasticity to the post-yielding regime. Chapter 4 switches gears and investigates microplasticity in the bulk metallic materials using interferometry techniques. Chapter 5 concludes the thesis with final remarks and suggestions of future work.

Chapter 2: Microplasticity in Small-Scale Crystals

As introduced in Chapter 1, in small-scale metallic systems, collective dislocation activity has been correlated with size effects in strength and with a step-like plastic response under uniaxial compression and tension. Yielding and plastic flow in these samples are often accompanied by the emergence of multiple dislocation avalanches. Dislocations might be active preyield, but their activity typically cannot be discerned because of the inherent instrumental noise in detecting equipment. Alternate current load perturbations via dynamic mechanical analysis are applied during quasistatic uniaxial compression experiments on single crystalline Cu nanopillars with diameters of 500 nm and compute dynamic moduli at frequencies 0.1, 0.3, 1, and 10 Hz under progressively higher static loads until yielding. By tracking the collective aspects of the oscillatory stress-strain-time series in multiple samples, an evolving dissipative component of the dislocation network response that signifies the transition from elastic behavior to dislocation avalanches in the globally preyield regime is observed. Microplasticity, which is associated with the combination of dislocation avalanches and slow viscoplastic relaxations, is postulated to be the cause of the dependency of dynamic modulus on the driving rate and the quasistatic stress. A continuum mesoscopic dislocation dynamics model is constructed to compute the frequency response of stress over strain and obtain a consistent agreement with experimental observations. The results of the experiments and simulations present a pathway to discern and quantify correlated dislocation activity in the preyield regime of deforming crystals.

2.1 Introduction

Using basic forms of mechanical loading, such as a force- or displacement-controlled compression, careful examination of the data provided evidence for the presence of short plastic instabilities before the onset of the obvious and apparent strain bursts [9,42,43,47,49], e.g., 100–400 MPa regime of 500 nm copper pillars, as shown in Section 1.2.1, Figure 1.1 (b). The higher yield stress observed in small-scale samples compared to their macroscopic counterparts can be understood in terms of dislocation starvation, where upon compression, the initially present mobile dislocations have a higher probability of annihilating at a nearby free surface than multiplying or being entangled with other dislocations[35,74]. This dislocation source exhaustion mechanism might involve preyield dislocation activities. In situ transmission electron microscope (TEM) nanoindentation experiments revealed the onset of dislocation motion before the first obvious displacement excursion[36,41]. In situ Laue microdiffraction work with micron-sized Ni sample showed that a dislocation structure forms at ~0.65 of the yield stress and continues to develop until global yielding is reached[75]. Creep experiments on single crystals of ice detected acoustic emission events at resolved shear stresses far below the yield stress[28,73]. These observations have yet to be connected to constitutive relations and a quantifiable stress-strain response. Discrete dislocation dynamics (DDD) simulations suggest the existence of intermittent events in the preyield regime of crystalline materials[59,60] and a significant loading rate effect on strain burst response of nano- and microcrystals due to dislocation jamming and relaxation[76]. Stress-induced probabilistic cross-slip relaxation has also been associated with several nontrivial aspects of crystal plasticity[77]. It is natural to question whether microplasticity be detected and quantified in crystals' preyield regime.

Machine noise has been the Achilles' heel of numerous experimental nanomechanical investigations. Attempts have been made to characterize the machine noise, with reported values of ~0.2 nm displacement-, ~30 nN force- noise floor, and a thermal drift of < 0.05 nm/s for the prevalently used Hysitron TI 950 Triboindenter in quasistatic mode. In uniaxial compression experiments, a flat nanoindenter tip applies compressive load to the top of a commonly cylindrical sample, a so-called micro- or nanopillar, and the indenter-sample friction, as well as the electromagnetic assembly responsible for the load control produce substantial and inevitable machine noise. In addition, noise caused by thermal drift sets a limit on the duration of such experiments, which renders long-time mechanical experiments like cyclical or fatigue loading, as well as creep tests virtually impossible to interpret. Statistical probing is necessary to detect any possible nonlinear dislocation activities, which cause axial displacements below the machine noise. Dynamic mechanical analysis (DMA) is applied at multiple frequencies that span three orders of magnitude, from 0.1 to 10 Hz, on multiple 500 nm-diameter single crystalline Cu nanopillars. The overall DMA behavior is statistically characterized and compared with mean- field dislocation depinning predictions.

2.2 Experimental Methodology

2.2.1 Nanomechanical Testing

500 nm diameter single-crystalline copper samples are prepared following the sample fabrication procedure described in Section 1.3.2. The nanomechanical experiments were carried out in a nanoindenter (Triboindenter, Hysitron) introduced in Section 1.3.2. Figure 2.1 (a) conveys a representative compressive engineering stress-strain data, with the inset

showing the corresponding time series of load and displacement, zoomed into the preyield regime. In the experiment, a uniaxial quasistatic load that monotonically increased in a stepwise fashion is applied to an individual nanopillar. Small stress oscillations with the amplitude of 6 μN and a fixed frequency in the range between 0.1 and 10 Hz were superimposed over the static load to each 15-s step interval.

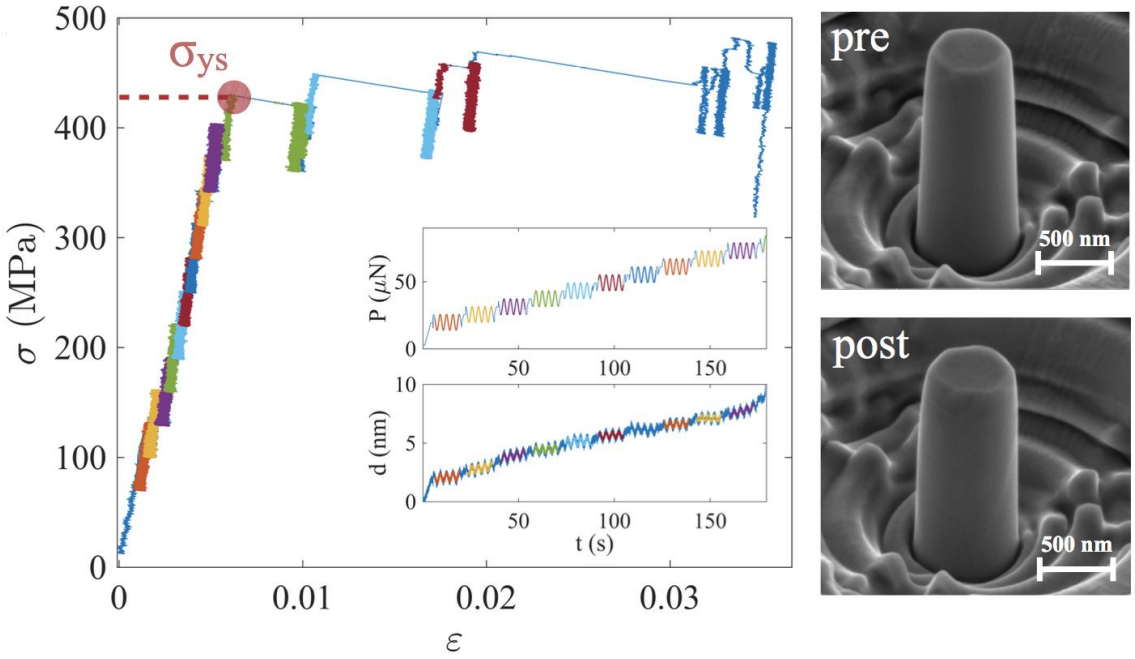

Figure 2.1 Dynamic mechanical analysis on Cu nanopillars. (a) Engineering stress vs strain during DMA measurements on a Cu sample at a frequency of 0.3 Hz. (b) SEM images of an as-fabricated (pre-) and compressed (post-) ~500 nm diameter Cu pillar with a nominal aspect ratio of 3∶1. Figure reprinted with permission from [X. Ni, et al. *Phys. Rev. Lett.* 118, 155501 (2017)] Copyright (2017) by the American Physical Society.

Before the initiation of each compression experiment, the stages and piezo drive are settled for more than 145 s in order to equilibrate the in-contact displacement drift and the last 20-s drift data is used to estimate the thermal drift rate for subsequent correction. Only those experiments where the thermal drift rate was less than 0.05 nm/s were analyzed. The

loading time before the occurrence of the first large strain event was usually within the first 200 s for all tests. Figure 2.1(b) shows the representative pre- and post- compression SEM images of a representative Cu nanopillar.

2.2.2 Dynamic Mechanical Analysis

The dynamic modulus is defined as the frequency response of stress over strain $\mathrm{E}(\omega, \sigma_0) = \sigma(\omega)/\varepsilon(\omega)$, where σ_0 is the applied quasistatic stress and $\omega = 2\pi f$ is the driving frequency. Using this definition, extract the dynamic modulus can be extracted from the oscillations that are imposed at each quasistatic stress σ_0 using a frequency domain analysis.

The time series of stress $\sigma(t)$ and strain $\varepsilon(t)$ are fitted using the following form which also includes a linear drift term:

$$\sigma_f(t) = x_r \cos(\omega t) + x_i \sin(\omega t) + \sigma_d t + \sigma_0, \tag{2.1a}$$

$$\varepsilon_f(t) = u_r \cos(\omega t) + u_i \sin(\omega t) + \varepsilon_d t + \varepsilon_0, \tag{2.1b}$$

where $x_r, x_i, \sigma_d, \sigma_0, u_r, u_i, \varepsilon_d, \varepsilon_0$ are fitting parameters for the stress and strain. The complex dynamic modulus E can then be calculated as a function of the ω and σ_0,

$$E(\omega, \sigma_0) = \frac{x_r - i x_i}{u_r - i u_i} = A(\omega, \sigma_0) e^{i\phi(\omega, \sigma_0)}, \tag{2.2}$$

where A and ϕ are the amplitude and phase components of the dynamic modulus.

This type of DMA is applied with different driving frequencies (0.1, 0.3, 1, and 10 Hz) and measurements are taken from six samples for each frequency driving test. The

dynamic modulus can be solved at each quasistatic loading step at the single driving frequency using the fitting procedure described above. The quasistatic stress at each step is normalized by the yield stress of the system σ_{ys}. Amplitude and phase lag are binned in stresses for sample statistics. The binning average and standard error for amplitude and phase lag were calculated as a function of the stress bin centers and are shown for each driving frequency in Figure 2.1 (a). The DMA data reveal a maximum of ~70% decrease in the average amplitude and a maximum of ~60° increase in the average phase lag as the applied quasistatic stress approaches yielding at $\frac{\sigma_0}{\sigma_{ys}} = 1$ (~400 MPa).

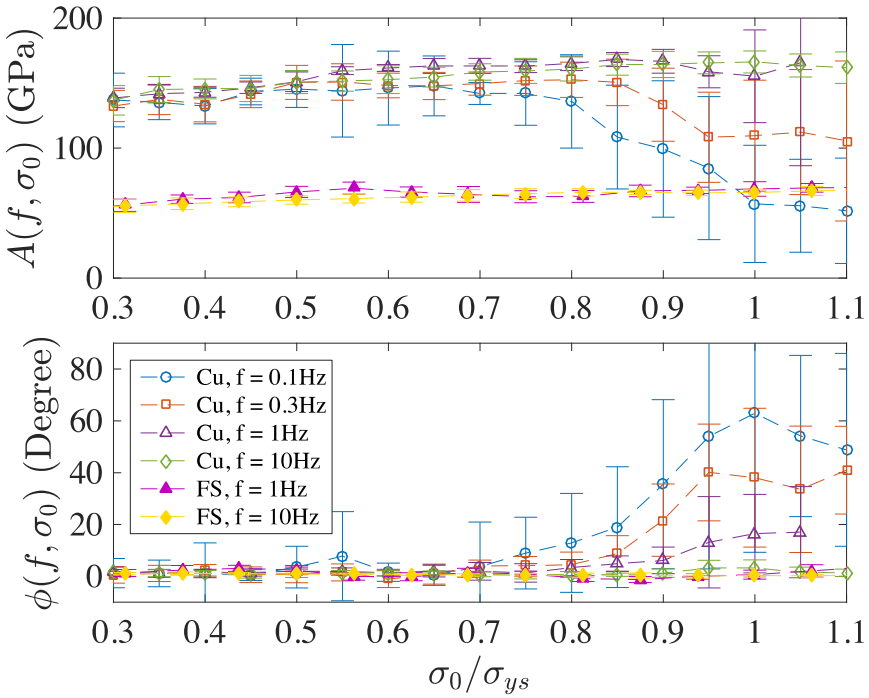

Figure 2.2 Dynamic modulus versus stress resolved from experiments. Figure reprinted with permission from [X. Ni, et al. *Phys. Rev. Lett.* 118, 155501 (2017)] Copyright (2017) by the American Physical Society.

This plot also shows that these deviations from elastic behavior are more pronounced for slower driving frequencies. These results are in stark contrast to the DMA data collected from the same type of uniaxial compression on a ~500 nm-diameter fused silica (FS) nanopillars, which exhibits a constant amplitude of ~65 GPa and a no-delay response for the driving frequencies of 1 Hz and 10 Hz.

The amorphous FS samples that are of the same pillar geometry but contain no dislocation sources are tested for calibration purpose. The FS nanopillars are fabricated by FIBing from bulk FS sample . A thin-layer of gold with a thickness of ~40 nm is deposited on the surface of the bulk FS for e-beam imaging. As shown in Figure 2.3 (a), the gold thin-film starts to delaminate from the sample surface after being exposed to the ion beam. Figure 2.3 (b) shows that no residual gold is left on the as-fabricated FS pillar.

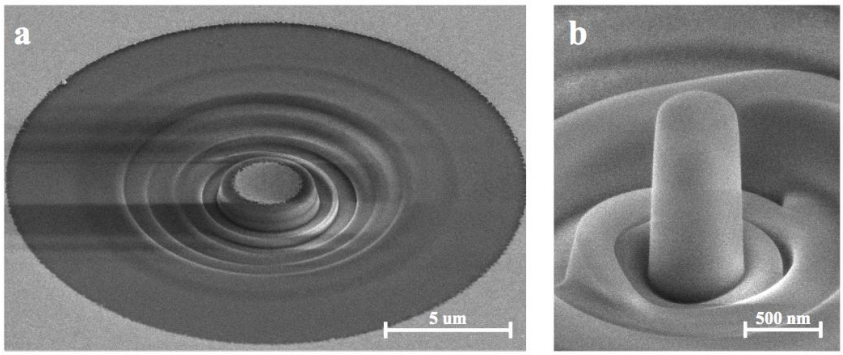

Figure 2.3 SEM images of a fused silica sample (a) during fabrication, and (b) after fabrication. The deposited gold thin-film completely delaminates from the sample surface.

The perfectly elastic DMA behavior of FS nanopillars serves as strong evidence that the observed nontrivial change in dynamic modulus with quasi-static stress in copper is related to dislocation dynamics.

2.3 Mesoscopic Plasticity Simulation

2.3.1 Modeling Framework

To reveal the underlying mechanisms that drive the observed nontrivial loss behavior in Cu as the applied stress approaches yielding, a continuum crystal plasticity model is constructed aiming at capturing the salient aspects of the observed mechanical behavior. This model considers the energetics of two competing processes: the dislocation-driven abrupt strain jumps and the slow stress-controlled relaxations towards minimum system energy state. To capture both the fast avalanches and the slow viscoplastic relaxations, a cellular automaton constitutive microplasticity model enhanced with an additional continuous-in-time strain field that follows a viscoplastic constitutive law is utilized[77–79]. The modeled shear strain consists of the elastic and plastic components $\gamma = \gamma_e + \gamma_p$. The elastic term is calculated using Hooke's law. The plasticity model that captures the plastic term can be realized using detailed continuum plasticity modeling approaches[26]. It is reasonable to assume that in a single representative volume element for single-crystalline fcc crystals, the following criteria hold: (i) uniaxial loading activates one dominant crystallographic slip system, A, with another system, B, assisting dislocation glide along A[1], and (ii) dislocations carry plastic distortion via two distinct mechanisms: (a) fast

[1] Although the bulk is nominally high-symmetry orientated, in a large deformation picture, the pillars would point towards dominant slip systems. The 〈111〉 orientation leads to a

dislocation avalanche-like glide and (b) slow, stress-relaxation-driven secondary glide on A caused by the coupled A-B dislocation mechanisms (e.g., double cross slip)[77]. With contributions from both mechanisms, the total plastic strain can be expressed as

$$\gamma_p = \gamma_p^{(a)} + \gamma_p^{(b)}. \tag{2.3}$$

In the fast dislocation avalanche-driven mechanism, a volume element at location $\boldsymbol{r}$ yields a random plastic strain $\delta\gamma_p^{(a)}$ if the local stress $\tau(\boldsymbol{r})$ is larger than a local depinning threshold $\chi(\boldsymbol{r})$ [31,40,41], where $\chi(\boldsymbol{r})$ follows a uniform distribution [42]. After each avalanche, the threshold value is redrawn from the same distribution. On the other hand, the slow relaxation mechanism follows a typical constitutive viscoplastic law,

$$\dot{\gamma}_p^{(b)} = \frac{D}{G}\big(\tau(\boldsymbol{r})\big)^n, \tag{2.4}$$

where D is the relaxation constant, G is the shear modulus, and $n \in [1, 3] < 10$ is the critical quantity to define another time scale which is slow compared to the fast avalanche process[43].

---

slip system with near zero resolved shear stress, leaving lots of dislocations that can function as the B slip system[42].

For numerical simplicity, this methodology is applied to edge dislocations only, for which the local resolved shear stress can be explicitly calculated as

$$\tau(\boldsymbol{r}) = \tau_{ext} + \tau_{int}(\boldsymbol{r}) + \tau_{hard}(\boldsymbol{r}), \tag{2.5}$$

where τ_{ext} is the applied external quasistatic stress combined with the oscillation component,

$$\tau_{ext} = \tau_0 + \tau_A \sin(\omega t), \tag{2.6}$$

and τ_{hard} is the stress that arises from dislocation hardening,

$$\tau_{hard}(r) = -h\gamma_p(\boldsymbol{r}). \tag{2.7}$$

where h represents a mean-field phenomenological hardening parameter[78–80].

τ_{int} is the stress that accounts for the long-range interactions with other dislocations,

$$\tau_{int}(\boldsymbol{r}) = \int d^2\boldsymbol{r}' K(\boldsymbol{r} - \boldsymbol{r}')\gamma_p(\boldsymbol{r}'), \tag{2.8}$$

where K serves as the interaction kernel for single slip straight edge dislocations. For the stress kernels of complete circular dislocation loops or screws, in principle, the results would be unchanged, since all these kernels are sufficiently long ranged[53,81].

2.3.2 Model Implementation

The model implementation is such that the system is meshed into N × N elements, with N = 32. Similar loading conditions are prescribed to eight random initial configurations as in the experiments, with different driving frequencies of 1, 2, 8, and 64 rad/s. The rate equation associated to Equation 2.3 can be numerically solved by Euler integration with

a fixed time step $\Delta t = 10^{-2}$s. The model assumes that a fast avalanche-driven channel $\gamma_p^{(a)}$ and a slow $\gamma_p^{(b)}$ contributes equally to the total plastic strain γ_p.

In the fast avalanche channel, a random depinning threshold $\chi(\boldsymbol{r})$ is assigned to each volume element at location $\boldsymbol{r}$. The value of each local threshold $\chi(\boldsymbol{r})$ is drawn from a uniform distribution in the range [0, 2] GPa. This phenomenological choice of threshold distribution will be argued in detail in Section 2.3.3. In the fast avalanche channel, for each time step, the local resolved stress $\tau(\boldsymbol{r})$ is compared to the local depinning threshold $\chi(\boldsymbol{r})$. Whenever $\tau(\boldsymbol{r}) > \chi(\boldsymbol{r})$, the local volume will yield a plastic strain $\delta\gamma_p = \varepsilon$. For each depinning event, the strain burst size ε is a random number drawn from a uniform distribution in the range [0, b], where b is the magnitude of the burger vector. The volume element will keep yielding until $\tau(\boldsymbol{r}) \leq \chi(\boldsymbol{r})$.

The slow relaxation channel is described by Equation 2.5. The relaxation rate is expected to be of order 10^{-6}~10^{-4} s^{-1} for FCC single crystals[37,77,82]. Relaxation constant *D* in for the copper nanopillar system is found to be ~ 10^{-4} s^{-1} via a parametric study in Section 2.3.3. The shear modulus G of copper has a value of ~ 70 GPa[83]. The strain-rate sensitivity exponent n = 1 is set for the simplest generalized case[77].

Deformation in single slip system considers the slip in x direction, slip planes normal to y axis, and strain field independent of z. The internal stress accounts for the long-range interactions with other dislocations in two dimensions[79,80] as,

$$\tau_{int}(\boldsymbol{r}) = \int d^2\boldsymbol{r}' K(\boldsymbol{r} - \boldsymbol{r}')\gamma_p(\boldsymbol{r}')$$

$$= C \int d^2\boldsymbol{r}' \left[\frac{1}{(\boldsymbol{r}-\boldsymbol{r}')^2} - \frac{8(x-x')^2(y-y')^2}{(\boldsymbol{r}-\boldsymbol{r}')^6} \right] \gamma_p(\boldsymbol{r}'), \tag{2.9}$$

which can be calculated in Fourier space in the simulations,

$$\tau_{int}(\boldsymbol{k}) = -C\gamma(\boldsymbol{k}) \frac{k_x^2 k_y^2}{|\boldsymbol{k}|^4}. \tag{2.10}$$

The coupling coefficient C, which decides the strength of long-range internal interactions amongst volume elements, is found to be 8000 GPa according to a direct comparison between simulation and experimental results in Section 2.3.3.

The phenomenological hardening parameter *h* in Equation 2.7 to is set to be 0.14 GPa[77]. For the external stress, 20 compressive stress steps from 100 to 500 MPa are prescribed, with constant driving amplitude 30 MPa and oscillation interval of 15 s, as in the experiment. The resolved shear dynamics on a single slip system e.g. (111)⟨011⟩ is considered. Eight random initial configurations are simulated for each of the four different driving frequency tests at 1, 2, 8, and 64 rad/s with a fixed time step of 0.01 s. A smaller time step of 0.001 s doesn't generate significantly different results.

2.3.3 Parameter Settings

The effects of three important parameters are investigated in simulation: 1. the distribution $P(\chi)$ of local depinning threshold χ, 2. the coupling coefficient C, and 3. the relaxation time scale D.

With a constant relaxation rate $D = 10^{-4}$ s^{-1} and a single-frequency oscillation at 2 rad/s, the effect of the threshold distribution $P(\chi)$ is empirically studied in the quasi-static limit.

For simplicity, the distribution is assumed to be uniform over an interval $[0, \chi_{max}]$[84]. Whether a specific form of the distribution will play a role is beyond the scope of this study. As demonstrated in Figure 2.4, if all other parameters are held constant but the upper bound of the threshold distribution χ_{max} is changed, the global yield stress σ_{ys} of a configuration will change accordingly – a higher cap of the threshold distribution can lead to a 'stronger system'. In Figure 2.4 the inset shows the measured σ_{ys} vs. the prescribed χ_{max} and a linear relationship is observed, which is as expected since the avalanche-driven plasticity is controlled by the Heaviside function $\Theta(\tau - \chi)$.

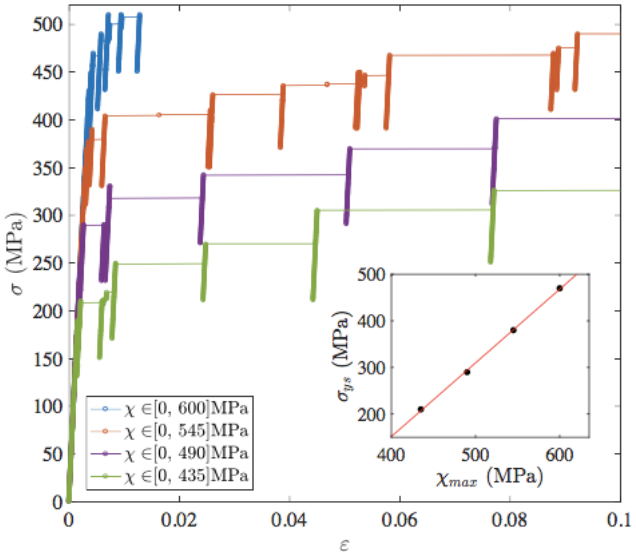

Figure 2.4 Sample simulation results with different threshold distribution $P(\chi)$. The figure shows stress-strain relations that demonstrate the effect of the threshold distribution on the quasi-static behavior of the system. The inset shows a linear fit for the measured yield stress vs. the prescribed distribution upper bound χ_{max}.

The coupling coefficient C determines how 'collective' the slip events are. To demonstrate this, quasi-static behavior of systems with different coupling strength spanning three orders of magnitude, from ~ 103 to 105 GPa, are simulated for comparison.

The larger C is correlated to a weaker system that globally yields at a lower stress, but the empirical parameter χ_{max} can be adjusted to compensate for the change in system strength as described previously, while all other parameters are kept constant.

Figure 2.5 shows the stress vs. strain response of three systems with C = 1.2 × 103, 3.5 × 104, 1.0 × 105 GPa, where different threshold distribution with χ_{max} = 250, 550, 2500 MPa are used correspondingly to maintain the global yield stress at ~ 400 MPa. From the sample simulation results, a smaller C can be associated to a more homogenous and deterministic plastic behavior, while the systems with larger C deform through more stochastic and collective strain bursts. A typical experimental quasi-static behavior is shown in the Figure 2.5 inset. For a direct comparison between simulation and experiment the collectiveness is quantified as the cutoff size of strain bursts present during the test. Setting the value of C to be 8000 GPa (with χ_{max} = 300 MPa) pro- vides good agreement between simulated and experimental data. Nevertheless, the DMA results are insensitive to the choice of coupling coefficient in a wide range from ~101 to ~104 GPa. Considering only the quasi-static limit behavior, in order to reproduce the experimental results, the threshold distribution range and the coupling coefficient can be tuned to adjust the nominal yield stress of the system and the degree of collectiveness to match the one measured in experiments.

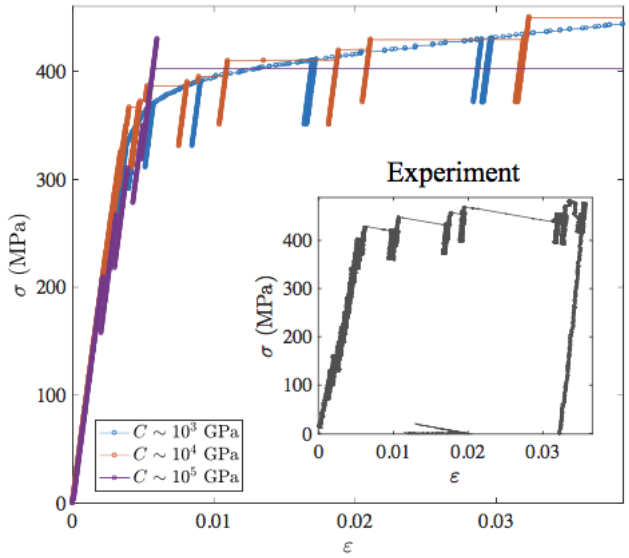

Figure 2.5 Sample simulation results with different coupling strength. The figure shows representative simulated stress vs. strain relations using different coupling coefficient C from~103 to105 GPa. χ_{max} is scaled for to keep each system yield globally at ~400 MPa. The results are compared with the inset experimental stress vs. strain response during DMA measurements at a frequency of 0.3 Hz.

Figure 2.6 presents the stress-strain relation and DMA analysis of the simulation data with zero relaxation D = 0, along with three different D values that span three orders of magnitude. The set of simulations uses the same uniform threshold distribution in the range [0, 550] MPa. Small oscillations at frequency 2 rad/s are superimposed to each stress hold. The main figure shows that the relaxation rate does not affect the quasi-static response. Systems with different relaxation constant yield globally at the same compressive stress σ ~ 400 MPa. Figure 2.6 inset shows the single-frequency DMA analysis at 2 rad/s. In the limit D = 0, the dynamic modulus amplitude is independent of the quasi-static stress level, and the phase is zero throughout loading, whereas finite relaxation is related to the dissipation mechanism – a larger relaxation rate is shown to be associated with a more significant decrease in amplitude and increase in phase under

modulation. In tuning the simulation parameters to obtain a system close to the experimental observation, the relaxation constant D controls the AC dissipation behavior of the system that can be quantitatively characterized by the DMA analysis.

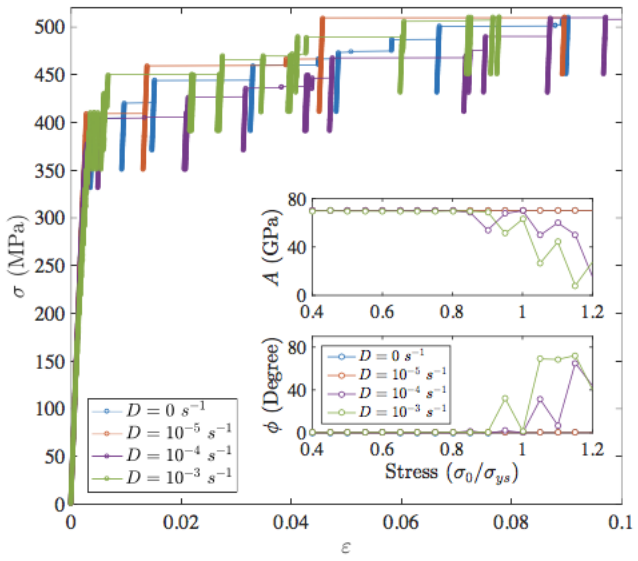

Figure 2.6 Sample simulation results with different relaxation rate. The figure shows representative stress-strain relations of systems with different relaxation constant D from 0 to $10^{-3}s^{-1}$. The inset compares the DMA analysis of the simulation results with different relaxation constant D.

The final choice of the simulation parameters is based on an agreement between simulation and experimental results, in both quasi-static and AC limit, achieved by tuning the upper bound of the uniform threshold distribution $P(\chi)$, coupling coefficient C, and the relaxation constant D.

2.4 Results and Discussions

2.4.1 Elastic-to-Plastic Transition

Figure 2.7 shows the same frequency domain analysis of the dynamic modulus using simulation results like the ones shown in Figure 2.2 for the experimental data.

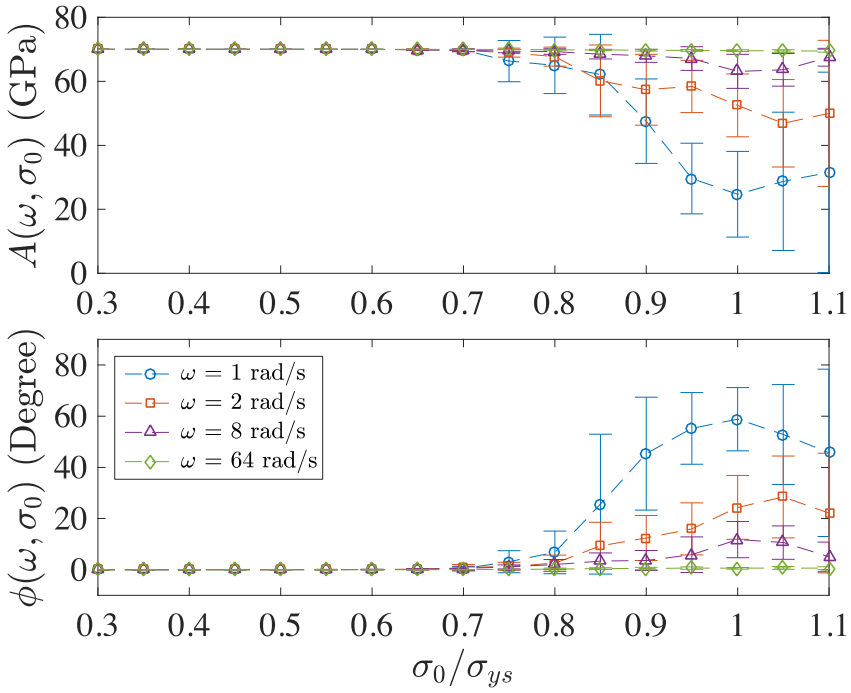

Figure 2.7 Dynamic modulus versus stress resolved from simulations. Figure reprinted with permission from [X. Ni, et al. *Phys. Rev. Lett.* 118, 155501 (2017)] Copyright (2017) by the American Physical Society.

The qualitative agreement between simulations and experiments motivates further quantitative comparison. Existing simulations investigated the effect of cyclic loading on the evolved dislocation network and predicted a scaling relation between the normalized strain rate amplitude and the driving frequency, focused on the mean-field depinning theory framework[60,85],

$$\frac{|\dot{\varepsilon}|}{|\sigma|} \sim \omega^{\kappa}, \tag{2.11}$$

where $\kappa = 1$ corresponds to a simple harmonic oscillator, *i.e.*, perfectly elastic behavior, and $\kappa = 0.82$ corresponds to a system driven close to the pinning threshold χ. The strain rate amplitude is normalized by the stress amplitude $\frac{|\dot{\varepsilon}|}{|\sigma|}$, which is equivalent to $\frac{\omega}{A}$, where A is the dynamic modulus amplitude measured via DMA.

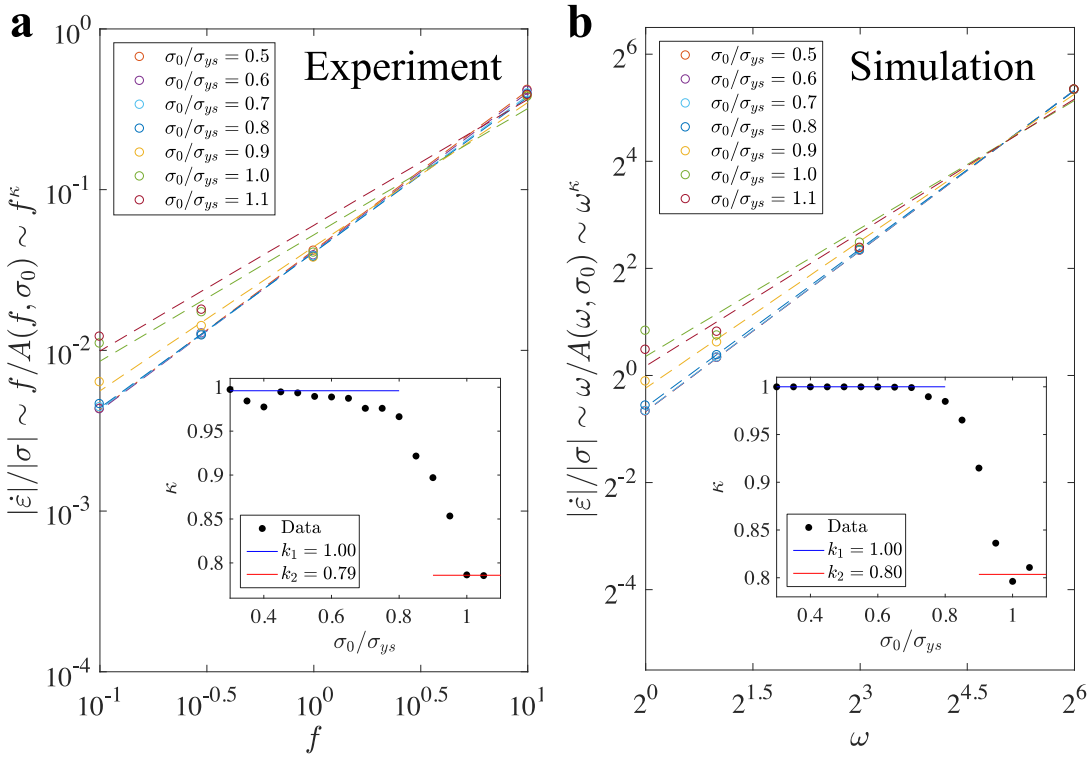

Figure 2.8 Scaling analysis of the normalized strain-rate amplitude. (a) The normalized strain rate amplitude scaling over driving frequency analysis[60] using experimental DMA data and (b) simulation DMA data. The figures show explicitly the fitting for scaling parameter κ using Equation 2.11 at different quasistatic stress levels. The inset presents the measured κ as a function of normalized stress. Figure reprinted with permission from [X. Ni, et al. *Phys. Rev. Lett.* 118, 155501 (2017)] Copyright (2017) by the American Physical Society.

Figure 2.8 shows the scaling analysis of the normalized strain rate amplitude vs driving frequency for the dynamic modulus amplitude calculated from the experiments and simulations at different quasistatic loads. The insets show the scaling parameter κ as a function of the normalized stress. These plots convey that at both small and large stress regimes, experiments and simulations produce scaling behaviors that are in agreement with the mean-field depinning predictions, and a smooth, microplastic crossover connects these two extreme regimes. The experiments and simulations reveal enhanced micro-plasticity activities as the system is stressed close to yielding. The actual mechanism that is responsible for the increased "susceptibility" to plasticity can be a thermally activation process like cross slip, or the collective dislocation bowing out due to long-range interactions, *i.e.*, the Andrade mechanism[57].

2.4.2 Driving Modulated Microplastic Events

Using the DMA simulation results, the statistics of microplasticity events the oscillatory stress excitations before the avalanche-dominated post-yield regime can be investigated during and placed in the context of the commonly observed distributions of large plastic events in small-scale. An avalanche is considered to finish simultaneously in a single time step, so avalanche event size S is equivalent to the strain increment. The stress-binned complementary cumulative distribution function (CCDF) of S can be integrated,

$$\mathrm{CCDF}(S) \sim \int_{S}^{\infty} P\,(S')dS', \tag{2.12}$$

where $P(S)$ is the probability distribution function of slip size S. For each quasi-static stress state, CCDF(S) is evaluated from eight random configurations driven at frequency

2 rad/s. Only one frequency result is presented here because no frequency dependency is observed with regard to the event size distribution.

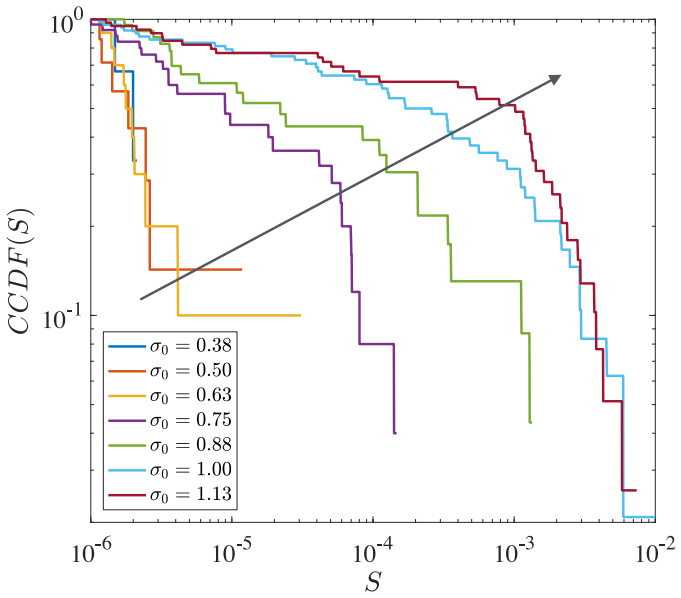

Figure 2.9 Complementary cumulative distribution function CCDF of simulated avalanche event sizes S. The distribution analysis proves the presence of larger abrupt microplasticity event as more stress is applied – the arrow points toward the stress-increasing direction. The dissipation behavior converges to a saturated state when the system is approaching the nominal yielding.

Figure 2.9 shows the event distribution CCDF(S) as a function of applied quasi-static stress σ_0, where σ_0 is normalized by the global yield stress. As σ_0 is increased, more large-size slip events are present during the oscillations. The distribution saturates when the stress is approaching the nominal yield point. The overall behavior is qualitatively consistent with a proximate depinning critical point as well as the experimental trend observed in Ref. [47]. However, the system sizes studied do not permit the identification of the universality class and whether it follows mean-field scaling CCDF$(S) \sim S^{-0.5}$ [47,61]or not[59]. Given the purpose of the modeling, the simulation focuses on the regime that could reveal pre-yield dissipation activities caused by the small pre- or intra-avalanche events.

The model does not have a mean-field interaction kernel, and can fail for the post-yield large-event regime.

Using the same simulation system, the correlation of the microplasticity events to the oscillatory drive is investigated. Focusing on the stochastic burst events, simulations are set up for two random configurations with the same parameters and investigate the differential strain rate output.

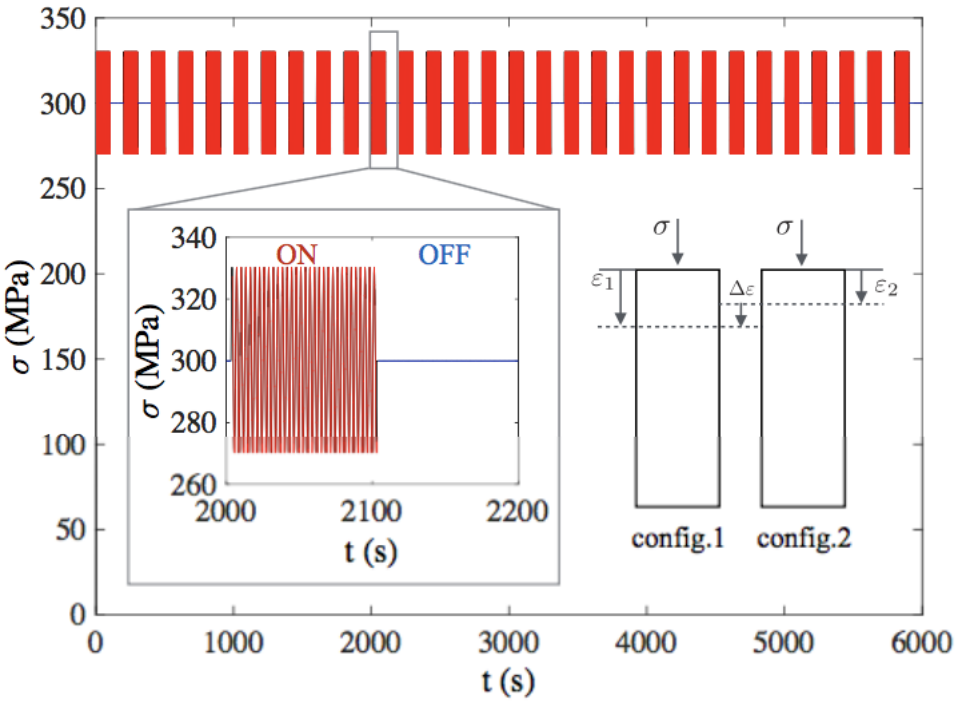

Figure 2.10 The differential-strain-modulation simulation scheme. The main figure is the prescribed stress vs. time, with a zoom-in in subsequent oscillation ON and OFF periods shown in the left inset.

As is shown in Figure 2.10, a constant quasi-static stress σ_0 = 300 MPa is applied to both configurations, on top of which a 30 MPa, 2 rad/s stress oscillation is turned on and off in sequent 100-s time intervals. The total test time goes up to 6000 s. The drive on the two

independent configurations is always simultaneous – if no stochastic strain events occur the differential strain rate $\Delta\dot{\varepsilon} = \dot{\varepsilon}_1 - \dot{\varepsilon}_2$, or equivalently the differential slip size $\Delta S = S_1 - S_2$, will remain zero. In other word, the size of ΔS characterizes the magnitude of stochastic microplasticity events.

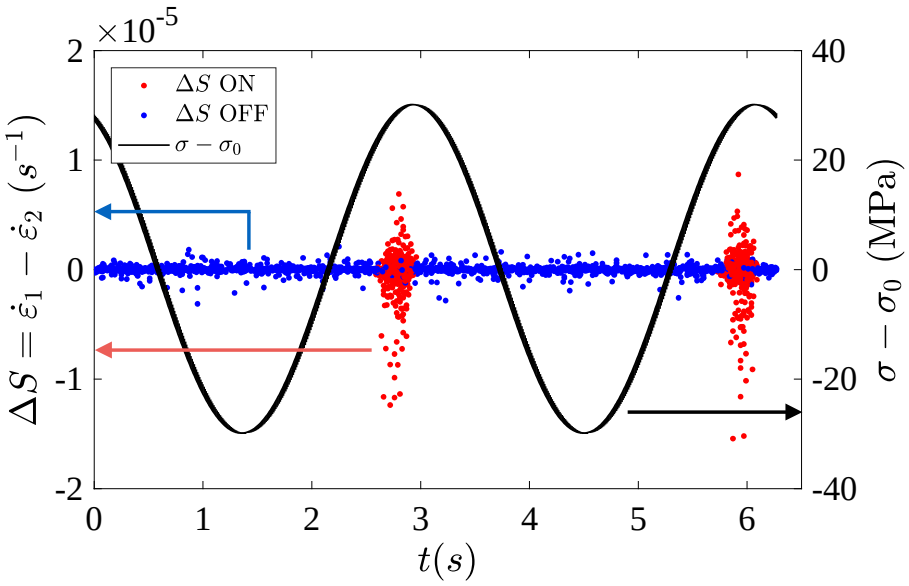

Figure 2.11 The differential strain rate data, or equivalently, the differential slip size ΔS vs. time data in oscillation ON and OFF intervals, marked as red and blue separately. The time-series data are folded into two periods of driving, with the black curves showing the folded oscillatory driving stress.

Figure 2.11 shows how the differential event size ΔS changes over stress oscillation. The red and blue data are ΔS in time series during the oscillation ON and OFF intervals, folded into two periods of driving. The comparison between the ON and OFF segments shows that larger differential strain events emerge when there is a finite stress perturbation, though the predominant quasi- static stress σ_0 is the same. The black curves are the prescribed stress oscillation $\sigma - \sigma_0$ vs. time. During the ON segments, ΔS increases when the external stress is approaching its global maximum, as the quasi-static stress direction

is assigned positive – there is clearly a correlation between the microplasticity event size and the external drive.

The event size distribution and the differential strain modulation analysis characterize the contents of the dissipative component resolved in the DMA experiments as stochastic strain events. These microplasticity activities can be excited by stress perturbations around nominally elastic loading and are correlated to the drives. Larger microplasticity events are expected to occur when the system is loaded at a quasi-static stress level closer to the global yield stress. It will be interesting to directly detect these events in future high strain resolution experiments. The simulation results will be directly applied as a theoretical basis for the macroscopic experiment on microplasticity in Section 4.5.4.

2.5 Summary

Oscillatory loads are imposed in the nominal elastic regime of the uniaxially compressed 500 nm-diameter single crystalline Cu nanopillars. Monotonically increasing stresses above the bulk yield point of ~10 MPa[86,87] are applied to investigate the mechanically correlated material response. Analysis of the cumulative oscillatory response reveals a substantial deviation from the nominally perfectly elastic behavior, as well as an emergent dissipation signature in what has always been considered preyield regime. This finding resembles prior research on amplitude-dependent internal friction in metallic materials[13,88]. The nanomechanical experimental observations are corroborated by a mesoscale dislocation plasticity model, which accounts for dislocation avalanches (fast processes) and the viscoplastic response (slow time scales) during oscillatory loading. A formulated scaling analysis shows a smooth transition of the system from perfect elasticity to

dislocation depinning-driven plasticity that occurs at loads lower than the global yield stress. This approach represents a new pathway to investigate and quantify the abrupt plastic events that emanate from dislocation activities even in the preyield regime that occur ubiquitously during deformation of small-scale single crystals below instrumental noise levels.

The developed methodology can be applied to characterize preyield dislocation dynamics in extensive list of fcc, bcc, and hcp materials. The micromechanical study sheds light on detecting crackling noise in macroscopic sample subjected to nominal elastic loading. The observation of such events might lead to better prediction of plastic yielding and even incipient fracture for structural materials. The preyield mechanical noise itself can be a hidden problem for instrumentation that requires high strain sensitivity. An effort in searching for the same type of microplastic noises in macroscopic samples will be discussed in Chapter 4.

Chapter 3: Yield-Precursor Dislocation Avalanches in Small-Scale Crystals

The transition from elastic to plastic deformation in crystalline metals shares both history dependence and scale-invariant avalanches behavior with other non-equilibrium systems under external loading. Many of these other systems, however, typically exhibit purely elastic behavior only after training through repeated cyclic loading; recent studies in these other systems show power laws and scaling of the hysteresis magnitude and training time as the peak load approaches a reversible-irreversible transition (RIT). This chapter discusses the discovery of yield-precursor dislocation avalanches in small crystals, which shows that the deformation of crystalline materials shares these key features. Yielding and hysteresis in uniaxial compression experiments of single-crystal Cu nano- and micropillars decay under repeated cyclic loading; the amplitude and decay time diverge as the peak stress approaches the failure stress, with power laws and scaling as seen in RITs in other nonequilibrium systems. These effects are observed to become smaller as the pillars become larger, perhaps explaining why scale-invariant training effects have not been observed in macroscopic samples.

3.1 Introduction

As introduced in Section 1.2.1, the mechanical deformation of macroscopic metals is usually characterized by the *yield stress*, below which the metal responds elastically, and beyond which plastic deformation is characterized by complex dislocation avalanches[25]. In small-scale crystals, these avalanches are manifested as discrete strain bursts in the

stress-strain response of the sample. The yield stress depends on the history of the sample, *i.e.* under uniaxial loading paths. Textbooks say that if the sample were to be unloaded and immediately re-loaded, the yield stress would be defined by the previous maximum stress – most metals *work harden* under increasing loading, with no deviations from linear-elastic response below each yield stress[27]. Many features of this description are shared by other nonequilibrium systems under deformation: dilute colloidal suspensions[89,90], plastically-deformed amorphous solids[47,91–95], granular materials[96–99], and simulated dislocation systems[100] exhibit a transition with clear analogies to work hardening and yield stress. In all of these other systems, the loading/unloading hysteresis disappears only after repeated cycling to the maximum stress, coined as material *training*. The complex avalanches that mediate deformation in these other systems exhibit power laws and scaling in the limit of maximum stress approaching a critical value, the so-called reversible-irreversible transition (RIT) that separates trainable and untrainable regimes. This work uncovers that sub-micron- and micron-sized metals display the same RIT, with the training hysteresis reduction in larger sample volumes.

3.2 Quasistatic Compression Experiment

3.2.1 Yield-precursor Avalanches

The ‘textbook description’ of yield stress and work hardening does not hold for metallic micro- and nano-pillars under uniaxial loading. In these experiments, the plastic strain bursts lead to a drop in the applied force caused by the finite machine stiffness under both displacement- and loading-rate control. The indenter tip used to compress these samples re-attains the prescribed load after a fast avalanche event is completed (see Figure 3.1). In

most experiments, this stress drop catch-up process is manifested by a spontaneous unloading-reloading response. The stress that initiates an avalanche can be regarded as the updated yield stress of the deformed pillar.

Figure 3.1 (a) shows a typical stress-strain response during displacement controlled (DC) compressions of single-crystalline <111>-oriented copper micropillars. This plot reveals the presence of occasional strain bursts during the post-avalanche reloading process at stresses that are lower than the current "yield stress", which is defined as the previous maximum stress that triggered the most-recent avalanche unloading event, as exemplified Figure 3.1 (b). The presence of yield precursor avalanches contrasts with the conventional definition of history-*dependen*t yield point that strictly separates the purely elastic behavior upon unloading and reloading from irreversible plasticity.

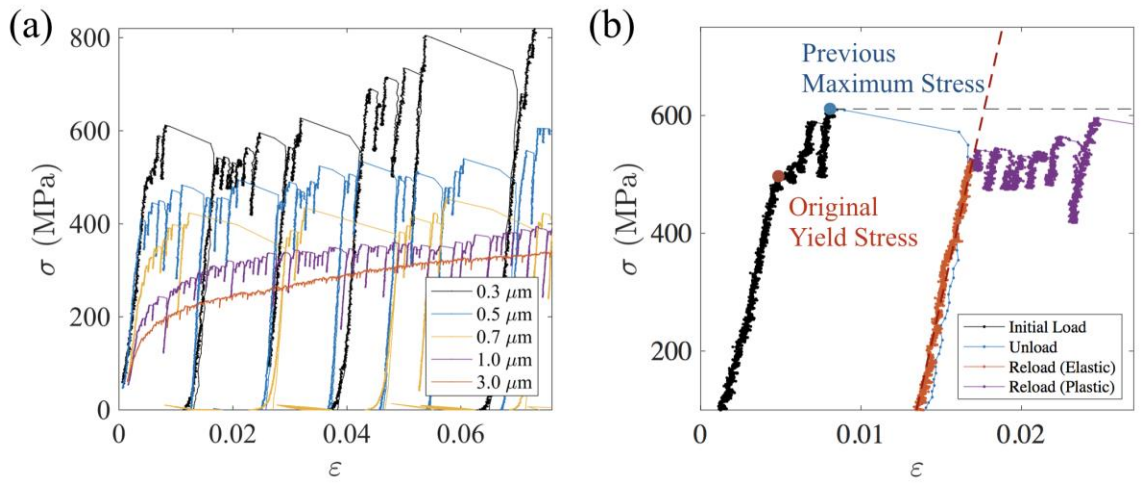

Figure 3.1 Precursor avalanches present in the quasistatic uniaxial compression experiments on different size of single crystalline copper pillars. (a) Sample stress-strains and (b) a close-up of a fast-avalanche induced unloading-reloading process. The sample starts to deviate from elastic response before reaching the updated "yield stress" defined as the previous maximum stress.

In the monotonic loading experiments above, larger pillars loaded under displacement control (DC) generally produce shorter avalanche strains[39,40] and are less frequently spontaneously unloaded by the instrument compared with the smaller pillars. Load-controlled (LC) compression experiments with several prescribed unload-reload cycles along the quasi-static compression are conducted to gain controls over the unloading amplitude and frequency to investigate the effect of system size on precursor avalanche behavior, where "system size" refers to the overall pillar volume.

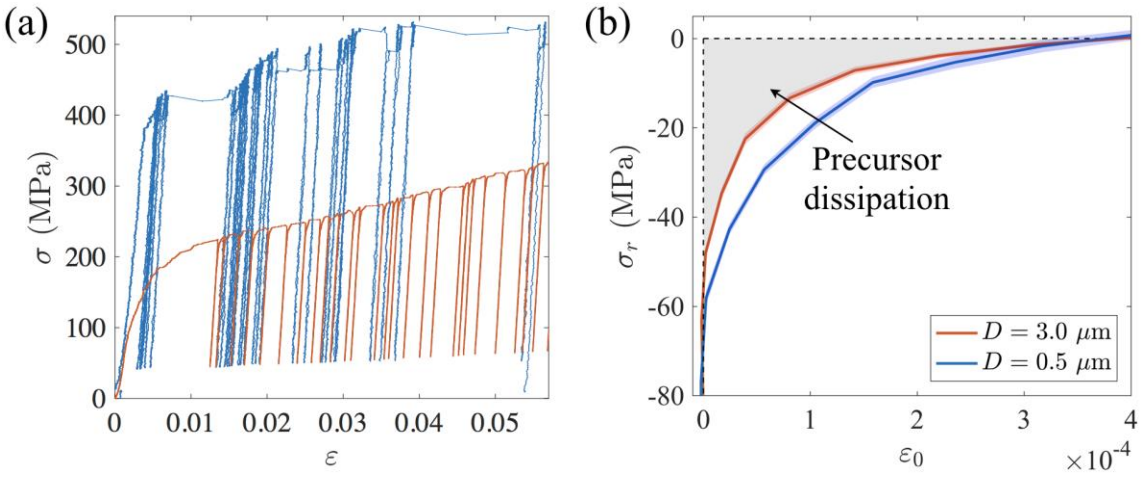

Figure 3.2 Precursor avalanches present in the uniaxial unload-reload cyclic compression experiments on different size of single crystalline Cu pillars. (a) Sample stress-strain and (d) the reconstructed non-Hookean stress-strain for two representative load-controlled (LC) unload-reload compression experiments (see Section 3.2.2 for detailed reconstruction procedures) on 3 μm and 500 nm diameter pillars.

Figure 3.2 (a) shows such unload-reload stress-strain response of representative 500 nm and 3 μm diameter Cu pillars. Figure 3.2 (b) compares their yield-precursor stress-strain response, σ_r *vs.* ε_0, where σ_r is the stress reconstructed as an average of all reloading stresses zeroed at their previous maximum stress, at a fixed reloading plastic strain ε_0. The next Section will describe the reloading stress-strain reconstruction protocol in details.

The types of precursor avalanches observed during the deformation of micropillars that extend over $\sim 10^{-4}$ strains at precursor stresses that are ~ 60 MPa lower than the previous maximum stress would pose significant corrections to Hookean elastic behavior if they persisted to macroscopic systems. An integral over the reloading reconstructed stress-strain,

$$U = -\int \sigma d\varepsilon, \tag{3.1}$$

evaluates the energy per volume dissipated by the precursor avalanches, the *precursor dissipation*, as indicated by the shaded area in Figure 3.2 (d) for 3 μm diameter samples. The precursor dissipation of ~ 60 kPa in the smaller 500 nm diameter pillars is larger than that of ~ 4 kPa in the larger 3 μm diameter samples, which suggests that the precursor avalanches may disappear in macroscopic samples, perhaps explaining why it has not been thoroughly examined in existing literature.

3.2.2 Reloading Stress-strain Reconstruction

In the previous Section, a reloading stress-strain reconstruction protocol is applied to analyze the yield-precursor behavior for different size pillars. As the occurrence of avalanches upon reloading is stochastic in small-scale crystals, the main purpose of the stress-strain reconstruction is to average all the reloading curves as a measure of the ensemble precursor deviation from the textbook "peak stress" yielding.

Figure 3.3 (a) shows a sample stress-strain data of load-controlled (LC) uniaxial compression tests on 500 nm diameter pillars with prescribed unload-reload cycles. The cyclic loading rate is ~ 400 MPa/s, while the maximum stress is increased by ~ 5 MPa per

cycle, which is equivalent to a quasistatic ramping rate of ~ 1.4 MPa/s. A minimum stress of ~ 40 MPa is set to maintain tip-sample contact.

For the reconstruction process, the origins of each reloading process are shifted such that the stress is zeroed at the previous maximum stress (usually at the start of unloading) and the strain is zeroed at the beginning of each reloading, which is demonstrated in Figure 3.3 (b). During reloading, if a new avalanche happens before reaching the previous maximum stress (re-zeroing stress), it is a precursor avalanche.

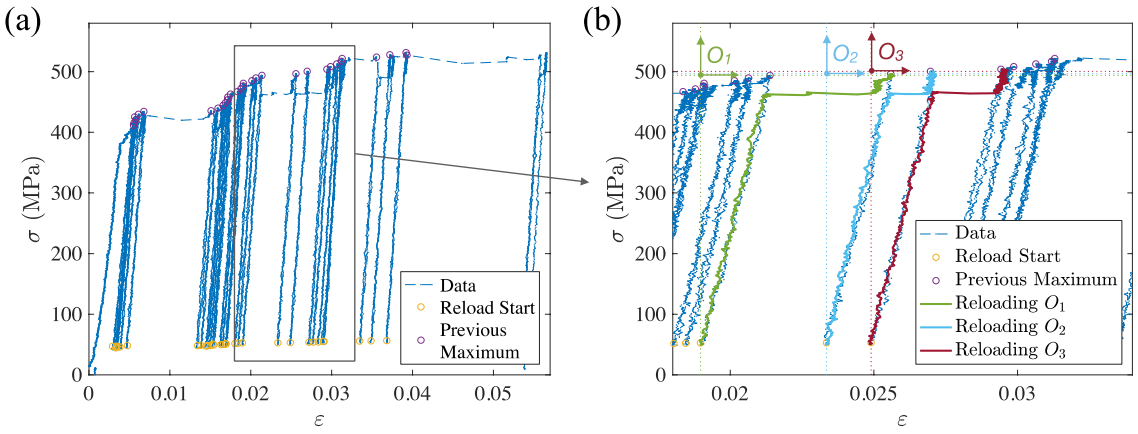

Figure 3.3 Re-zeroing reloading stress-strain in unload-reload experiments: (a) A sample stress-strain curve for the unload-reload test on a 500 nm diameter Cu pillar (b) A closer look at the sample unload-reload cycles demonstrating where the stress of each reloading is re-zeroed with the previous maximum stress (textbook yield stress updated upon deformation) and the strain is re-zeroed with the starting strain of the reloading process.

Each re-zeroed reloading process for any pillar is then treated as an individual reloading test on one nanopillar. The total precursor behavior for the pillars can be reconstructed according to a Gedanken experiment on a macroscopic sample composed of stacks of nanopillars either in parallel or in series, as illustrated in Figure 3.4.

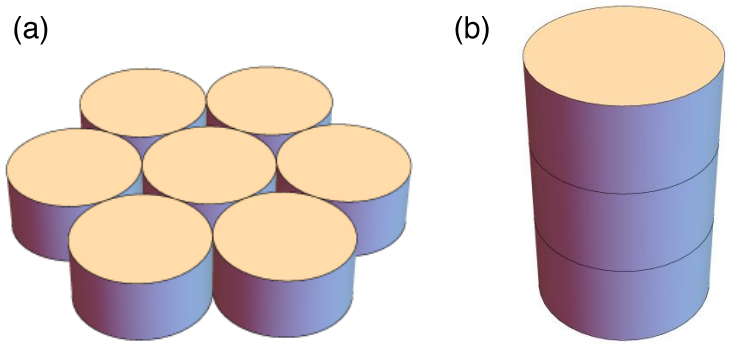

Figure 3.4 Schematics of the Gedanken compression experiments with (a) in-parallel (prescribed strain) and (b) in-series (prescribed stress) configurations.

The reloading response of each pillar can be interpolated and averaged along the monotonically increasing strain ε_0 (in-parallel) or stress σ_0 (in-series) for the ensemble response. Figure 3.5 (a) shows examples of the in-series and in-parallel interpolation of the single reloading curve shown in Figure 3.3 (b) and zeroed at O_1.

In the in-parallel configuration, for the i^{th} pillar, strain $\varepsilon_i = \varepsilon_0$ is controlled and stress σ_i encodes the material's response. The system composed of N pillars has a stress response,

$$\begin{aligned}\sigma_r &= \frac{1}{N}\sum_{i=1}^{N}\sigma_i \\ &= \frac{1}{N}\sum_{i=1}^{N}(E_i + \delta E_i)\varepsilon_0 \\ &= E\varepsilon_0 + \frac{1}{N}\sum_{i=1}^{N}\delta E_i\varepsilon_0 \\ &= (E + \delta E)\varepsilon_0. \end{aligned} \tag{3.2}$$

In Equation 3.1, $\delta E = \frac{1}{N}\sum_{i=1}^{N} \delta E_i$ characterizes the plastic response of the N-pillar system. σ_r and ε_0 are the reconstructed stress and strain. Similarly, the series reconstructed strain ε_r can be expressed with respect to the prescribed stress σ_0,

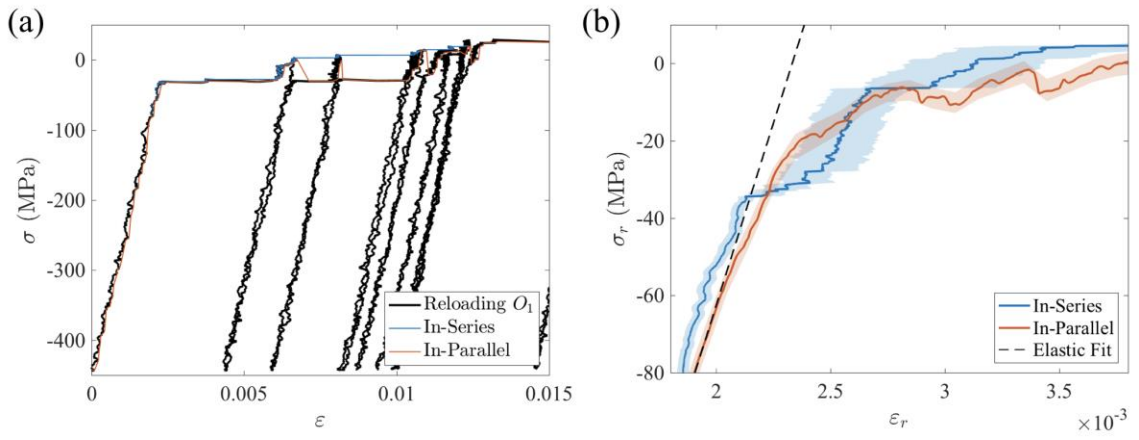

Figure 3.5 Stress-strain reconstruction according to the Gedanken compression experiments on micropillars (a) Examples of the in-series strain and in-parallel stress interpolation of the single reloading curve shown in Figure 3.3 (b) and zeroed at origin O_1. (c) The averaging stress-strain reconstruction of the reloading curves for both in-parallel and in-series cases for the sample load-controlled test shown in Figure 3.3.

Figure 3.5 (b) shows the sample in-series and in-parallel averaging reconstruction of reloading stress and strain for the same unload-reload test on a 500 nm diameter Cu pillar as shown in Figure 3.3. In the previous section, present the in-parallel reconstruction for tests on seven identically-prepared pillars for each size. The elastic strain fitted from the linear reloading regime, $\sigma_r \in [-300, -100]$ MPa is subtracted to keep only the Non-Hookean part of strain in the final results. The elastic fit for the sample in-parallel reconstruction stress-strain is shown in Figure 3.5 (b).

The same reconstruction analysis can be applied to the conventional load- or displacement-controlled nanomechanical experiments. In the quasi-static, uniaxial

loading experiments, the plastic strain bursts usually lead to drops in the applied force caused by the finite machine stiffness under either displacement or load control. Figure 3.6 (a) shows a sample stress-strain of a load-controlled compression test on a 500 nm diameter Cu pillar, marked with the onset and finish of each avalanche event: at the beginning of a displacement burst of size Δx, the force applied to the sample drops by $k\Delta x$, with k being the machine stiffness. Driven by the feedback control, the indenter tip will re-attain the prescribed load on the sample after a fast avalanche event is completed. This stress-drop-and-catch-up process is manifested as a spontaneous unload-reload response. The stress that initiates an avalanche can be regarded as the updated yield stress of the deformed pillar. The yielding avalanche triggers the following unloading process. When the avalanche finishes, the load control re-engages and starts the reloading process.

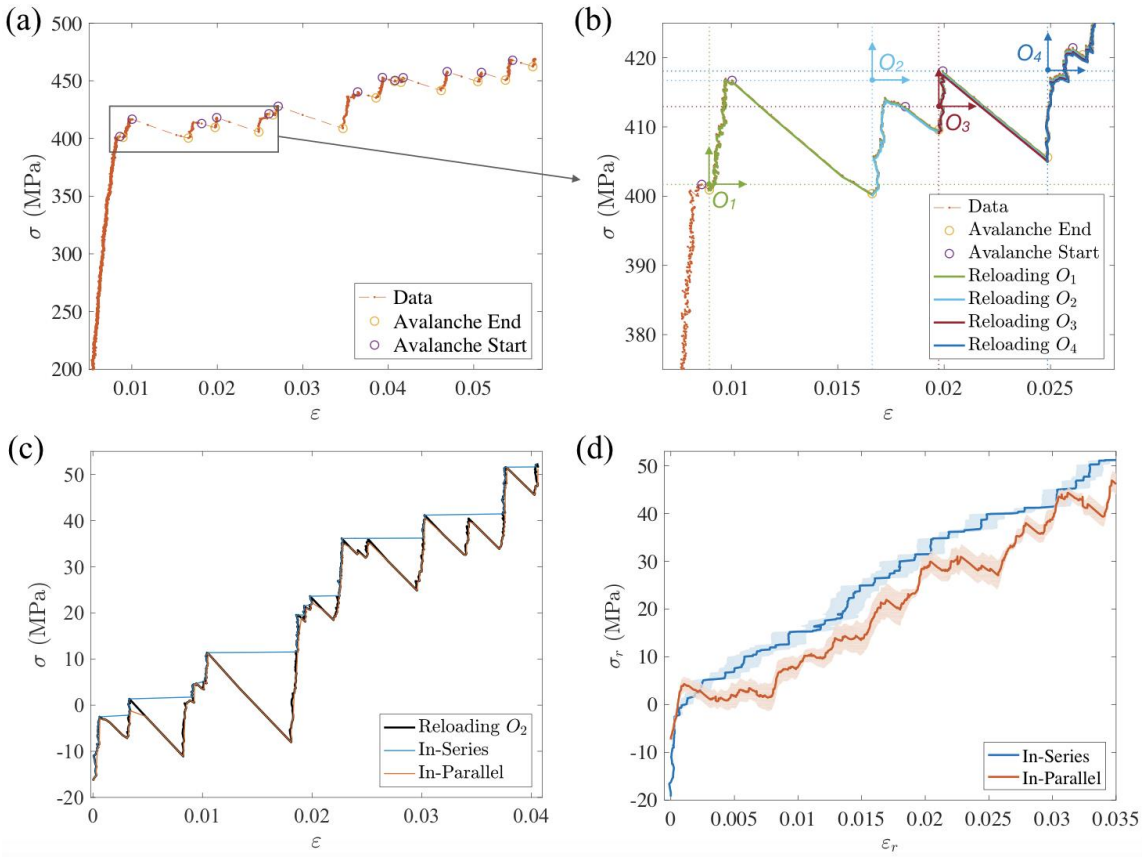

Figure 3.6 Stress-strain reconstruction for finding precursor avalanches in the quasistatic load-controlled experiment: (a) A sample stress-strain curve for the unload-reload test on a 500 nm diameter Cu pillar (b) A closer look at the sample unload-reload cycles demonstrating the re-zeroing process. (c) Examples of in-series strain and in-parallel stress interpolation of the single reloading curve shown in (b), zeroed at origin O_1. (d) The averaging in-parallel and in-series stress-strain reconstruction of all reloading curves shown in (a).

Figure 3.6 (b-d) exemplify the reconstruction process for the load-controlled experiment shown in Fig S3(a) following the same protocol as the one applied to the unload-reload experiments: (b) first shift origins of the stress-strain data after each yielding avalanche with the stress zeroed at the start of the avalanche and strain zeroed at the end of the avalanche, (c) interpolate the in-series strain or in-parallel stress, and (d) take averages of the interpolated strain/stress for the stress-strain reconstruction.

3.2.3 Precursor Avalanches in Different Loading Modes

The stress-strain reconstruction analysis can be applied to displacement-controlled and load-controlled quasistatic compression tests, as well as unload-reload cyclic compression tests, on different size Cu pillars with diameters of 300 nm, 500 nm, 700 nm, 1 μm, and 3 μm. The sample stress-strain measurements are shown in Figure 3.7 (a-c), while the in-parallel reconstructed reloading curves are correspondingly shown in Figure 3.7 (d-e). Each reconstruction analysis takes averages of all reloading curves from individual tests on seven identically-prepared pillars. The elastic strain is subtracted from the reconstructed strain; the results keep only the plastic precursor strain. The reconstructed non-Hookean reloading stress-strain quantitatively evaluates the averaging yield-precursor avalanche behavior of a specific size of Cu pillar under a specific loading mode.

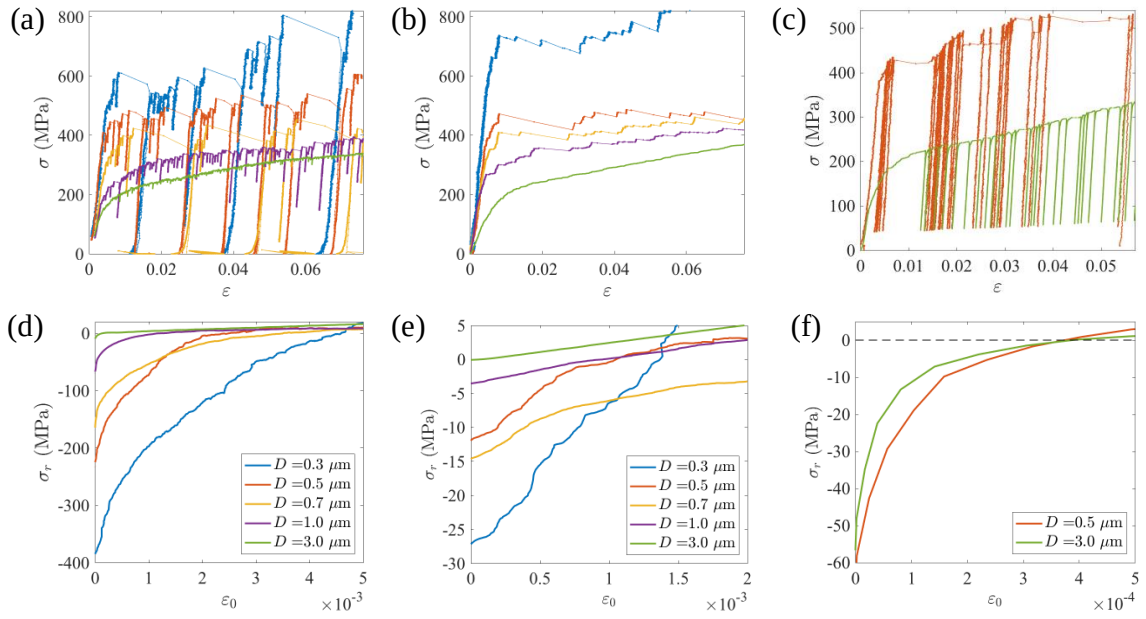

Figure 3.7 Precursor avalanches present in different loading-mode uniaxial compression experiments on different size Cu pillars. Sample stress-strain (top) and in-parallel reconstructed non-Hookean stress-strain (bottom) for (a, d) displacement-controlled (DC) monotonic-loading, (b, e) load-controlled (LC) monotonic-loading, and (c, f) unload-reload cyclic-loading compression experiments on different size pillars. In general, less precursor dissipation is observed in larger Cu pillars.

In all cases, precursor dissipation is prevalently observed in small pillars. A comparison amongst the different loading mode results provides insights into the precursor avalanche behavior: 1. Larger precursor strains are observed in displacement-controlled tests than load-controlled tests. As shown in Figure 3.7 (a) and (b), the avalanche-induced unloading amplitudes in displacement-controlled tests are on average larger than those in the load-controlled experiments. This might infer that the size of precursor strains is dependent on unloading stress amplitude. 2. The precursor strains in unload-reload tests are much smaller than those of the displacement-controlled tests, though the unloading amplitude is of the similar scale (for the 500 nm diameter pillars). One possible explanation is that part of the “precursor strains” observed in the quasistatic compression tests are “unfinished”

avalanches caused by non-perfect control: unlike the prescribed unloading in unload-reload tests, unloading processes in the monotonic loading test are spontaneously triggered by fast avalanches; thus, stress always drops during a slip event, which might interrupt the growing avalanche, leaving residual avalanche to be re-activated upon the subsequent reloading process. 3. Larger precursor dissipations are observed in smaller pillars. This emergent size dependency can be an intrinsic size effect of materials' yield precursor behavior; on the other hand, it can also be a result of smaller pillars undergoing larger unloading amplitude as shown in in Figure 3.7 (a) and (b) – smaller pillars exhibit larger strain bursts, which in turn, will give larger stress drops due to the inherent machine stiffness in both displacement- and load-controlled tests.

The analysis results on simulated data (using 3D discrete dislocation dynamics) show similar qualitative behavior (G. Costantini and S. Zapperi, unpublished). Further investigation on the emergent size effect, e.g. doing same-amplitude unload-reload tests on different sizes of pillars, is beyond the scope of this work.

3.3 Cyclic Training Experiment

Cyclic loading experiments are then conducted to study how the precursor hysteresis changes under repeated loading to the same maximum stress, analogous to experiments on other non-equilibrium systems[89,90]. 3 μm diameter single crystalline Cu pillars are chosen as to be the primary experimental system because it is sufficiently large amongst the "small-scale" counterparts to exhibit failure under quasistatic loading as well as relatively deterministic precursor avalanche behavior. Figure 3.8 shows the stress-strain

data from three representative experiments on the left along with the scanning electron microscope (SEM) images of a typical pillar pre- and post-compression on the right.

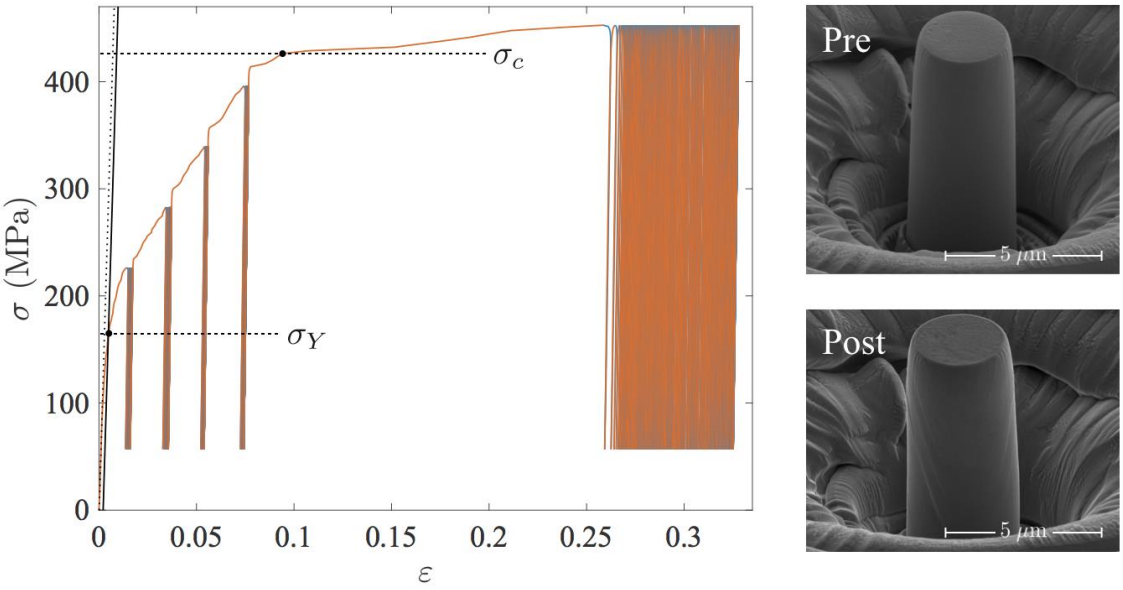

Figure 3.8 Cyclic training loading on micro-pillars. Left: stress-strain response from a training experiment on a 3 μm diameter copper pillar. Unloading and reloading stress-strain curves are marked in blue and red respectively. The maximum stress is increased in six steps. At each step, 100 unload-reload cycles are prescribed. Right: pre- and post-test scanning electron microscope (SEM) images a sample pillar.

Yield stress σ_Y is defined as the intersection between the stress-strain data and the 0.2% strain offset elastic loading segment according to the standard engineering criteria, which gives σ_Y ~ 160 MPa for the 3 μm diameter Cu pillars. The failure stress, σ_c, defined as the stress beyond which the samples are no longer able to support additional applied load, is ~ 420 MPa. Above this stress, the sample continually deforms plastically at a constant stress. Five-step maximum cyclic stress is prescribed from 228 MPa (0.54 σ_c) to 452 MPa (1.08 σ_c) at equal stress intervals of 56 MPa (0.13 σ_c). In each stress step, 100 unload-reload cycles are applied, during which the sample is loaded to the same maximum stress

and unloaded to a minimum of 56 MPa to maintain contact between the compression tip and the sample. The yield precursor dissipation evolution over cycles at each stress step, from an integral over each unload-reload cycle, $U = \int \sigma d\varepsilon$.

3.3.1 Drift Correction

Before looking closely into the precursor behavior over a large number of stress cycles, the thermal or instrumental drift during such tests with long testing time has to be taken care of. During tests with long unloading/reloading segment time, the instrumental drift in the machine can result in large discrepancies between the measured displacement and the actual sample displacement. This can give rise to errors in the calculation of the precursor hysteresis, which is very sensitive to the measurement of displacement during each unload-reload cycle.

Figure 3.9 (a) and (b) demonstrate the drift problem in the training experiment on 3 μm diameter Cu pillars by comparing the precursor hysteresis calculated over cycles of the same maximum stress ~ 350 MPa between the tests with 2 s (short), 80 MPa amplitude unloading/reloading segments and the tests with 4 s (long), 160 MPa amplitude unloading/reloading segments. Both tests use the same loading rate of 40 MPa/s. For the 4 s segment tests shown in Figure 3.9 (b), the precursor dissipation decays to negative values, which is unphysical for a uniaxial compression test on single crystalline metals. The negative hysteresis that is slowly-varying over time can be explained by the usually negative thermal drift present in the nanoindentation tests. An offline drift correction is applied to each unload-reload cycle. Figure 3.9 (c) shows the post-drift-correction precursor hysteresis vs. cycle data for the same set of 4 s segment tests, which mitigates

the unphysical negative values and exhibits similar decay-over-cycle behavior as that for the short segment test.

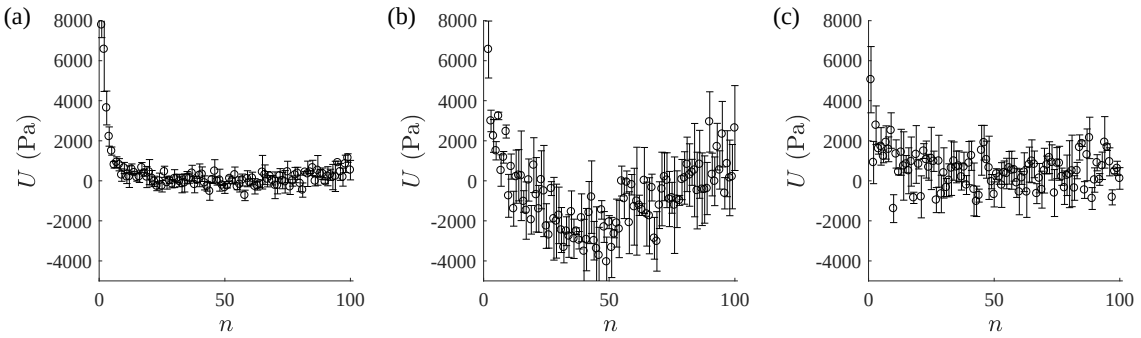

Figure 3.9 Effect of instrumental drift on the calculated precursor dissipation for 3 μm diameter Cu pillars. (a) Tests with 2 s (short) individual unloading/reloading segments show a clean decay of the average precursor dissipation. (b) Average precursor dissipation for tests with 4 s (long) unloading/reloading segments exhibit unphysical negative values (c) A drift correction on the 4 s segment test data mitigates the negative values and discloses a decay behavior.

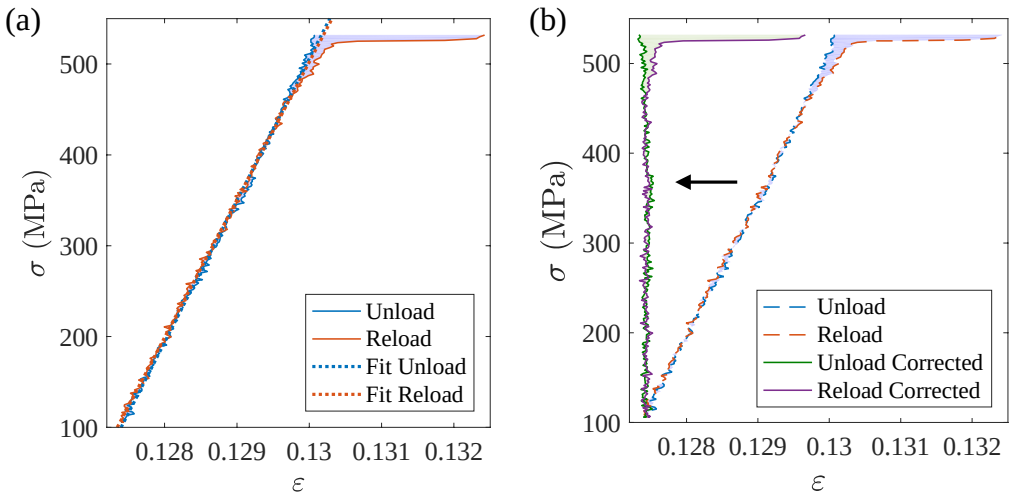

Figure 3.10 Demonstration of the drift correction process: (a) An example raw stress vs. strain data of subsequent unloading and reloading segments. The segments are individually linearly fitted to account for the slow instrumental drift in addition to the Hookean elastic strain; The fitting excludes data in the top 80 MPa segment within which precursor avalanches are present. (b) The linearly fitted strains are subtracted from the unloading and loading segments respectively to correct for the instrumental drift. The shaded area in the figures indicates the precursor hysteresis calculated from its corresponding set of data.

The drift correction is applied to each unload-reload cycle as the following. One raw stress-strain cycle, shown in Figure 3.10 (a), is taken as an example. The precursor hysteresis associated to the cycle is marked by the shaded area. Since the individual unloading/reloading segment duration (< 1s) is short, the drift rate during each segment is assumed to be constant. A linear fit is prescribed to each unloading/reloading segment below the onset stress of precursor avalanches (the top 80 MPa segment), to account for the Hookean strain as well as the linear drift. In Figure 3.10 (b), the linearly fitted strain is subtracted from the overall unloading/reloading strain for the drift-corrected hysteresis behavior. The post-correction deformation is plastic only.

3.3.2 Decay of Precursor Dissipation over Cyclic Loading

Figure 3.11 shows the sample 2nd, 5th and 8th cycles of drift-corrected data cycled to 340 MPa in Figure 3.8, with precursor dissipation indicated by the shaded areas. The sample data shows a decay in precursor dissipation in later cycles.

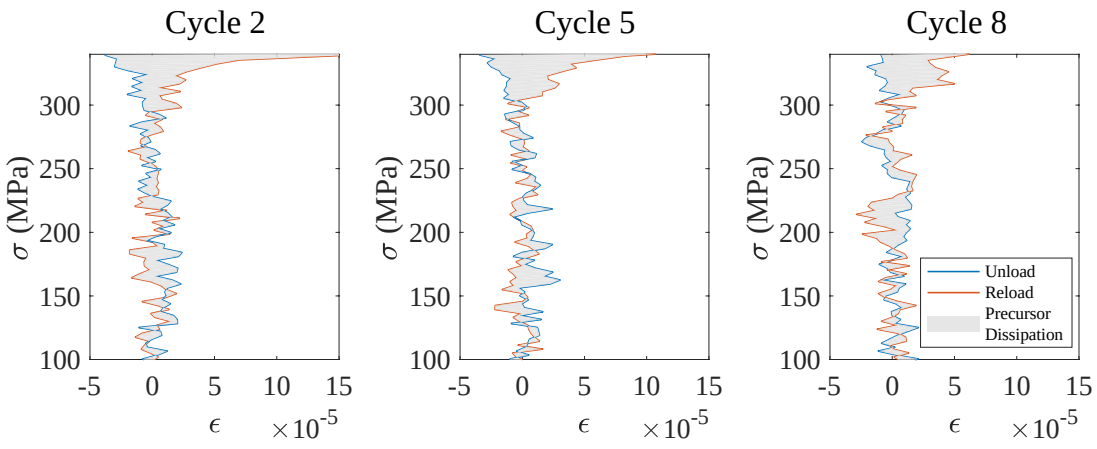

Figure 3.11 The reconstructed stress vs. strain during the 2nd, 5th, and 8th cycles with maximum stress held at ~ 340 MPa. The shaded area represents the energy dissipated through precursor avalanches, which decreases over cyclic loading.

The same multistep cyclic load function is applied to nine identically prepared samples. It is reasonable to assume that for a cycle at a specific stress step, the intrinsic precursor dissipation behavior is equivalent across all samples within statistical variation.

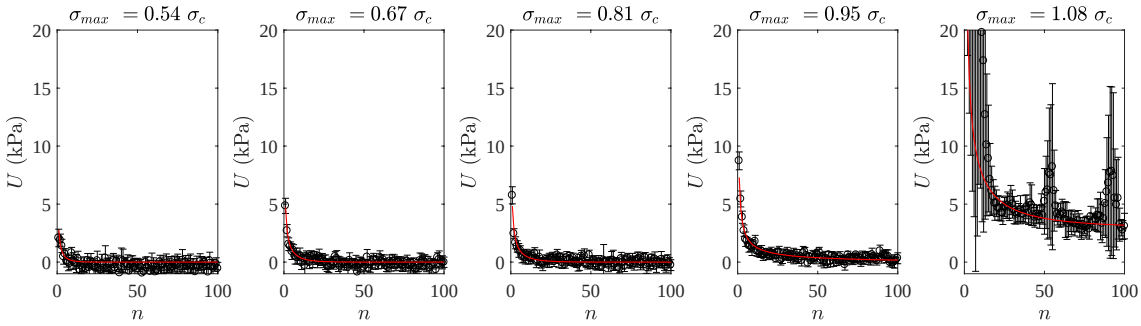

Figure 3.12 The precursor dissipation energy U decays with the number n of prior loading cycles at different maximum stress.

Figure 3.12 shows the average and standard error of the precursor dissipation as a function of cycle number for increasing stress steps. These plots unambiguously demonstrate the *training* phenomenon: the precursor hysteresis decays with cycling. Increasing the maximum stress triggers new precursor avalanches and new training cycles. Below the catastrophic failure stress σ_c, the precursor dissipation virtually vanishes. Above the failure stress, the hysteretic dissipation continues beyond the prescribed 100 stress cycles, which indicates that the training is incomplete.

The decay of precursor dissipation, U, versus number of cycles, n, is characterized using a fitting function $U_f(n)$[90],

$$U_f(n) = (U_0 - U_\infty)e^{-\frac{n}{\tau}}n^{-\delta} + U_\infty, \tag{3.3}$$

where $U_\infty = U_f(n \to \infty)$ is the estimated steady-state dissipation, and U_0 is the initial dissipation. The power law decay of U_f hints at the fluctuation behavior near the critical point. δ is evaluated from a simple power law fitting to the approximate critical behavior at $\sigma_{\max} \sim \sigma_c$,

$$U_f'(n) = U_f(n;\ \tau \to \infty, U_\infty \to 0) = U_0 n^{-\delta}. \tag{3.4}$$

A long-term 500 cycle training data at stress step $\sigma_{\max} = 1.08\ \sigma_c$ is used for the power-law fitting for δ, as shown in Figure 3.13. Over large number of cycles with the engineering maximum stress prescribed to be constant, the large plastic deformation in high-symmetry direction can cause a decrease in the true maximum stress applied to the sample due to volume conservation. As the cycling at the stress level above the critical stress goes, the maximum stress eventually falls below the critical stress over large precursor strain – the precursor dissipation does not decay to finite steady-state value over long cycling tests.

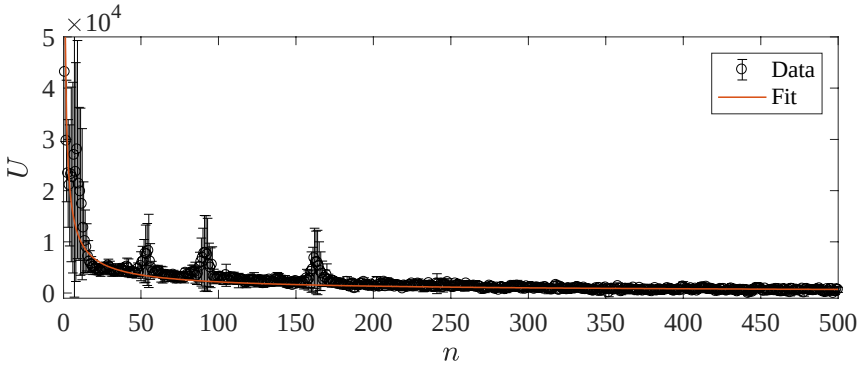

Figure 3.13 Power-law fitting to the long cycling training behavior. The precursor dissipation vs. cycle behavior at the stress $\sigma_{\max} \sim \sigma_c$ is approximately critical and can be characterized by a simple power-law decay for the fitting of the power-law exponent δ in the general model. The mean

value spikes at n ~ 55, 92, 162 are occasional large precursor avalanches present in individual tests.

The fitted mean power-law exponent $\delta \sim 0.68$ is applied in the general fitting model (Equation 3.3) for all stress steps. U_0 is the initial value of U_f. The fitting parameters, τ and U_0, as well as their confidence intervals were obtained using a nonlinear regression model featuring the Levenberg-Marquardt nonlinear least squares algorithm[101,102]. Each data point is weighted by the measurement error. The estimation error for the k-th parameter is taken as the 95% confidence interval, $2\sigma_k$.

3.4 Results

3.4.1 Reversible-to-Irreversible Transition (RIT) in Crystal Deformation

When plotting the characteristic time scale, τ, as a function of proximity to critical point on a log-log scale in Figure 3.14, a striking resemblance to the colloidal suspension systems shows up, which indicates that stress-driven dislocations in small-scale metals exhibit RIT behavior similar to that seen in sheared colloidal particles[90].

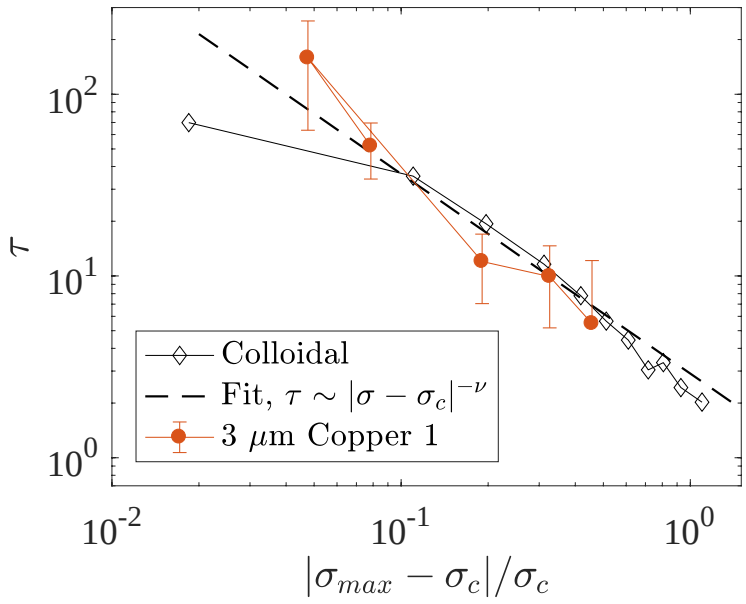

Figure 3.14 Training experimental results showing precursor dissipation activity at different maximum stresses. A direct comparison of dislocation RIT behavior gleaned from the Cu micropillar compression experiments with that reported for a colloidal particle system in sheared suspension[90], which provides evidence for a divergence of necessary cycle time τ to reach a reversible state, close to the critical failure stress.

This RIT behavior is *not* seen in 2D simulations of discrete dislocation dynamics at zero temperature, which do not capture dislocation creation or annihilation; the mechanisms and physical conditions underlying this behavior in simulations and experiments remain important questions for future studies.

Since the power-law exponent δ in the general fitting model is obtained from a critical point behavior approximation – a pure power-law fitting of the cyclic precursor dissipation data at the maximum-stress step close to the critical stress, it is necessary to investigate the error tolerance for the fitted δ: the power-law divergent behavior of the fitted time scale τ should not be sensitive to the changes of the prescribed power law

component δ in a range. This range can be evaluated by investigating fitted τ vs. σ_{max} for different values of δ.

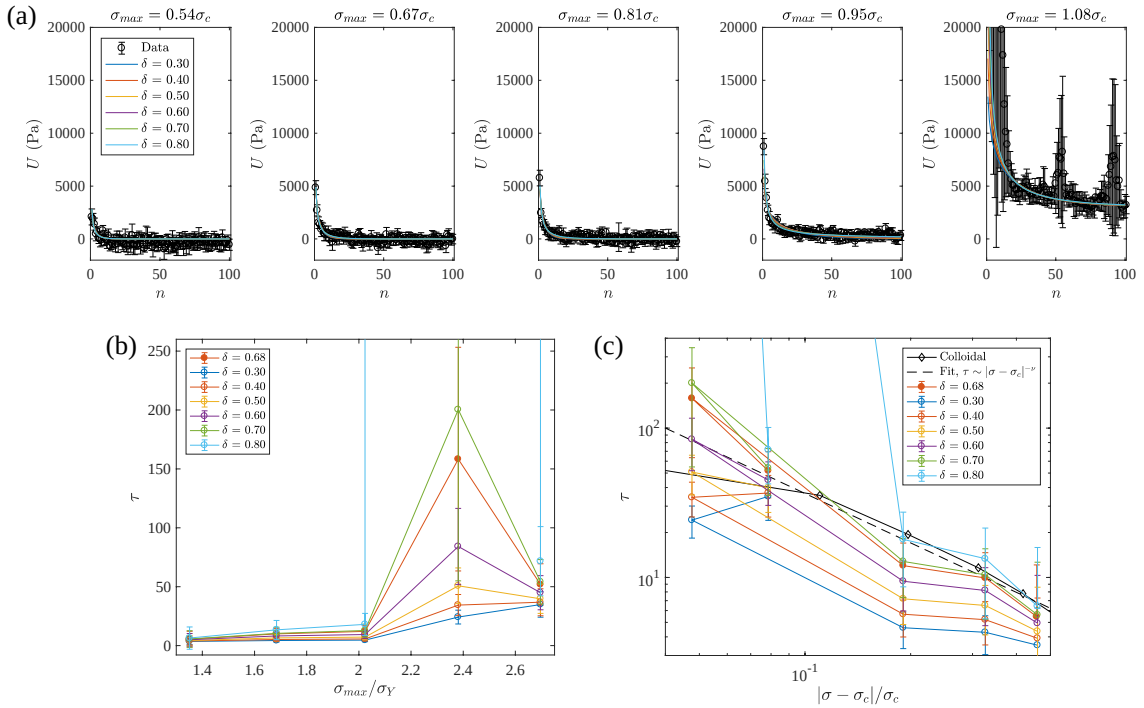

Figure 3.15 Fitting for decay time constant τ for 3 μm diameter pillars with different values of power-law exponent δ. Different δ-value fits are represented by different colors: (a) Fittings to U vs. n at increasing maximum stress, (b) fitted τ vs. σ_{max}, and (c) a scaling analysis of τ vs. σ_{max}.

The fittings to the 3 μm diameter pillar cyclic precursor dissipation data using different values of δ, sweeping the range 0.3 ~ 0.8 in a 0.1 interval, are shown in Figure 3.15 (a). Figure 3.15 (b) shows the fitted τ vs. σ_{max} with the same δ sweep. The scaling analysis of τ shown in Figure 3.15 (c) demonstrates that the divergent behavior of the training time constant does not change much when δ is in the range 0.3 ~ 0.7.

3.4.2 Size Effect

The precursor avalanches training behavior is investigated with smaller sizes of pillars with diameters of 0.5 μm and 1 μm. For 0.5 μm pillars, a total of twenty-six pillars were tested using six different maximum stresses ranging from 550 MPa to 800 MPa, with increments of 50 MPa. For 1 μm pillars, seven pillars were tested using five different maximum stresses ranging from 300 MPa to 600 MPa with increments of 75 MPa. For both training tests, a minimum stress of 100 MPa is maintained to keep the actuation punch in contact with the sample.

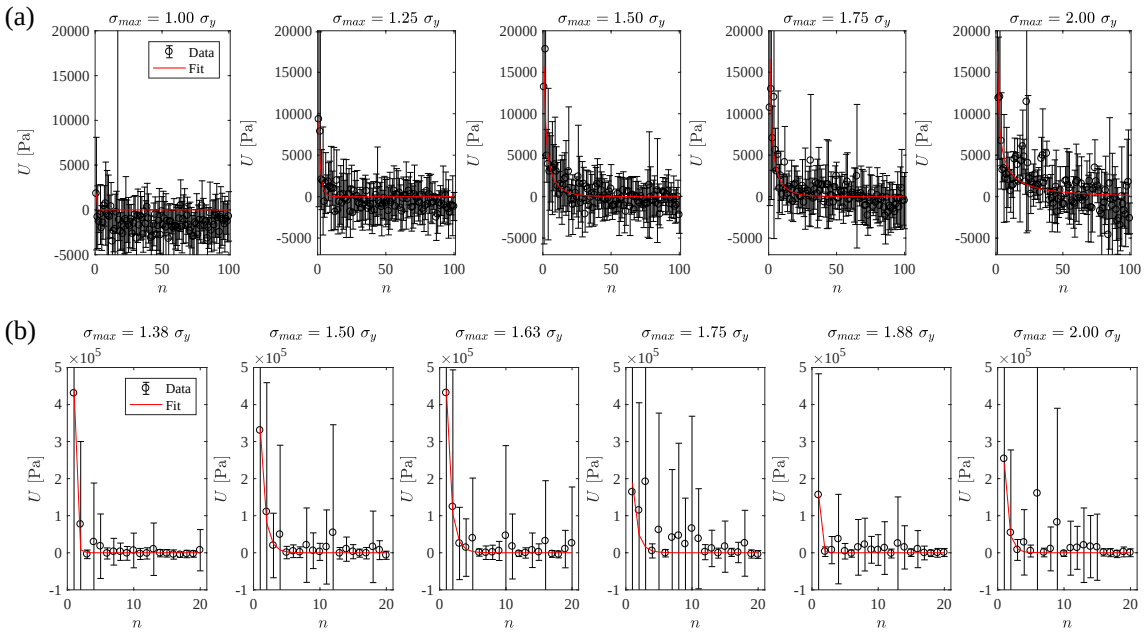

Figure 3.16 Precursor dissipation vs. number of cycle data for (a) 1μm diameter pillars and (b) 0.5μm diameter pillars. For all sizes and in all steps with $\sigma_{max} < \sigma_c$, the precursor dissipation can be trained away after a certain number of cycles. The magnitude of precursor dissipation is in general larger in smaller size pillars.

The analysis procedures described in previous sections for the 3 μm diameter pillars apply the same to examine the cyclic precursor dissipation behavior for the smaller 500 nm and

1 μm diameter pillars. The precursor dissipation vs. number of cycle analysis results are shown in Figure 3.16. It is worth noting that the training tests for 500 nm diameter pillars have too small unloading/reloading amplitude for drift correction. For both sizes of pillars, the precursor dissipation can be trained away after a certain number of cycles.

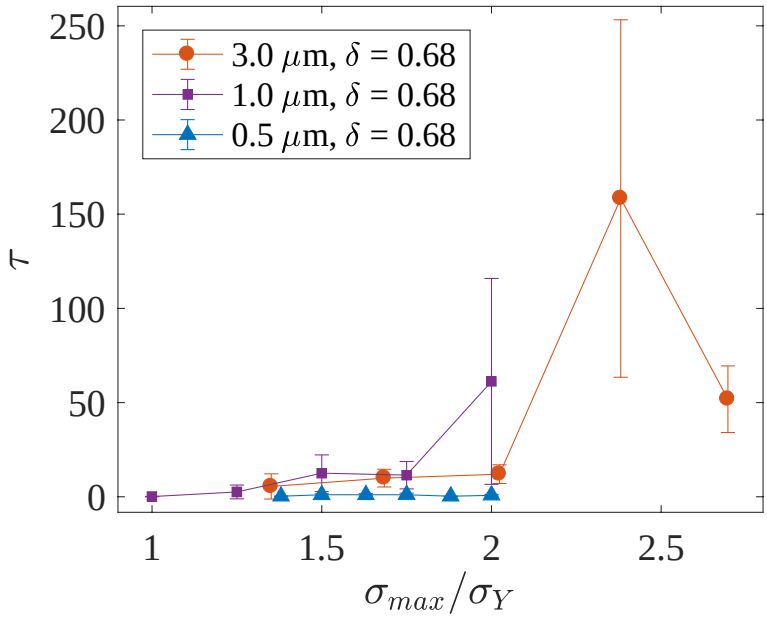

Figure 3.17 The characteristic decay time τ versus maximum stress σ_{max} (normalized by yield stress σ_Y) estimated for different pillar sizes.

Figure 3.17 compares the fitted decay time τ versus maximum stress σ_{max} (normalized by yield stress σ_Y) results for different pillar sizes. For 1 μm diameter pillars, the decay time slightly increases with stress. For 500 nm diameter pillars, it is hard to distinguish the training behaviors at different maximum stress from the available data.

3.5 Discussion

Analogous to the colloidal suspension systems, it is plausible that at low stresses, the strongly interacting dislocations in the pillars may rearrange themselves into a stable

configuration as the system reloads the first time. At higher peak stresses, the dislocation rearrangements in one cycle may trigger a cascade of further avalanches in subsequent cycles. In small-scale crystalline plasticity, the RIT corresponds to the stress at which additional cycling continues to plastically deform the system with no additional applied forces, which corresponds to the failure stress.

The critical behavior of the precursor avalanches observed here is potentially related the power-law distribution of dislocation avalanches observed in nano- and micropillars under monotonic loading. The precursor avalanches at an RIT usually diverge in size only near the failure stress. Plasticity avalanches under monotonic loading are usually considered to be a 'self-organized criticality'[31], which exhibits a power law scaling along the entire loading curve. Friedman et al.[47] measured a cutoff in the avalanche size distribution that diverged only as the stress approaches the 'failure' stress'[61] – precisely as one would expect for the approach to an RIT.

3.6 Summary

This work sheds light on the overlooked signature of yield precursor avalanches in conventional nanomechanical experiments. The amount of dissipation due to yield precursor avalanches is shown to decay over repeated stress training cycles. This training behavior is reminiscent of prior research on ratcheting in fatigue deformation studies [15,16], as well as the unloading effect on yield point phenomena[103,104]. The characteristic decay time is found to increase with the applied maximum stress. The apparent divergence of the time constant at a maximum stress near the quasistatic failure stress (see Figure 3.14) indicates that the flow transition of the dislocation system is fundamentally a RIT

transition. These observations may lead to a better understanding of plasticity and catastrophic failure in crystalline materials governed by complex dislocation dynamics. This fundamental connection between dislocation systems and other non-equilibrium systems can provide new insights into the microstructural design of novel materials.

Chapter 4: Crackling Noise Experiment

The pre-yield dislocation activities in micro or nano-scale metals have been discussed in previous chapters. One open question is whether these microplastic events can be resolved in the bulk materials. Is it only a matter of resolution or if there is any fundamental difference between the deformation physics of small-scale and bulk materials. In order to study the potential pre-yield microplastic events in macroscopic materials, an instrument is developed aiming at characterizing non-linear mechanical noise in metals subjected to elastic load. In macroscopic systems, microplastic deformation is expected to manifest as a non-stationary noise modulated by external disturbances applied to the material – a form of *mechanical upconversion* of noise. If they were to be detected – they should exhibit scale-free properties (maybe with cutoffs), manifested as *crackling noise*[51] introduced in Section 1.3.3. The main motivation for this work is to investigate the mechanical upconversion noise, *a.k.a.* crackling noise, in maraging steel components (cantilevers and wires) in the suspension systems of terrestrial gravitational wave detectors, as introduced in Section 1.4.1. Such instruments are planned to reach ambitious displacement sensitivities. Mechanical noise in the cantilevers could prove to be a limiting factor for the detectors' sensitivities, mainly due to non-linear upconversion of low frequency residual seismic motion to the frequencies of interest for the gravitational wave observations.

An experimental setup aiming at resolving the crackling noise in microplastic regime is custom-built with a target sensitivity ~ $10^{-15}\ m/\sqrt{Hz}$ in the frequency range of 10 –1000 Hz. A driving modulated noise is detected at the level of ~ $10^{-14}\ m/\sqrt{Hz}$ at frequency $f = 20$ Hz with a shape of $1/f^3$. The characteristics of the noise is compared with the

microscopic simulation results obtained in Section 2.4.2. An upper limit for the crackling noise level in advanced LIGO sensitivity is estimated based the prototype experiment measurements.

4.1 Introduction

This work investigates the possible influence of non-linear mechanical noise on the Advanced Laser Interferometer Gravitational-Wave Observatory (LIGO) detectors. The Advanced LIGO detectors are large-scale ground-based laser interferometers intended to observe gravitational waves[62]. To be successful, the LIGO detectors must reach an extreme displacement sensitivity in the audio frequency band. At the low frequency end of this band (10–20 Hz), the horizontal motion of the 40 kg fused silica mirrors, acting as test masses, must be only about $10^{-19} m/\sqrt{Hz}$. Since the detector is located on the ground, it employs complex seismic isolation systems to reduce the contamination of the sensitivity by local seismic activity. The Advanced LIGO test mass suspension system[65,105] (see Figure 1.3) consists of a quadruple pendulum for horizontal isolation and incorporates three stages of 50 cm- long cantilever spring pairs, made of maraging steel[106] for vertical isolation. The suspension wires are made of steel music wire, with the exception of the wires connecting test mass and the penultimate PUM mass, which are made of fused silica bonded to the mirror, to reduce thermal noise. Any mechanical noise occurring within the cantilevers or in the wires will propagate to the test mass at some level. In particular, the lowest set of cantilever springs, which are installed in the second mass from the top (the upper intermediate stage, or UIM), will couple most strongly to vertical displacement of the test mass, since there is less vertical isolation between them

and the test mass than for those cantilevers that are higher up the chain. In turn, vertical motion of the test mass will couple to its horizontal displacement, which is the degree of freedom which is measured to detect gravitational waves, due to mechanical imbalances in the suspension system and, ultimately, to the Earth's curvature[65]. Thus, even if the impulsive strain events at the test mass are small, their combined influence can introduce background noise which could limit the interferometer sensitivity.

Metals can also exhibit creep noise[107]. Although the underlying micro-mechanics of mechanical up-conversion of microplasticity and creep may be related, creep has an event rate that decreases quickly after the initial stress, and experimental investigations have shown that the creep can be reduced with the use of maraging steel[108–111]. This work however focuses on mechanical events that are continuously triggered by a time varying external perturbation, such as the Advanced LIGO suspension cantilevers which are subjected to by the local micro-seismic activity of the ground. In addition, since it is virtually impossible to distinguish between events happening in the cantilevers from those happening in the suspension wires or in the clamps, the system mimics as close as possible the Advanced LIGO configuration for cantilevers, wires, and clamps. It is known that mechanical noise occurs when metals are stressed in the plastic regime. In the Advanced LIGO suspension system, however, the cantilever and wires loads are solidly within the macroscopically elastic regime, specifically about 50% of the yield stress[106]. Interest is in the first direct detection in macroscopic-scale metals for discrete, stochastic deviation from linear mechanical behavior in crystalline materials this far below the engineering yield stress.

The effort is not in trying to detect individual slip events, but the stochastic noise that would arise as a sum of a large number of small events. Such noise might have a non-stationary nature, with power depending on the external perturbation, as predicted in Section 2.4.2. In particular, given the performance of the Advanced LIGO seismic isolation system, it is expected that the residual low frequency motion of the suspension cantilevers could excite broadband mechanical noise, resulting in non-linear up-conversion and a broad-band power spectrum of displacement noise, time-correlated with the driving force or force rate. Thus, an increased rate of larger events is expected when the stress or stress rate of the cantilever is increased with respect to the equilibrium position.

4.2 Measurement Methodology

The experiment is based on Michelson Interferometer configuration described in Chapter 1. The setup is designed to resolve transient differential motion of two identical cantilever blade tips under common mode stress excitation.

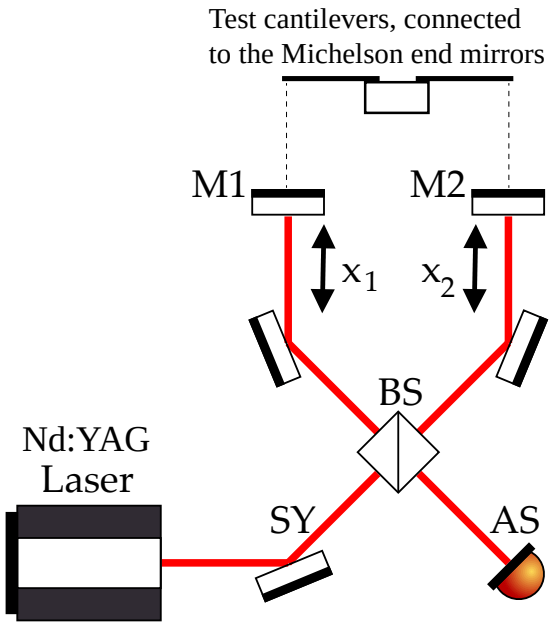

Figure 4.1 Simplified schematics of the Michelson Interferometer layout employed. Figure reprinted from [G. Vajente, et al. *Rev. Sci. Instr.* 87, 065107 (2016)], with the permission of AIP Publishing.

Figure 4.1 shows simplified schematics demonstrating the interferometer layout used in this experiment. x_1 and x_2 represent the motion of mirrors 1 and 2, which are suspended from the two test cantilevers. "SY" and "AS" refer to the "symmetric" and "anti-symmetric" ports, respectively. The setup transduces the differential displacement $\Delta x = x_1 - x_2$ to an optical signal $I_{AS/SY}$.

The testing cantilever samples are mounted symmetrically onto a central post to avoid modulation on optical gain. The blades are pre-curved, but loaded to be flat with a mass by wire. The Michelson end mirrors are mounted to the bottom of the mass, so the length change of the optical arm well represents the vertical motion of the blade tip. Sensor-actuator pair is applied to control or drive the two blades. Ideally, this differential signal gained by the optical layout would be the uncorrelated crackle events. The study focuses

on the possibility that non-linear phenomena could up-convert low frequency (below 1 Hz) excitations of the metals into high frequency (audio band) noise in their elastic regime.

The Michelson signal is investigated in two different states for statistical significance: with an additional oscillatory drive ON and up-conversion noise present, and with the drive OFF and no up-conversion noise present. In the designed experiment, a low-frequency ($0.2 - 2$ rad $\cdot$ s^{-1}) small amplitude (30 μm) common-mode drive is turned ON and OFF in sequent half-hour measurement segment.

4.3 Experimental Setup

4.3.1 Suspension System

The most important degree of freedom in the system is the vertical one, since it corresponds to the direction of the Michelson interferometer measurement. In the first prototype experiment[112], the sensitivity of the interferometer at frequencies below a few hundred Hz is dominantly limited by seismic noises. A double stage suspension systems is designed for seismic noise isolation.

The ground motion in a typical urban location is orders of magnitude larger than the targeted sensitivity of this experiment. The measured motion of the optical table showed a displacement noise of the order 10^{-8} m/$\sqrt{\text{Hz}}$ at $f = 10$ Hz, rolling off with frequency roughly like f^{-3}. Ideally, if the optical system is infinitely rigid and the two test cantilevers are perfectly equal, vertical motions of the optical board will be rejected as common mode variation of the Michelson arms. However, in practice, motions of the

optical board can couple to the differential signal via asymmetry of the Michelson configuration due to imperfections of the system.

Using a simple elastic model of the two cantilevers, the residual coupling of common vertical motion x_{comm} of the board to differential displacement x_{diff} of the two cantilever tips can be estimated as,

$$\frac{\mathrm{x_{comm}}}{\mathrm{x_{diff}}} \sim \left(\frac{f_0}{f}\right)^2 \left(2\frac{\delta f_0}{f_0} + \frac{\delta L}{L}\right), \tag{4.1}$$

where f is the measurement frequency, f_0 is the mean resonance frequency of the cantilevers, δf is the resonant frequency mismatch, L is the mean cantilever length from the clamping to the wire suspension point, and δL is the difference in cantilever lengths. The expression works in frequency range $f_0 < f < f_1$, where $f_0 \sim 2$ Hz and $f_1 \sim 150$ Hz is the first higher order resonance of the loaded cantilever.

A difference in the two resonant frequencies of about 5 mHz and a difference in the two lengths of 0.5 mm, well within machining tolerances, provide a common mode rejection factor of about 6000. The suspension system is designed as two cascaded stages with characteristic frequencies close to 2 Hz in order to provide an additional factor of 2000 of vertical isolation at 10 Hz.

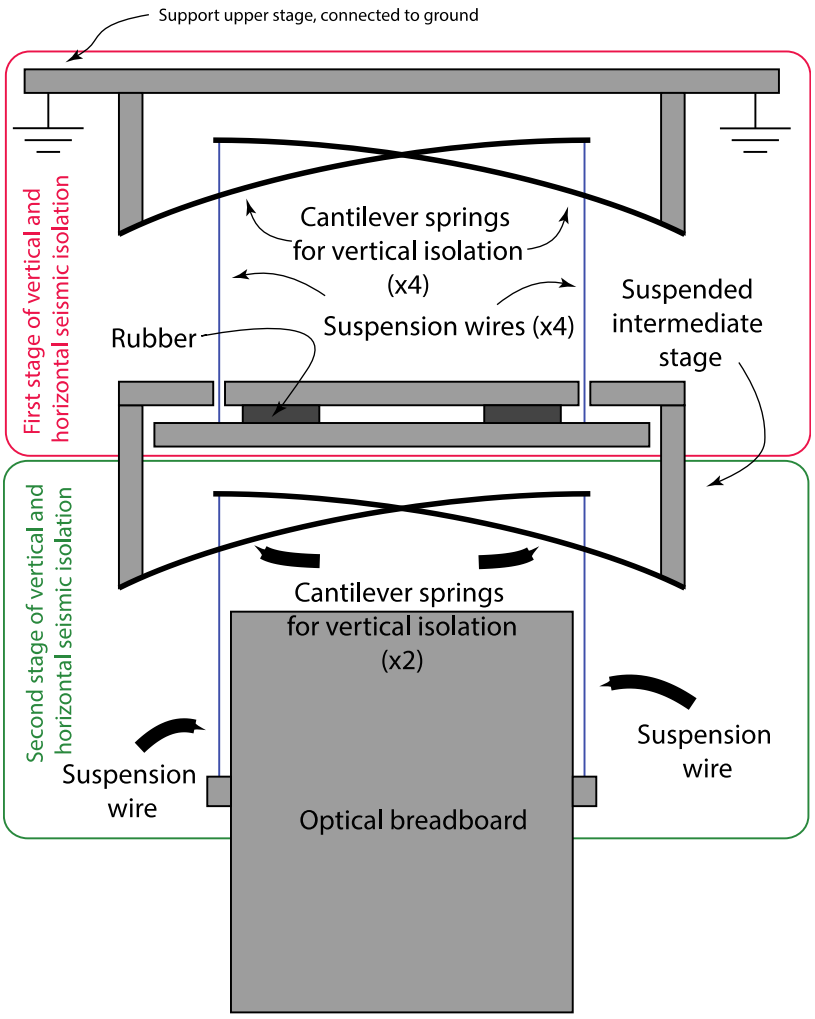

Figure 4.2 A simplified schematic of the seismic isolation system, highlighting the key components and the two stages of vertical and horizontal isolation. Figure reprinted from [G. Vajente, et al. *Rev. Sci. Instr.* 87, 065107 (2016)], with the permission of AIP Publishing.

Figure 4.2 shows a simplified schematic of the suspension system. Each stage is composed of maraging steel cantilevers, roughly 30 cm long, 7 cm wide, and 2 mm thick. Four cantilevers suspend the intermediate stage from a support structure with maraging steel wires, and two additional cantilevers support the optical breadboard from the intermediate stage, with another two wires attached to the sides of the board, above its center of mass. Each cantilever supports a load of about 10 kg, which corresponds to about 50% of their

yield stress. Both the optical board and the intermediate stage have a mass of about 20 kg. The intermediate stage includes a stack of rubber to provide some passive damping of the suspension resonant modes.

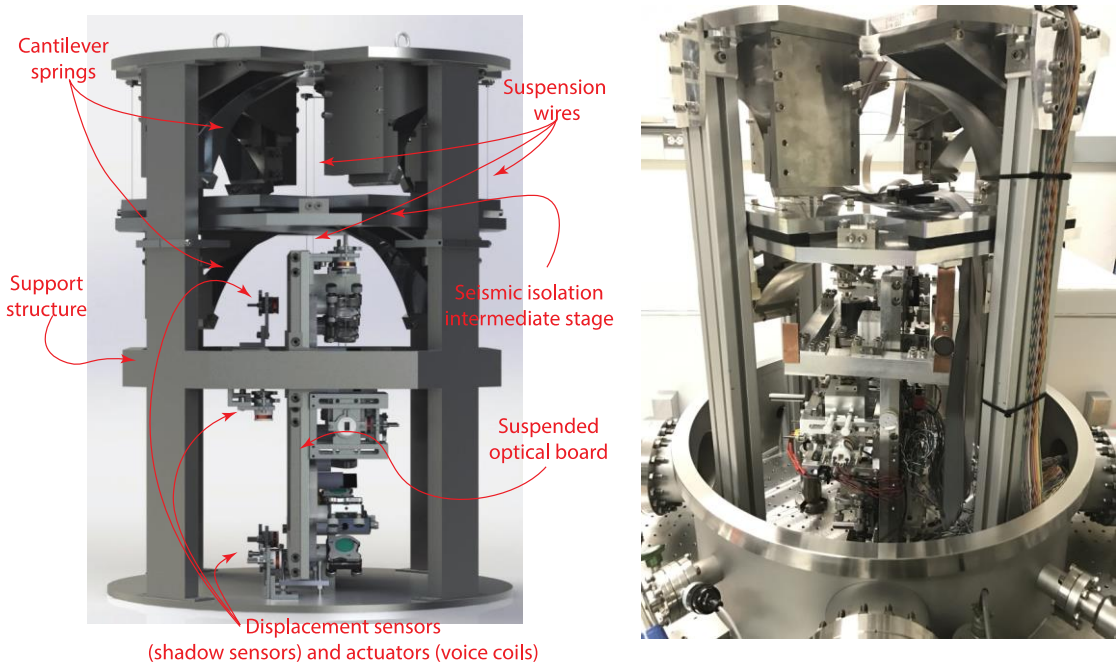

Figure 4.3 The 3-dimensional rendering (left, reprinted from [G. Vajente, et al. *Rev. Sci. Instr.* 87, 065107 (2016)], with the permission of AIP Publishing) as well as a photo (right) of the measurement apparatus showing the suspension system (Sec. 4.3.1), the vertically suspended optical breadboard (Sec. 4.3.2), and the displacement sensors and actuators for the board (Sec. 4.3.3).

Figure 4.3 shows a three-dimensional rendering in parallel with a photo of the suspended instrument. The optical board that holds the Michelson interferometer hangs vertically inside the support structure. The breadboard is suspended by two stages of vertical and horizontal isolation.

The suspended board is balanced by counter weights, shown for example in Fig 4.4 (a), to make sure the center of mass of the board is right below the suspension point. A laser

collimator is built for balancing reference: firstly, an optical board is mounted vertically to an optical table horizontally leveled using a spirit level. A He-Ne laser is mounted onto the optical board so its output beam passes through two far-separately irises mounted at the same heights on the table, so that the beam path is parallel to the optical table. One vertical edge of the optical board is aligned to a plumb line so the collimator setup can be transferred to another optical table that might not be leveled.

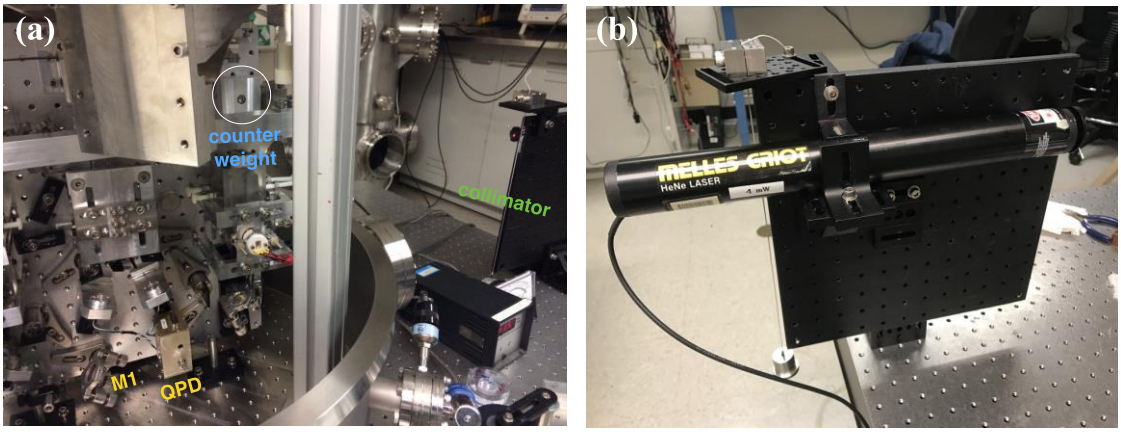

Figure 4.4 Board being balanced using counterweights and laser collimator. Quadrature Photodiode (QPD) is mounted at the back of the first steering mirror (M1) on the optical board.

The motions of the optical board and the load masses are sensed and controlled using Optical Sensor and Electro-Magnetic actuator (OSEM), the integrated optical position sensor and electro-magnetic actuator. Twelve OSEMs are installed to sense and actuate the total twelve degrees of freedom. Figure 4.5 shows the representative spectra of the three-axis free motions of the two load masses freely-suspended from the maraging steel blades.

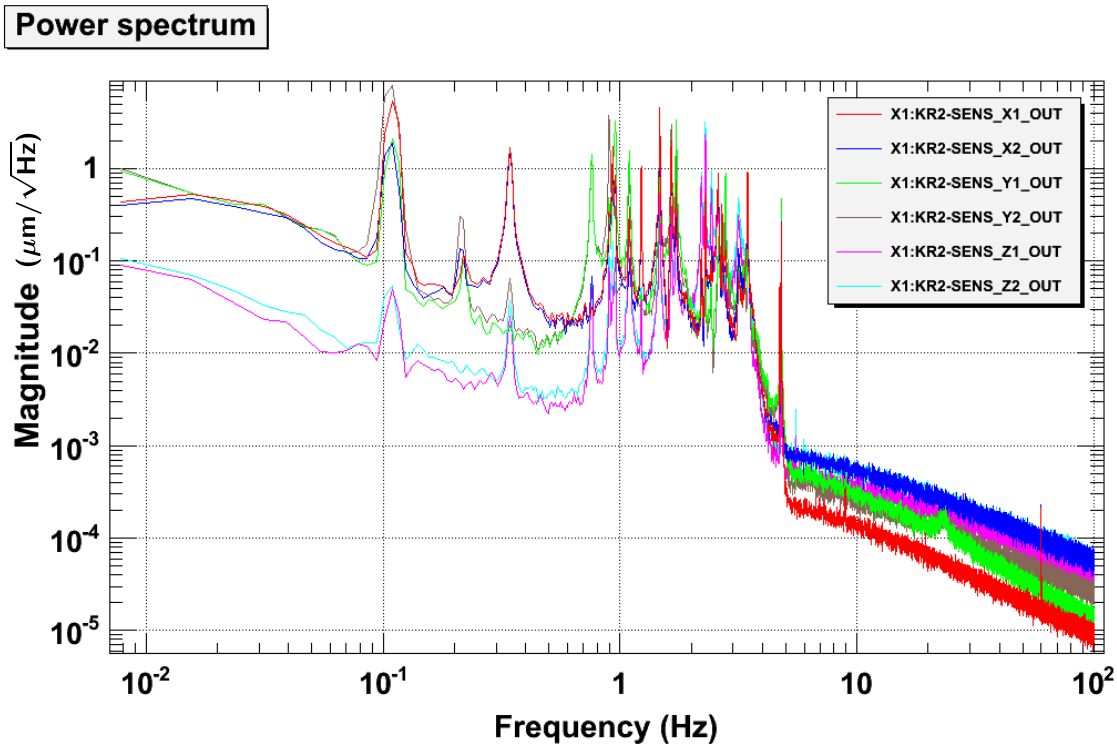

Figure 4.5 Reference OSEM spectrum of free suspension configuration taken in air.

The entire system is housed inside a vacuum chamber, to reduce contamination of the optics, noise due to air fluctuations, and acoustic disturbances.

4.3.2 Optical Setup

Figure 4.6 (left) is a schematic illustrating details of the optical setup based on Michelson configuration. Figure 4.6 (right) presents the schematics in overlap with a photo of the real experiment for comparison.

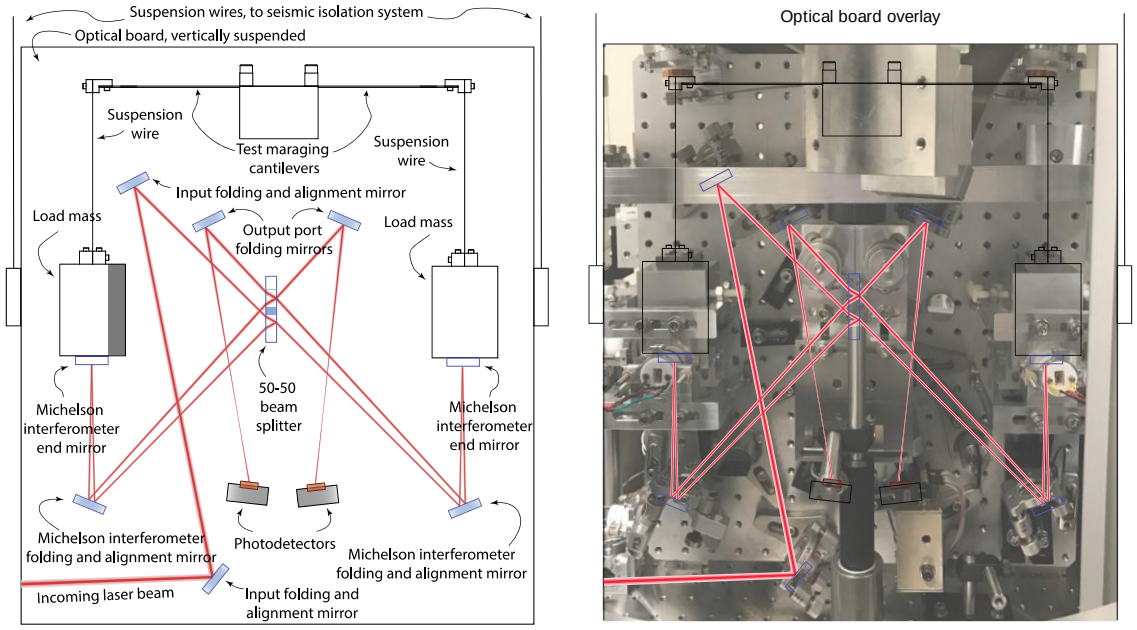

Figure 4.6 (Left) Simplified optical scheme of the Michelson interferometer, reprinted from [G. Vajente, et al. *Rev. Sci. Instr.* 87, 065107 (2016)], with the permission of AIP Publishing. (Right) The schematic optical paths in overlap with a photo of the optical board.

The macroscopic blades are prototypes of the cantilever blades used in the aLIGO suspension system. They have a dimension of about 12 cm length, 1.8 cm width, and 0.8 mm thickness. The blades are mounted symmetrically onto a central post. The blades are pre-curved and then loaded to be flat with a mass by wire. The Michelson end mirrors are glued to the bottom of the mass, so the length change of the optical arm well represents the vertical motion of the blade tip. A magnet is mounted at the tip of the blade so the blade can be controlled and driven by a shadow sensor - magnetic coil actuator pair.

4.3.3 Sensor-Actuator, Electronics, and Wiring

The Photodiode (PD) Transimpedance Amplifier (TIA) circuits are mounted to the back of the optical board in vacuum in order to amplify the diode signal at a closer stage. On

the back of the optical board is also mounted a counterweight driven by DC motor for precise balancing purpose. Picomotors are integrated to one of the end mirrors for Michelson alignment. The folding mirror in one of the Michelson arms (AS arm in this case) is mounted on a translational stage for Michelson arm lengths balancing.

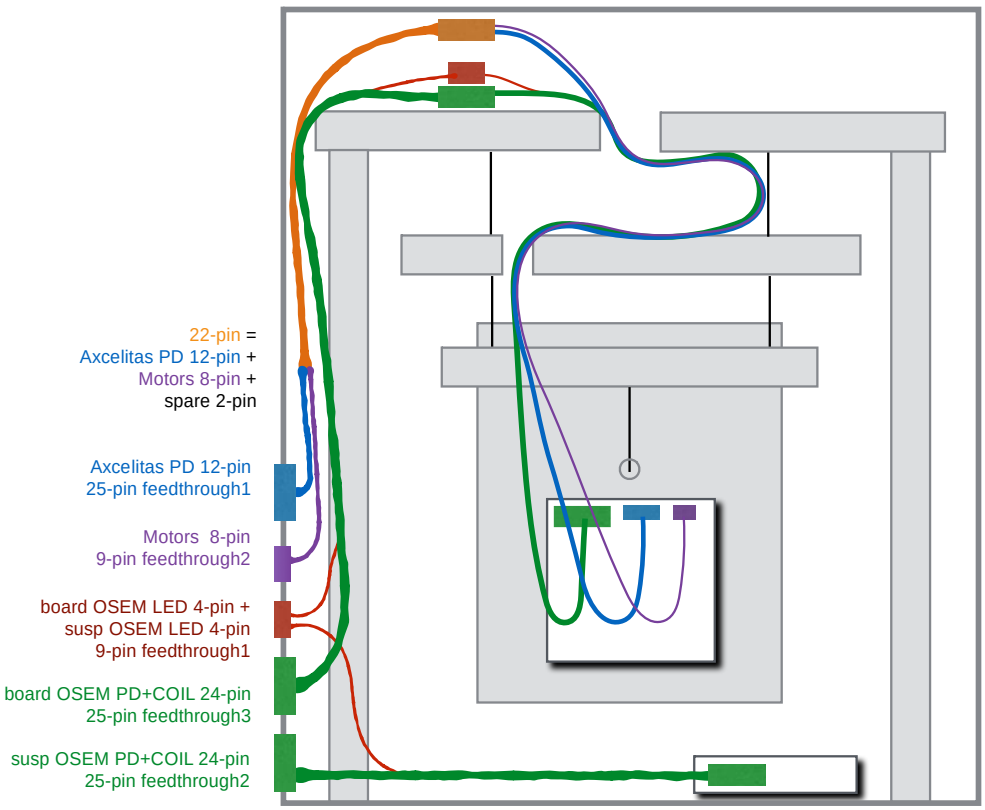

Figure 4.7 Vacuum feedthrough wiring through stages to avoid seismic noise short circuiting

The cabling and wiring configuration for all in-vacuum electronics is illustrated in Figure 4.7. The *solid lines* represent the more compliant flat cables for seismic coupling concerns. The flat cable is combed into thin wires for minimum stiffness and twisted at the back of the board toward the yaw mode in order not to stiffen the more critical roll mode. Outside

the suspensions the cables are swapped to twisted paired cables drawn as the *wavy lines* for electromagnetic field decoupling.

4.3.4 Lock Acquisition

Servo feedback is implemented to control the Michelson interferometer length at half-fringe, *i.e.* to *lock* the Michelson[113]. The Michelson error signal x_1 to be controlled is given by the difference of the two PD readings:

$$x_1 = I_{AP} - I_{SP}, \tag{4.2}$$

A simplified version of the control model is illustrated in Figure 4.8, where F is the servo filter composed of multiple digital filters with different functionalities designed for the locking purpose, A is the actuation function determined by the dual-cantilever blades mechanics, and H is the Michelson interferometer transducing the differential displacement of cantilever tips to an optical signal m. ADC and DAC are analog-to-digital and digital-to-analog conversion channels. Post ADC, A digital noise x_{exc} can be injected to the servo loop for characterization purpose. The total noise x_2 being passed to the servo filter is a sum of the injected noise and the measured error signal x_1. The servo filter outputs a control signal x_{out} to suppress differential motion of the cantilever tips. The DAC converts the control signal in addition to the prescribed common mode actuation signal x_A to an actuation voltage V_A to drive the coils. The ideal differential displacement signal due only to the microplastic deformation of the cantilever blades is denoted as dx, but in reality, other types of noises can couple through the slight asymmetry of Michelson

arms and contaminate the differential motion readout as dx_n (see Section 4.4 for details). The measured differential displacement is dx_s.

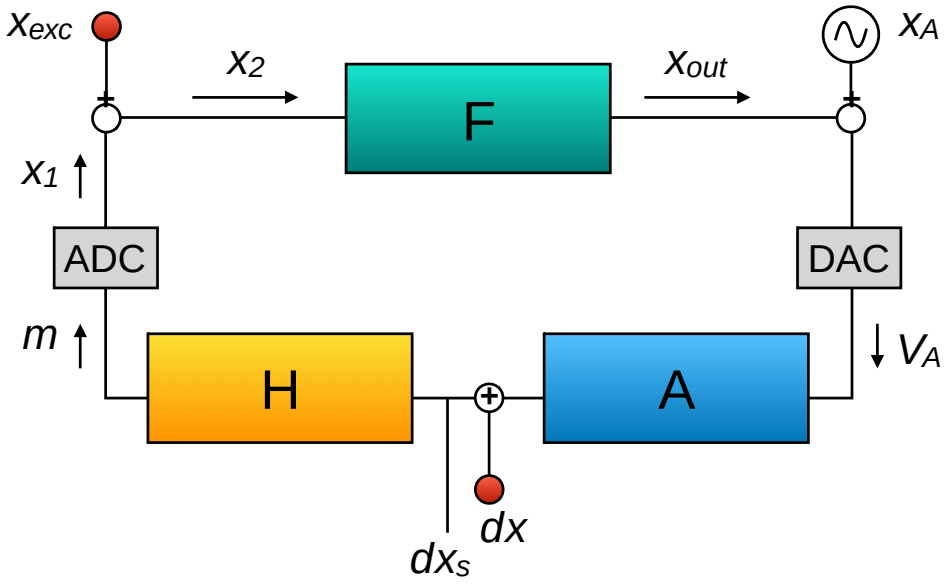

Figure 4.8 Simplified schematics for the SERVO model.

The primary *lock* filter is designed based on the double-blade actuation model. In order to engage the lock filter, *notches* filter that consists of multiple narrow-band band-stop filters is applied to avoid exciting high frequency motions with a high quality-factor that can cause loop instability.

When Michelson is locked in relatively low noise, the plant transfer function (TF) AH can be measured as $\frac{V_A}{x_1}$ with noise x_{exc} injection. The plant TF is expected to have the same shape as the actuation function A, because in locked condition the optical transducer transfer function H is simply a constant gain. The measured plant TF, as shown in Figure 4.9, follows primarily the expected shape of a double pendulum. The plant TF measurements can be well captured by a 10^{th} order model. A *plant compensator* filter can

be designed using a 2nd order fit to an inverse of the plant TF accompanied by a time-delay correction. A *boost* filter, *i.e.* a low-pass filter to boost control gain at low frequencies, can be engaged when the system is locked with enough phase margin (>30 degree). In addition, *resgain* filters can be designed to gain extra control over the low frequency resonance peaks of the mechanical system.

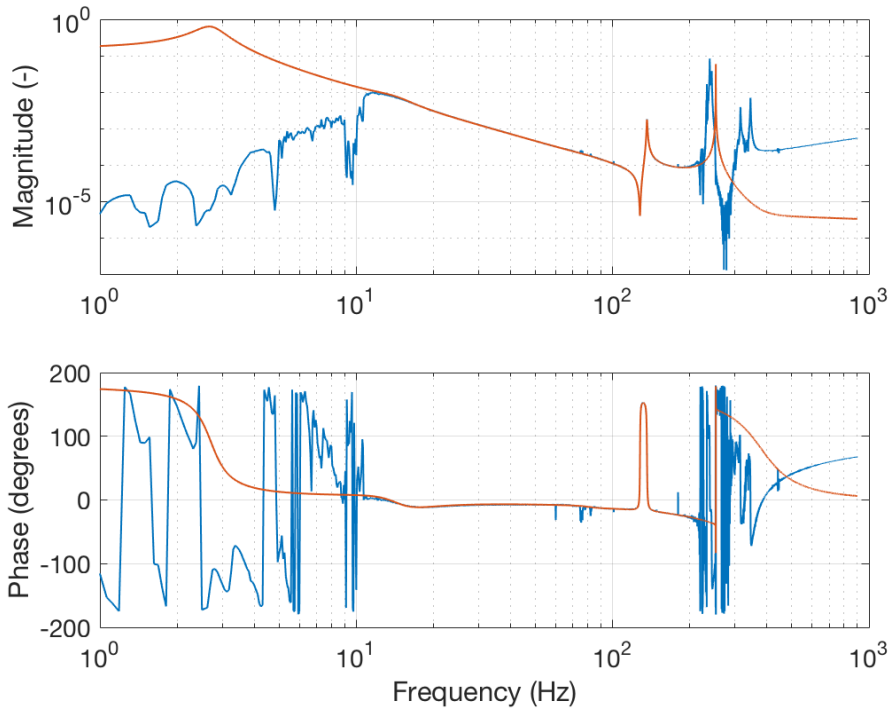

Figure 4.9 Measurement of the plant transfer function with noise injected to the loop. The plant can be fitted with a 10th order model. The pair-pole structure at ~ 136 Hz can be fitted with 2nd order model. A plant compensator lock filter is designed accordingly.

4.3.5 Michelson Signal Calibration

The optical gain of the setup can be measured and updated every time a new lock is acquired. A linear approximation for the optical gain estimation (See Section 1.4.2 for details) gives:

$$g = \left(\frac{2\pi}{\lambda} \cdot I_A\right)^{-1} \tag{4.3}$$

The peak to peak amplitude of the fringes I_A is estimated using minimum I_{min} and mid I_{mid} values (because maximum power of the fringes saturates the PD readings),

$$I_A = 2(I_{mid} - I_{min}). \tag{4.4}$$

The minimum value I_{min} is measured by taking averages of the time-windowed minimum of PD output while a 5 Hz noise excitation is injected to the servo loop to make sure the fringes run fast enough to reach their minimum within the time window. The mid value I_{mid} is taken as an average of PD readout when Michelson is locked at mid fringe.

The actuation function A is measured as the plant TF divided by optical gain. The compensated displacement can be calculated from the control signal c (in units of μN) through the actuation function. The differential displacement signal δx_s can be recovered:

$$\delta x_s = x_1 g^{-1} - Ac, \tag{4.5}$$

with proper dewhitening and whitening of the signal.

The quality of the calibration can be examined upon closed-loop transfer function (CLTF) measurements with x_{exc} noise injection, where, if A and g are properly measured and fitted, the calibrated CLTF should have the same shape as the measured CLTF:

$$\frac{x_1}{\delta x_s} \sim \frac{x_2}{V_{exc}} \,. \tag{4.6}$$

A sample comparison of the two-way CLTF measurements is shown in Figure 4.10.

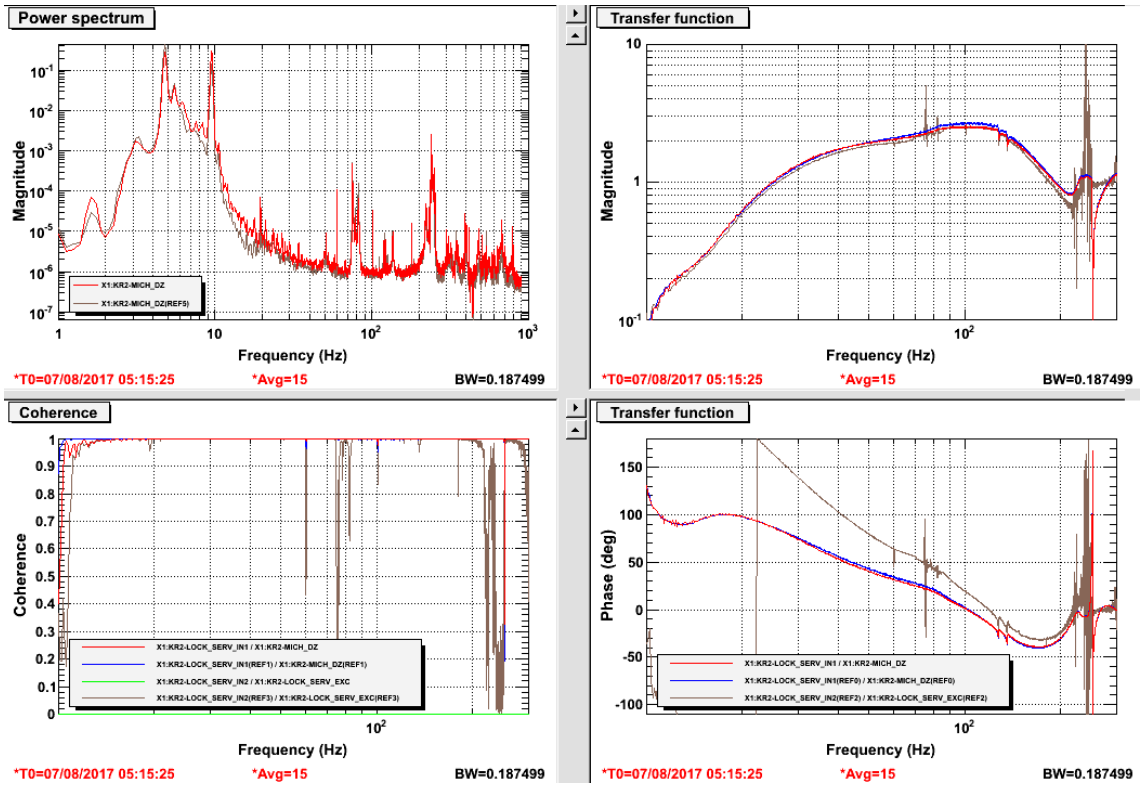

Figure 4.10 Two-way closed-loop transfer function measurements agree in shape when the Michelson signal is well calibrated.

4.3.6 Cantilever Samples

The maraging steel blade samples used in the table-top experiment are a scaled-down prototype of the cantilever spring blades used in the advanced LIGO suspension system.

They are manufactured using the same process for advanced LIGO. The basic chemical and mechanical properties have been examined in literature[106,110]. Figure 4.11 (a) shows a SEM image of a mechanically polished maraging steel sample, cut directly from the blade sample used in the experiment. Figure 4.11 (b) is an electron backscatter diffraction (EBSD) investigation on the polycrystalline grain structures, while the phase map shown in Figure 4.11 (c) confirms that maraging steel is in BCC phase.

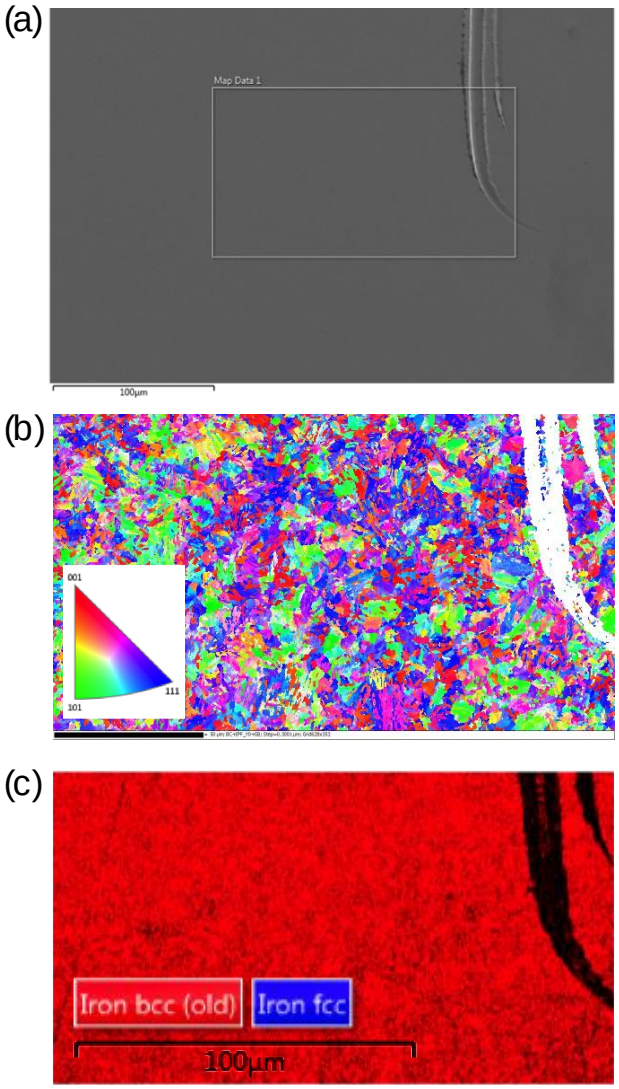

Figure 4.11 Electron backscatter diffraction investigation on a mechanically polished maraging steel sample. (a) SEM images of the sampled surface area, marked with sharp scratch. (b) EBSD

map of the same region shows a polycrystalline microstructure with average grain sizes of ~ 5 um. (c) a phase map of the same region shows that the crystal structure of maraging steel is BCC.

In order to investigate materials dependency, experiments with high carbon steel blades are done in the same setup. The high carbon steel is believed to be a crackling-noisy material because it exhibits large hysteresis in cyclic loading test, and is reported to inherit large internal friction damping[110,114]. The off-the-shelf AISI1074 steel is used as the experimental high-carbon spring steel materials. Electrical discharge machining (EDM) cuts the high-carbon steel strips into the same dimension as the maraging steel blades. The as-received blades are cold-rolled for pre-curvature.

Macroscopic mechanical tests on single pre-curved blades are done in Instron loading frame for a characterization of the basic mechanical behavior of the blades. A gripped tension configuration is applied to avoid the contact slip occurred in the compression test.

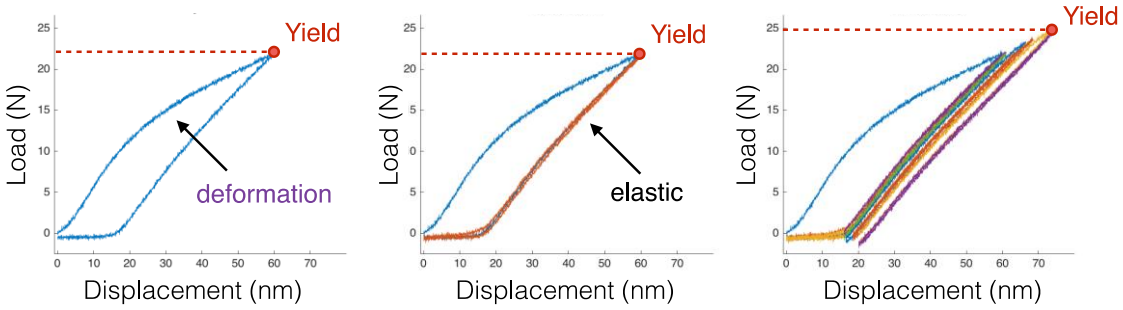

Figure 4.12 Cycling tension experiments on a single precurved blade in Instron loading frame showing a work hardened yield point evolution over maximum stress.

Figure 4.12 shows cycling tension experiments on a single pre-curved blade, where the blade yields quickly, followed by an elastic unloading. The re-loading process is then elastic because in macroscopic scale, the work-hardening defines the historically

maximum load as the new yielding point of the materials system (See also Chapter 3). The further increase in the maximum load will continue plastically deform the materials.

With this property, blades can be designed with the same thickness[2] but different initial pre-curvature and different deformation history to achieve a same load to load them straight; in the meantime the static load equals the desired percentage of the yielding of the blades. Since it's expected from the nanomechanical study that the higher the static load, the more crackling noise in the materials system, experiments are done with high-carbon blades loaded nominally at ~ 90% of the yielding.

4.4 Source of Noises and Sensitivity

4.4.1 Noise Budget

A *noise budget* is an accounting of the noises that add up to form the noise floor of the instrument. Figure 4.7 (a) shows the noise budget, generated using half-hour locked data in the maraging steel blades configuration, that investigates the amplitude spectral density of the total noise (*a.k.a.* the limiting sensitivity) along with variety of sources of noise. The counterpart noise budget for high-carbon steel blades configuration is shown in Figure 4.7 (b). The budgets take care of seismic and acoustic noise (Section 4.4.2), electronics (ADC and dark) noise (Section 4.4.3), laser intensity noise (Section 4.4.4), laser frequency noise (Section 4.4.5), beam scattering noise (Section 4.4.6), beam jittering

[2] The thickness of the blades is chosen carefully so the loaded high carbon steel cantilever has a desired resonance frequency close to that of the maraging steel cantilever (<2 Hz).

noise (Section 4.4.7), shot noise (Section 4.4.8), and voice coil actuation noise (Section 4.4.9).

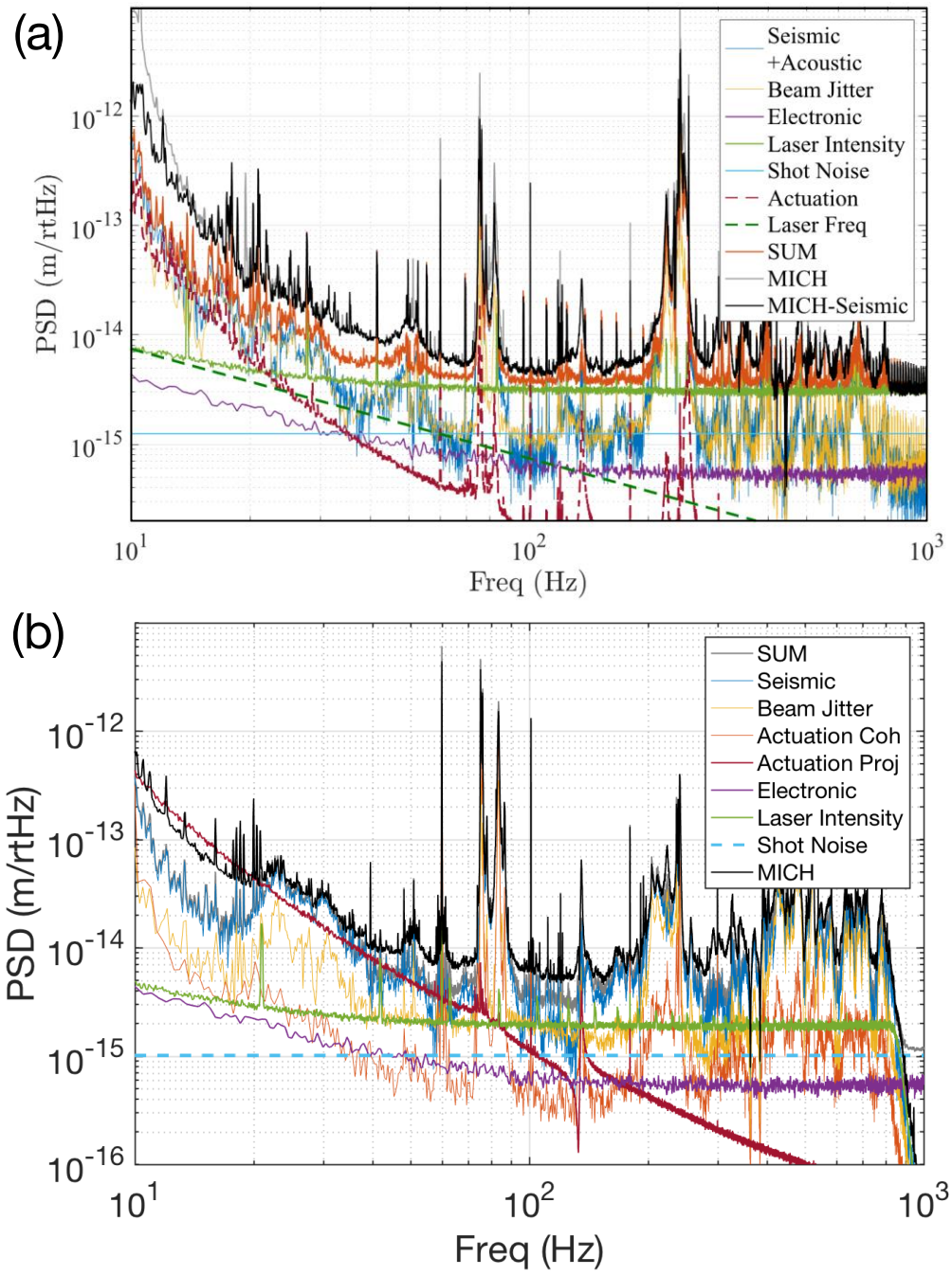

Figure 4.13 Noise budget for the Michelson setup installed with (a) maraging steel and (b) high-carbon steel cantilever springs

In the noise budget plots, the sum of all considered sources of noise (SUM) accommodates most part the measured Michelson sensitivity (MICH). Other sources of noise that can contribute to the discrepancy are beyond the scope of this study. The setup has achieved a displacement resolution on the order of $10^{-14}\mathrm{m}/\sqrt{\mathrm{Hz}}$ in the frequency range of 20 - 1000 Hz.

4.4.2 Seismic and Acoustic Noise

In the running experiment, the coupling from seismic and acoustic noise to Michelson signal can be measured using coherence projection. The seismic noises can be detected by a tri-axial Wilcoxon accelerometer. The environmental acoustic noise p is detected by a microphone. The inter-coupling between the three-axis seismic noise and acoustic noise measurements has to be considered. Using the accelerometer measurement $\boldsymbol{a} = [a_x; a_y; a_z]$ along with the microphone measurement p, multicoherence[3] function $mcoh_s$ between the Michelson signal $\mathbf{Y} = x_1$ and the multichannel noise $\mathbf{X_s} = [a_x; a_y; a_z; p]$ can be obtained. In frequency domain, the total noise $\widetilde{n_s}$ contributed to the Michelson signal from the seismic and acoustic noises can be estimated as $\widetilde{n_s} = \widetilde{x_1} \cdot mcoh_s$.

4.4.3 Electronics Noise

In the digital control system, analog-to-digital conversion (ADC) as well as digital-to-analog conversion (DAC) are common sources of noise. For ADC, the original analog

[3] An extension of the more common two-channel magnitude square coherence targeted to estimate the coherence of a target signal with a set of correlated auxiliary channels.

current signals from PDs are converted to voltage signals through the TIA stage described in Section 4.3.2. The dark noise n_{dark} of the PD contributes part of the total electronic noises. The analog voltage signal $s + n_{dark}$ is whitened and fed to the ADC channel. ADC adds additional noises n_{ADC} to the whitened signal. The signal is recovered by digital dewhitening filter designed as the inverse transfer function measured from the analog whitening stage $T_{whitening} = W_{out}/W_{in}$. The whitening process helps reduce ADC noise. The propagated residue electronic noise $n_e = n_{dark} + n_{ADC}$ can be estimated by measuring error signal $x_1 = s + n_{dark} + n_{ADC}$ when laser and room lights were off, that is, when $s \to 0$. The noise in error signal can be calibrated in time to a noise in Michelson signal using Equation 4.5. The DAC noise manifests itself as voice-coil actuation noise and will be specifically discussed in Section 4.4.9 in details.

4.4.4 Laser Intensity Noise

The coupling function from the laser intensity noise to the Michelson readout can be measured when intensity noise becomes a dominant source of noise for the system. The normal variation of laser power can be monitored in time as the sum of the photodiodes readings $I_{null} = I_{AP} + I_{SP}$. The excess intensity noise can be generated by modulating the laser current. Giving the total laser power $I'_{null}$with high relative intensity noise (RIN), the propagation term can be measured as a transfer function $G_I = dx'_s/I'_{null}$, where dx'_s is the Michelson signal measured with the noisy intensity laser input. The intensity noise can be projected as $n_I = G_I I_{null}$ using the high-frequency measurement of G_I.

4.4.5 Laser Frequency Noise

Following the field representation model of Michelson Interferometer configuration, the frequency noise of the laser dv is coupled to the Michelson signal dx_s as

$$dx_s = \frac{dv}{\nu_0}\,\Delta L, \tag{4.7}$$

where ν_0 is the laser frequency, $\nu_0 = \frac{c}{\lambda} = \frac{3\times10^8 m\cdot s^{-1}}{1064\times10^9 m} = 2.8195\times10^{14}$Hz, and dL is the macroscopic differential arm length. The Nd:YAG master laser has a typical free-running frequency noise $n_v = dv$ at the level of $\sim 100\frac{Hz}{\sqrt{Hz}} \times 100\frac{Hz}{f}$, where f denotes the spectral frequency.

The coupling term from laser frequency noise dv to Michelson signal can be estimated as $G_f = \frac{\Delta L}{\nu_0} = \frac{dx_s'}{n_v'}$ when frequency noise n_v' is injected to the laser source by piezo driving the lasing crystal. A flat magnitude shape can be obtained for $|G_f|$ when taking measurements with >0.6 coherence. Figure 4.14 shows a sample transfer function measurement.

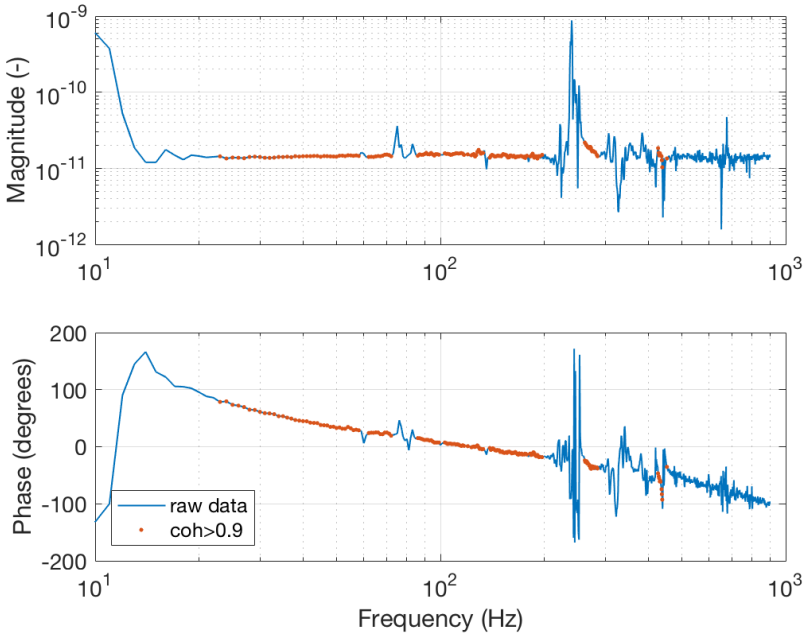

Figure 4.14 A Bode plot of the frequency noise to Michelson signal coupling transfer function.

The Michelson arm balance can be improved to reduce the frequency noise coupling. The arm length difference ΔL can be measured as,

$$\Delta L = \frac{\nu_0}{d\nu}\frac{m}{G_f}. \tag{4.8}$$

with a single frequency line (1111 Hz) 20 kHz amplitude frequency noise $d\nu$ injected to the laser. The asymmetry can be reduced by moving the translational stage (onto which one folding mirror is mounted; see Section 4.3.3 for details).

4.4.6 Beam Scattering

The Michelson signal can be contaminated by *ghost beam* scattered from moving elements. Ghost beam refers to the beam that deviates from the designed optical path (See Section 4.3.2 for details of the optical path) and is not properly dumped. The motion of the

scattering element z causes phase shift $\phi \in [0, \frac{2z}{\lambda}]$ of the scattered light, which will result in a noise plateau in frequency range $f \sim |\dot{\phi}| \in \left[0, \frac{2}{\lambda}|\dot{z}|\right]$ in the Michelson spectrum with a corner frequency,

$$f_{max} = \frac{2}{\lambda} v, \tag{4.9}$$

where $v = |\dot{z}|$ is the speed of the scattering element. The scattering noise is usually non-stationary. When the Michelson sensitivity is limited by scattering noise, the band-limited root-mean-square (BLRMS) of the Michelson signal can correlate significantly in time to motions of some optical elements. Spectrogram analysis on Michelson signal can be applied to diagnose for beam scattering. Figure 4.15 shows (a) the spectrogram analysis of an example Michelson measurement. In the configuration, the low-frequency Michelson BLRMS are detected to have high coherence with the end mirror motion quantified as $\frac{d}{dt}|z_1 + z_2|$, where z_1, z_2 are OSEM measurements for the two blade tip motions. Figure 4.15 (b) shows that the time-varying low-frequency noise plateau cutoff overlaps perfectly with the corner frequency estimation $f_{max} = \frac{2}{\lambda}\frac{d}{dt}|z_1 + z_2|$.

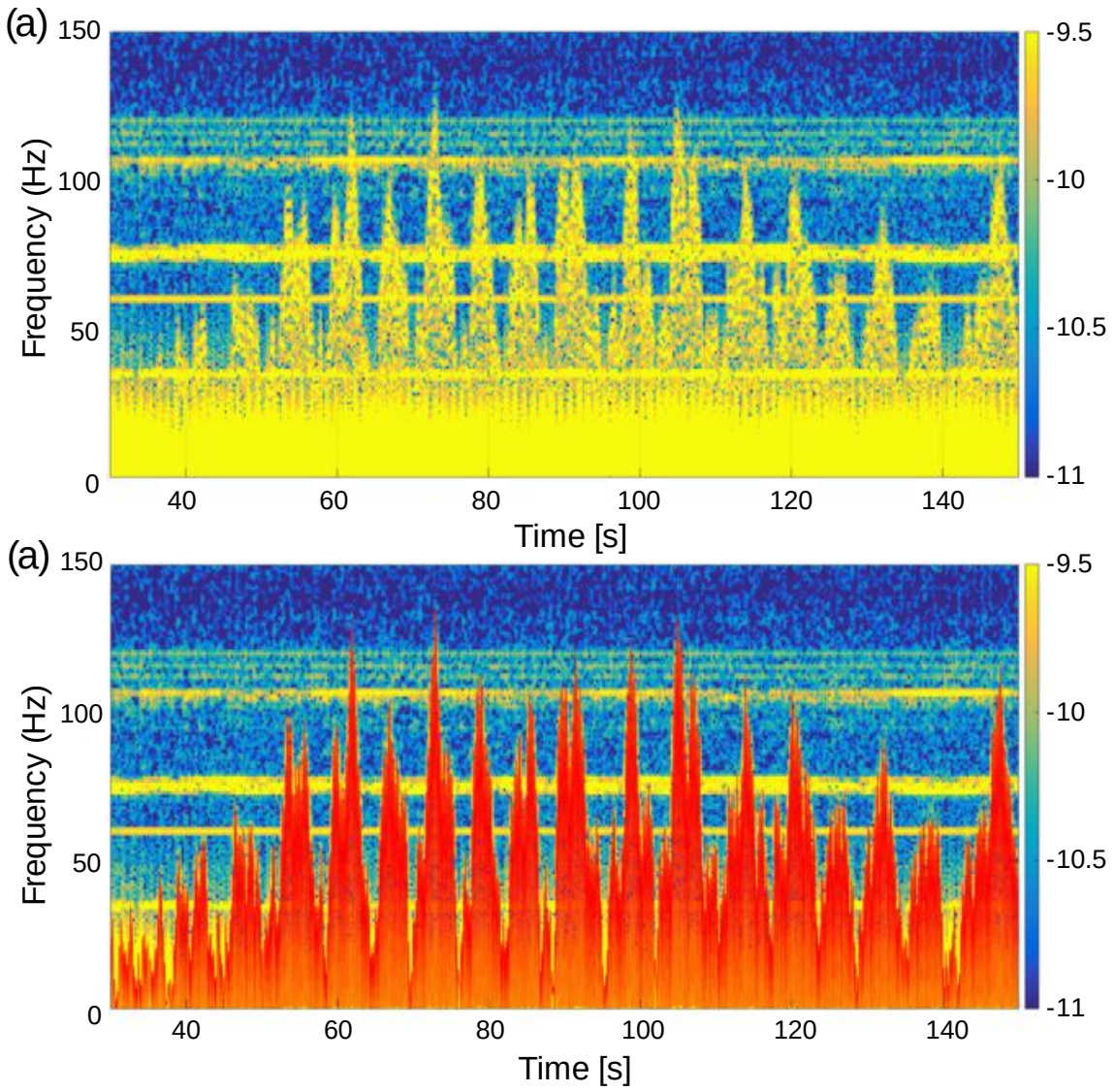

Figure 4.15 Spectrogram of Michelson signal in a configuration where spurious beam is a dominating noise source. (a) The spectrogram shows that the Michelson signal is non-stationary. (b) The time-varying low frequency noise plateau (yellow) cutoff overlaps perfectly with the corner frequency calculated from scattering noise estimation (red).

When scattering noise dominates the low-frequency Michelson behavior, beam scattering noise contribution can be estimated from measurements of the mirror motion $z = |z_1 + z_2|$. The calculation follows a simple field model and assumes that a fraction r_{sc} of the

beam power impinging on the mirror is scattered back and couples again with the main beam. The field arriving at the photodiode is perturbed by the scattered light:

$$\psi = \psi_0 + \sqrt{r_{sc}}\,\psi_0\, e^{i\frac{4\pi}{\lambda}z}. \tag{4.10}$$

The power read by the photodiode becomes,

$$I = I_0(1 + r_{sc}) + 2I_0\sqrt{r_{sc}}\cos\left(\frac{4\pi}{\lambda}z\right). \tag{4.11}$$

The beam scattering noise n_{sc} can be estimated by assuming uncorrelated scattered light from single bounce from the two end mirrors:

$$n_{sc} = g \cdot 2I_0\sqrt{r_{sc}}\sqrt{\cos^2\left(\frac{4\pi}{\lambda}z_1\right) + \cos^2\left(\frac{4\pi}{\lambda}z_2\right)}, \tag{4.12}$$

where g is the optical gain, and a maximum r_{sc} is chosen to match the low frequency sensitivity in the Michelson spectrum. The sample projection for the noisy case (with the presence of spurious beams) is shown in Figure 4.16 with the scattering fraction computed to be $r_{sc}\sim 10^{-8}$.

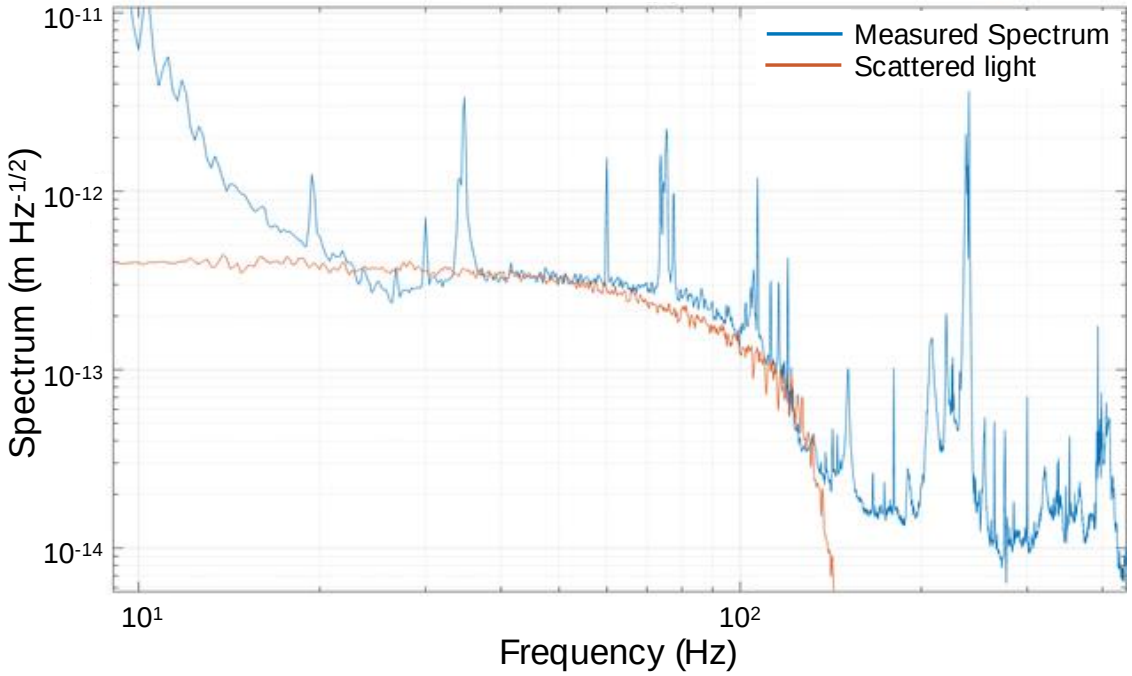

Figure 4.16 A projection of beam scattering noise for the example case with presence of spurious beams.

Figure 4.17 below shows the spectrogram analysis of the Michelson signal sampled from a quiet measurement segment. The spectrogram is superimposed with the corner frequency profile estimated from the in-time end mirror motion measurement.

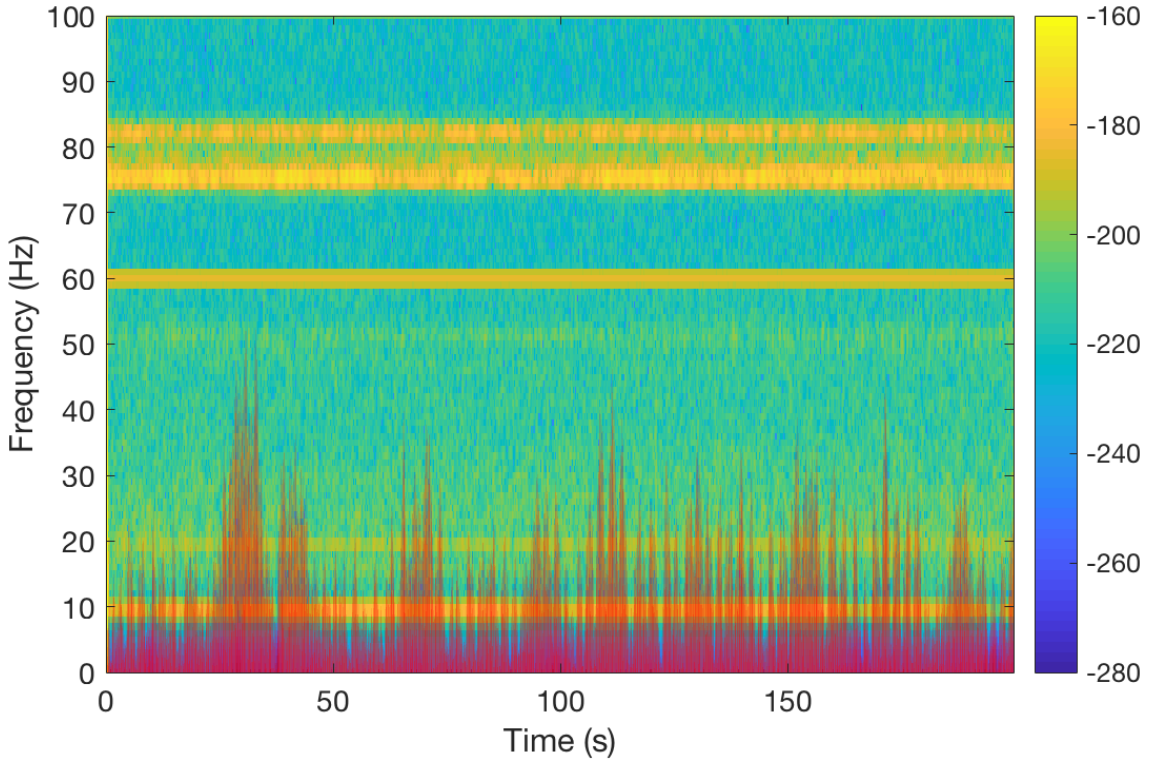

Figure 4.17 Sample spectrogram analysis of high-passed Michelson signal during quiet measurement period superimposed with the corner frequency profile estimated from end mirror motions.

The signal is high-passed to avoid spectral leakage caused by short FFT windowing. The spectrogram analysis shows a relatively stationary Michelson behavior (in contrast to the noisy case shown in Figure 4.15) and resolves no correlation between the mirror motion and the Michelson signal.

4.4.7 Beam Jitter

A Quadrant Photodiode (QPD) is installed onto the optical board after the first steering mirror (M1) for in-time beam jitter measurements. The location of the QPD is shown in Figure 4.4. The QPD uses the transmitted beam from M1 ($\sim$ 99% reflectivity) with a power of $\sim$ 0.1 mW to measure the 2-dimensional motion of the beam on optical elements.

The beam is centered on the QPD within the ~ 1 mm linear sensitivity range. The transducing factors are calibrated ex-situ using translational stage to be $g_x = 6.98\ \mathrm{V/mm}, g_y = 6.22\ \mathrm{V/mm}$. The QPD readout works also as a reference point for in-vacuum Michelson alignment purpose. The noise contribution from beam jittering to the Michelson sensitivity is estimated using coherence projection $n_j = dx_s \cdot mcoh_j$, where $mcoh_j$ is the multi-coherence between $\mathbf{Y} = dx_s$ the Michelson signal and $\mathbf{X} = \left[I_{QPD}^x; I_{QPD}^y\right]$ is the multichannel QPD measurement of beam jitter in x- and y- direction.

4.4.8 Shot Noise

Shot noise is one of the fundamental limits of the laser interferometer techniques that depends on laser power[115]. The shot noise level at all frequencies is given by equation

$$n_{shot} = \sqrt{2 \cdot h_p \cdot \nu_0 \cdot I_{input}}\,, \tag{4.13}$$

where h_p is the plank constant, ν_0 is the laser frequency, and I_{input} is the total input laser beam power, which is $\sim 18\ \mathrm{mW}$, and estimated in time by the sum of AP and SP photodiode readings $I_{null} = I_{AP} + I_{SP}$.

4.4.9 Actuation (DAC) noise

The actuation noise can be highly nonlinear due to digital discretization or harmonic distortion of DAC. This type of digital noise can be uncorrelated in the two actuation channels, and therefore can be coupled to the Michelson signal in a similar way as crackling noise.

A current monitor is implemented to directly measure the current sent to the interferometer coil actuators. The measurement is initially limited by sensing noise. A low-noise 10X instrumentation amplifier is installed to achieve an intrinsic sensing noise lower than the one produced by the DAC driving the coils. The sum of the two current monitor readouts is a direct estimation of the DAC noise that can induce transient differential driving force on the blade tips. This force noise can project to the differential motions of the cantilever tips through the actuation transfer function (See Section 4.3.4 for details).

With the Michelson locked, the coil current monitors see only the control signal. The transfer function $C_{currmon} = x_{out}^{servo}/x_{in}^{currmon}$ gives a direct calibration of the current monitor input (in ADC counts) in units of the control signal (μN). The resulting TF, as shown in Figure 4.18 (a), is flat in magnitude above 10 Hz, and follows the shape of the whitening filter of the current monitor (not of the coil driver) below 10 Hz. The calibration filters are designed by fitting $C_{currmon}$ for each coil.

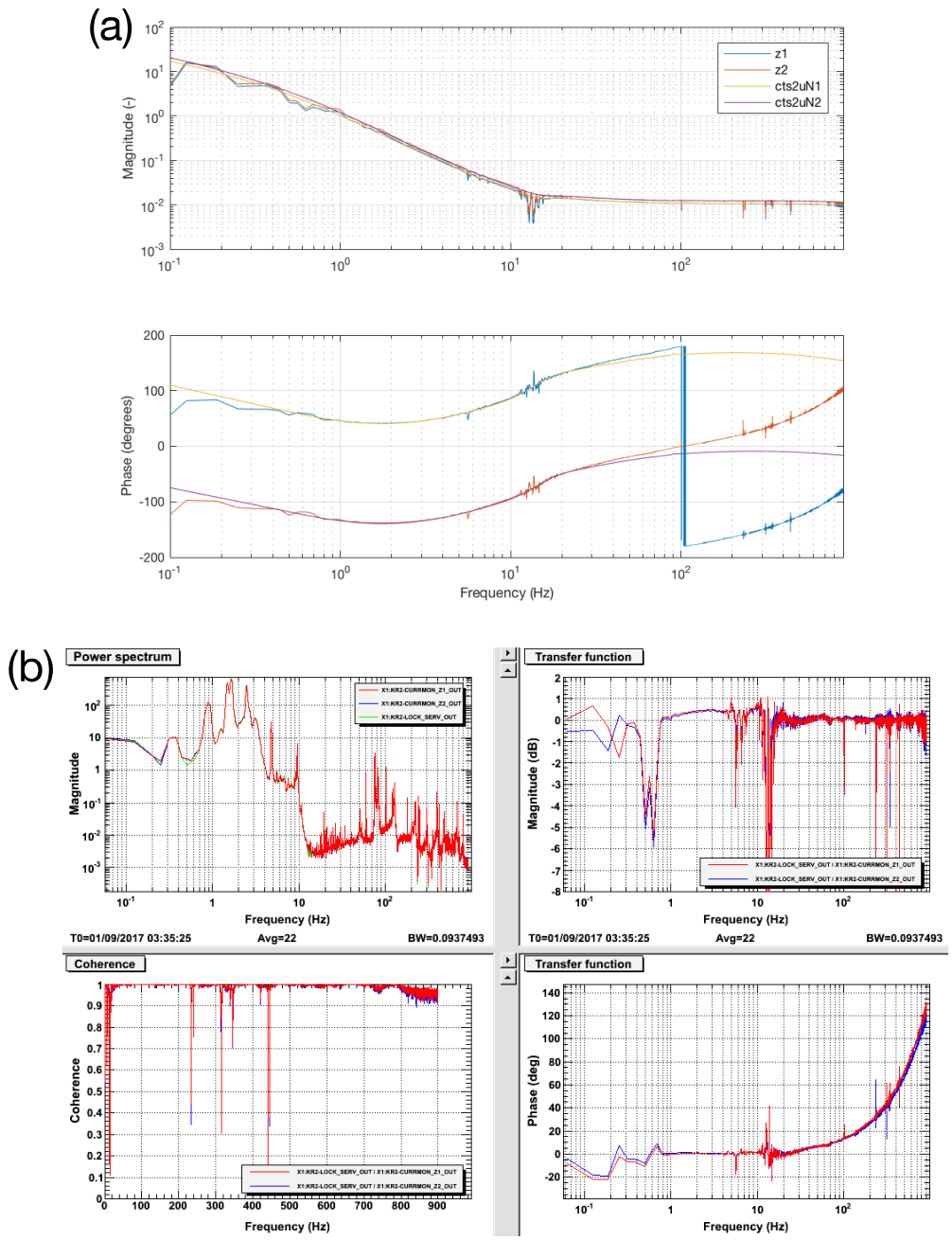

Figure 4.18 Current monitor measurement calibration. (a) The transfer function between current monitor input and the locking control signal measured when Michelson is locked, the fitted model of which calibrates the current monitor input in units of the control signal. (b) The transfer function measured between current monitor output and the control signal checks the performance of the current monitor calibration.

After applying the calibration filter, the current monitor output $x_{out}^{currmon}$ should be equal to the control signal x_{out}^{servo}. Whether the current monitor signal is properly calibrated can

be checked by measuring directly the transfer function $x_{out}^{servo}/x_{out}^{currmon}$. The measurement for an example setup is shown in Figure 4.18 (b). The measured transfer function has unity gain at all frequencies. The phase rotates away from zero starting from frequency ~ 20 Hz. but in the same way for z_1 and z_2 calibration. Since it is the noise power, *i.e.* the $dz = z_1 + z_2$ spectrum, that matters in the end, this common phase delay should not affect the results of the upconversion noise analysis to be described soon in Section 4.5.

4.5 Upconversion Noise Demodulation

In Chapter 2, the microscopic investigation on microplasticity predicts a form of crackling noise arising under slow varying stress modulation. Specifically, Section 2.4.2 describes how the predicted noise amplitude changes under an external oscillatory stress. The primary goal of the data processing is to quantify the noise power being modulated, or upconverted by the low-frequency stress excitation. A demodulation analysis based on Fourier series analysis is developed to extract the collective results of the mechanical upconversion noise predicted by the micromechanical study at multiple driving frequency components.

4.5.1 Demodulation Analysis

In Section 2.4.2, Figure 2.11 predicts that the simulated crackling noise arising from microplastic deformation of metals has an amplitude that goes up and down with the sinusoidal stress. If a sinusoidal force,

$$F_0(t) = F_0 \sin(\Omega t)\,, \tag{4.14}$$

is applied, due to the physical coherence between the crackling noise power and the driving, the noise amplitude A can be extracted by a Fourier series expansion of the total signal power $s^2(t)$, with the basis frequency being the driving frequency Ω:

$$s^2(t) = A_{1I}\sin(\Omega t) + A_{1Q}\cos(\Omega t) + A_{2I}\sin(2\Omega t) + \cdots \tag{4.15}$$

The above equation sets the definition of in-phase and quadrature signals with respect to the driving force:

$$\begin{aligned} &\sin(\Omega t) \to 1I, \\ &\cos(\Omega t) \to 1Q, \\ &\sin(2\Omega t) \to 2I, \\ &\cos(2\Omega t) \to 2Q \ldots \end{aligned} \tag{4.16}$$

The Fourier amplitude A_K can be estimated by averaging the signal power multiplied by the corresponding Fourier term $K = 1I, 1Q, 2I, \ldots$ in a finite time stretch T:

$$A_K^T = < s^2 \cdot K >_T. \tag{4.17}$$

A band-pass filter can be applied to the signal to investigate band-limited noise behavior in specific frequency range $\boldsymbol{f} = [f_1, f_2]$. The band-limited crackling noise power density $P_{K;\boldsymbol{f}}$ can be computed from the band-limited Fourier amplitude, $A_{K;\boldsymbol{f}}^T = < s_{\boldsymbol{f}}^2 \cdot K >_T$, where $s_{\boldsymbol{f}}(t)$ is the band-passed signal:

$$P_{K;\boldsymbol{f}}^T = \frac{2 \cdot 2}{\Delta f} \left| A_{K;\boldsymbol{f}}^T \right|. \tag{4.18}$$

In the normalization pre-factor, $\Delta f = |f_2 - f_1|$is the analysis bandwidth. The first factor two comes from $< \sin^2(\Omega t) > = < \cos^2(\Omega t) > = 0.5$; the second factor of two comes from single-to-double sided power spectrum conversion. The mean and standard error of $P_{K;\boldsymbol{f}}$ can be obtained from multiple T time window sampling. This demodulation process is expected to help distinguish the crackling noise from other stationary, or non-stationary but driving-uncorrelated background noise.

4.5.2 Sinusoidal Noise Demodulation

In order to validate the demodulation analysis, the first thing to do is to apply the analysis to a controlled, manually generated signal that is being modulated in a known fashion. A general form of such signal $s(t)$ is:

$$s(t) = b(t) + G(t)n(t), \tag{4.19}$$

where $b(t)$ is the background random noise, and $n(t)$ is the noise modulated by a time varying function $G(t)$. The signal power is

$$s^2(t) = b^2(t) + G(t)b(t)n(t) + G^2(t)n^2(t). \tag{4.20}$$

When averaged over a timescale that is fast for the noises $b(t)$ and $n(t)$ but slower with respect to the characteristic timescale of $F = G^2(t)$, the signal power becomes

$$s^2 = b^2 + F\, n^2, \tag{4.21}$$

where $s^2 =< s^2(t) >, b^2 =< b^2(t) >, n^2 =< n^2(t) >$. The coupling term $G(t) < b(t)n(t) >$ goes to zero because $b(t)$ and $n(t)$ are independent. A simple form of modulation on n^2 is a sine wave acting on n^2, *i.e.* $F(t) = \sin(\Omega t)$. Following the

demodulation process described in the previous section, the noise power (with analysis bandwidth of Δf), for example, modulated in phase at the frequency 1Ω, would be,

$$
\begin{aligned}
P_{1I;f} &= \frac{4}{\Delta f} < s^2(t) \cdot \sin(\Omega t) > \\
&= < (b^2 + \sin(\omega t)\, n^2) \sin(\omega t) > \\
&= < \sin(\omega t)\, b^2 + \frac{\cos(2\omega t) + 1}{2} n^2 > \\
&= < \sin(\omega t) > b^2 + \frac{1}{2} < \cos(2\omega t) > n^2 + \frac{1}{2} n^2 \\
&= \frac{2}{\Delta f} n^2.
\end{aligned}
\tag{4.22}
$$

For testing purpose, a data train s is created as a sum of a stationary background noise b and a signal n. The background noise has a flat spectrum with amplitude of $1/\sqrt{Hz}$. The signal spectrum is shaped like $1/f$ and is modulated by a sinusoidal function $F(t)$ at any frequency and phase. The demodulation analysis is applied to the band-passed data to investigate the spectral frequency dependency of the demodulated signal. The demodulation analysis on the simulated sinusoidally-modulated data reconstructs the correct signal spectrum.

4.5.3 Generic Noise Demodulation

The demodulation technique is also tested against a more generic form of modulated signal. In general, the noise amplitude can follow any modulation shape. In particular, a

noise mimicking the simulated microplastic noise (Sec 2.4.2) is produced: the amplitude is everywhere zero but has a smooth peak around the maximum of the drive.

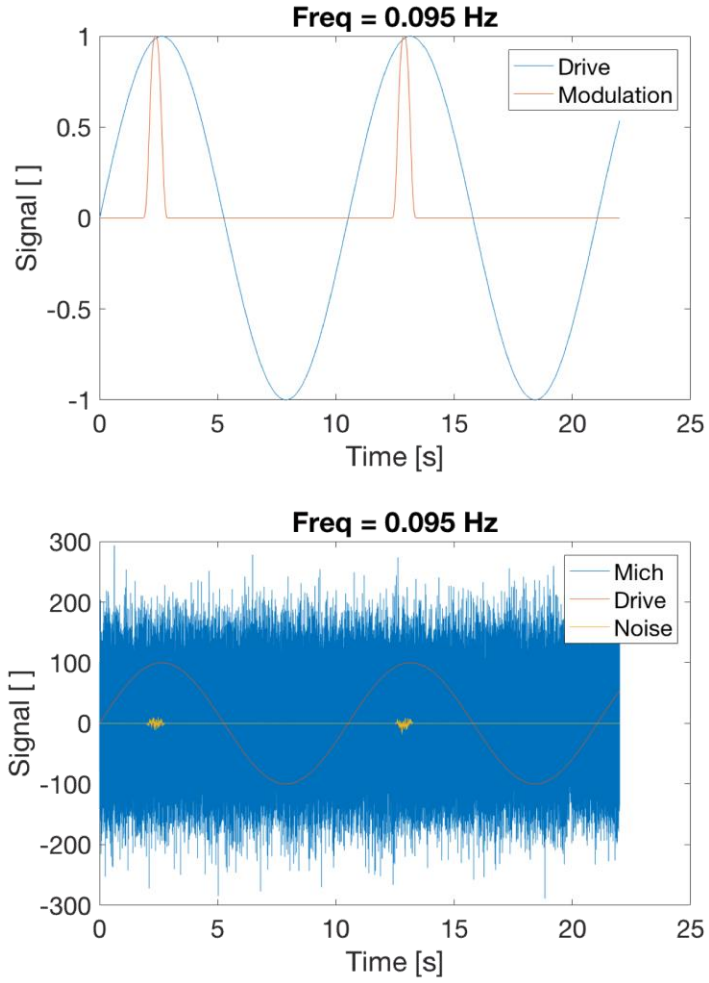

Figure 4.19 A generic form of noise with a prescribed amplitude of 1 and modulation frequency at 0.095 Hz is generated to mimic the simulated crackling noise as shown in Figure 2.11.

In the sample simulation, the background noise has a flat spectrum of amplitude $1/\sqrt{Hz}$. The signal is constructed as follows: An additional random noise is low-passed from 10 Hz to be shaped like $1/f$. The modulation shape is constructed by convolving a square wave with a Hanning window. The square wave function has an amplitude of 1 in the time window $0.2\,T_0 - \ 0.25\,T_0$, where $T_0 = 2\pi/\Omega$ is the driving period. The Hanning window

has the same width ($0.05\ T_0$) as the square wave. The sample segment of generated noise is plotted in contrast with the total noise and in parallel with the prescribed driving in Figure 4.19. The demodulation analysis on the simulated generically-modulated data reconstructs the prescribed signal form and amplitude.

4.5.4 Simulated Crackling Noise Demodulation

The simulation noise injection tests described and validated in the previous sections can be applied to the simulated crackling noise data. The microplastic simulation is based on the microscopic model described in Sec. 2.3.1. Using the same simulation parameter for single-crystalline copper, N number of samples can be generated independently with the randomness inherited in the different initial dislocation configurations. The load function is prescribed in accordance with the crackling noise experiment condition, *i.e.* a quasistatic stress plus a superimposed small-amplitude oscillatory stress. The same load function is applied to all the samples and the strain response of each sample is computed. One crackling noise measurement can be acquired as the differential strain rate from two independent samples. $\binom{N}{2}$ combination pairs of differential strain response can be constructed from simulation results from N number of independent samples through bootstrapping. The ensemble result is a mean square of the differential strain rates,

$$< \delta\dot{\epsilon} > = \frac{1}{N}\sum_{ij} (\dot{\epsilon}_i - \dot{\epsilon}_j)^2. \tag{4.23}$$

According to the preliminary microscopic simulation prediction (see Chapter 2 for details), the driving frequency is one of the most important parameters that affect the demodulated

noise behavior (See Figure 2.7). Different driving frequency tests are simulated for a driving frequency dependency study.

Figure 4.20 shows the sample demodulated amplitudes $A_{K;\boldsymbol{f}} = \sqrt{P_{K;\boldsymbol{f}}}$ of signals band-passed in frequency range 20-25 Hz vs. the number of testing segments, where $P_{K;\boldsymbol{f}}$ is defined by Equation 4.18. The statistical results are obtained from bootstrapping differential strain rate measurements from $N = 8$ independent simulation samples. For each sample, a quasistatic stress at 75% of the nominal yield stress is applied (See Section 2.4.2 for details). An oscillatory drive is turned ON and OFF sequentially around the quasistatic stress. One simulation test contains sixty driving ON/OFF segments. Each segment lasts 1000 seconds. The driving stress amplitude during the ON segments is prescribed to be 10% quasistatic stress and is zero during the OFF segments. The driving frequency for the sample simulation run is $1\ \mathrm{rad} \cdot \mathrm{s}^{-1}$.

The demodulated noise amplitude $A_{K;\boldsymbol{f}}$ is analyzed in each driving segments following the demodulation process described in Section 4.5.1. In the figure, the ON-segment results are marked in red, while the OFF-segment results are marked in blue. The demodulated amplitude during ON segments settles to relatively constant finite values after ~ 30 cycles.

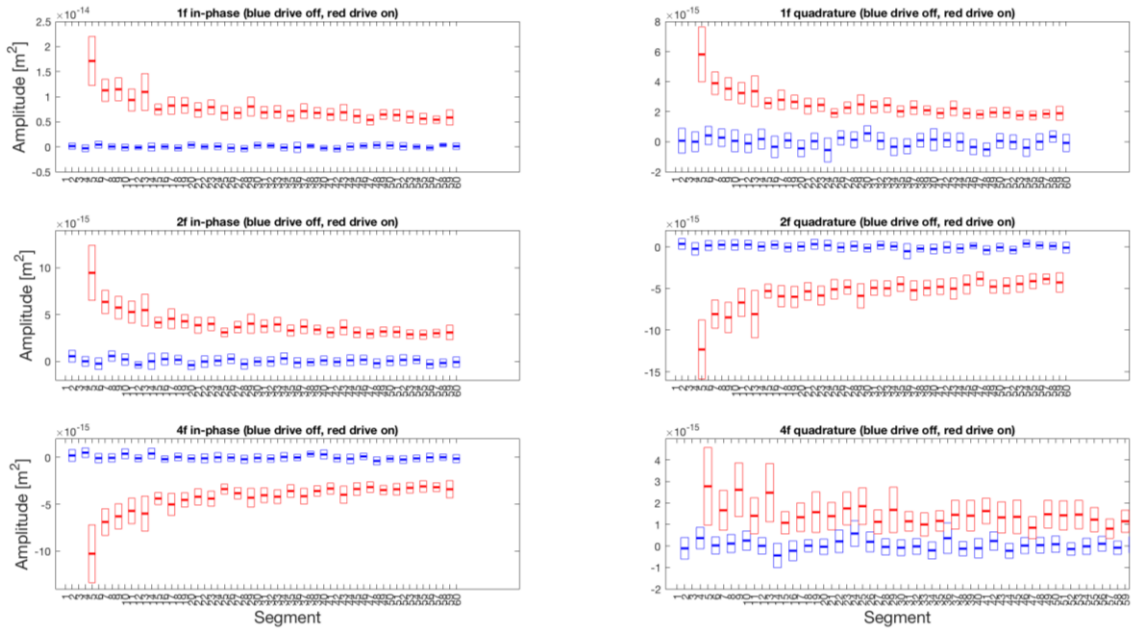

Figure 4.20 Sample demodulated differential strain rate amplitude for 1 rad/s micromechanical simulation vs. sequent driving ON/OFF segments.

A finite demodulated noise shows up in all Fourier terms when the oscillatory driving is ON. The amplitude $A_{K;f}$ is positive for components $K = 1I, 1Q, 2I, 4Q$ and negative for the rest. The demodulation signal reconstructed from the average Fourier amplitudes of the last fifteen ON segments agrees with the crackling noise profile shown in Figure 2.11.

4.6 Experimental Data Analysis

4.6.1 Offline Seismic Noise Subtraction

As is shown in Figure 4.13, the seismic noise is limiting the Michelson sensitivity at low frequencies. An offline seismic noise subtraction analysis based on FFT filtering and subtraction can be implemented following the procedures:

1. For each 1800-s segment of locked Michelson data, compute the averaged transfer function, as well as the coherence between one axis accelerometer signal *e.g.* a_z (see Sec 4.4.2) and the Michelson signal dx_s
2. Compute the full length FFT of both z-accelerometer signal and Michelson signal.
3. Interpolate the averaged transfer function and coherence to the FFT frequency bins.
4. Set all bins with low coherence to zero.
5. Subtract the accelerometer signal FFT times the transfer function from Michelson signal FFT.
6. Convert the subtracted dx_s signal FFT back to time domain with an inverse FFT.

This technique provides a time series of the seismic-noise-subtracted Michelson signal for each driving segment of data.

This offline technique has many advantages: it gives the best possible subtraction during each lock (even if it's non-causal); it provides a time series which can be used for the standard analysis in time domain and for further noise hunting; it can be applied to all measurements with the in-time seismic noise measurements; it can be easily extended to any other channel which turns out to be coherent with the Michelson signal.

4.6.2 Line Removal

The Michelson signal spectrum is polluted by a large amount of lines, which makes it difficult to find a good frequency band for the demodulation analysis. An algorithm is implemented to automatically detect the lines in a given frequency band and remove them in the time domain. The line detection algorithm works as follows:

1. Compute the power spectral density P_s of the signal.

2. Subdivide the desired frequency band (for example 100-2000 Hz) into a small number (256) logarithm spaced bands.

    a. For each band, compute the mean value and the standard deviation of $\log_{10} P_s$ over all the bins in the band.

    b. Remove all the bins with values of $\log_{10} P_s$ which deviate from the mean value more than three times the standard deviation.

    c. Repeat from (a) until all points are within 3 times the standard deviation.

    d. The mean value is a good estimation of the background noise in the band, without the contribution of the lines.

3. Interpolate the estimated background noise to all the original frequency bins.

4. Select all the bins of the original PSD for which the value is more than five times the estimated background: those are the lines to be removed.

5. Collate together all the adjacent bins found in the previous step.

6. Each group will be a single line: estimate the mean frequency, peak value, width, and total power.

Then, for each of the detected lines, a time domain filter is created, implementing a notch with tuned frequency and Q-factors.

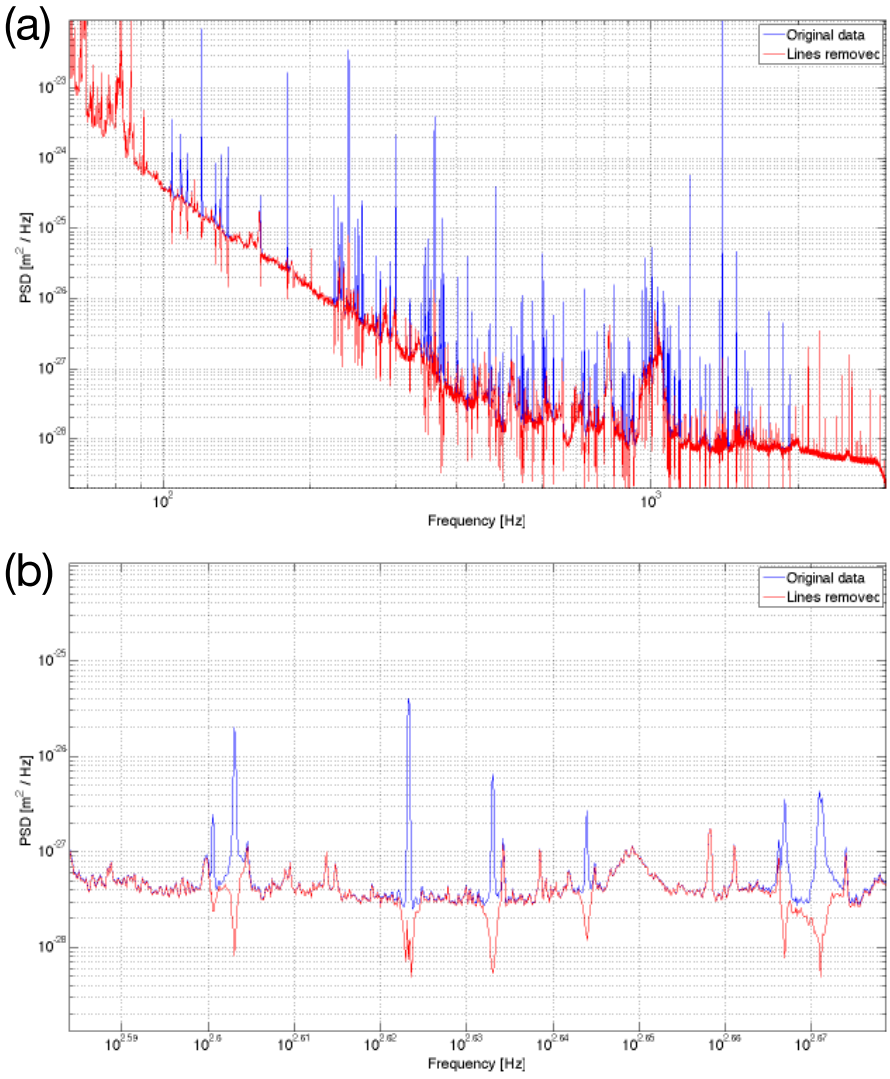

Figure 4.21 Sample Michelson spectrum showing the line removal results.

Figure 4.21 shows an example of the result. Some of the lines are over-notched. However, this is not harmful – if a line is notched more than necessary, the signal power in that frequency is simply discarded.

4.6.3 Segment Quality

Each crackling noise measurement run lasts about two days. The data can be contaminated by excessive environmental noise from time to time. The quality of the segment has to be evaluated on half-hour basis. Criteria are set to omit noisy segments from analysis.

The alignment of the interferometer affects the sensitivity. The beams are overlapped at the PDs and the Michelson arms are balanced before the measurement starts. As time goes, the alignment can drift due to, for example, the deflation of the air legs that can change the float table leveling. The in-line calibration inspects the quality of Michelson alignment by monitoring the in-time variation of optical gain with a single-line noise injection (111 Hz): the optical gain is calibrated using fringe amplitudes when the setup is optimally aligned at the beginning. The change in alignment manifests itself in the change in the excited error signal.

The in-line calibration is equivalent to a single line measurement of the open-loop transfer function (OLTF) $\frac{x_1}{x_2}$ (See Section 4.3.4 for details about the servo loop). As the gain of the OLTF has a known approximate shape of $1/f$, where it crosses the unity gain can be estimated from the gain measured at the injection line. Unity gain frequency (UGF) is therefore monitored all the time. The average and standard deviation of UGF value in each half-hour segment is recorded. When the lock configuration is stable, the UGF has small fluctuations (with a typical standard deviation of ~ 5 Hz) around the optimally designed UGF value (~ 60 Hz). The segments with mean UGF values out of the normal range of 55-65 Hz or exceptionally large standard deviations (> 15 Hz) are discarded.

The low frequency (25-50 Hz) spectral power is integrated and threshold is set to spot segments with excessive low-frequency noise arising in the Michelson setup that are most likely caused by unusually large seismic or acoustic noise during that measurement segment.

4.6.4 Demodulate Crackling Noise

The demodulation techniques described in Section 4.5 are useful for discriminating periodic signals from stationary background. Since crackling noise is expected to be upconverted from the slow-varying external driving, the demodulation amplitudes at harmonics of the driving frequencies are investigated in each of the driving ON/OFF segments. Following the similar demodulation procedure as described in Section 4.5.4 for the simulated crackling noise data, the calibrated Michelson signal in units of meters are band-passed in the relatively quiet frequency bands, squared, and then demodulated.

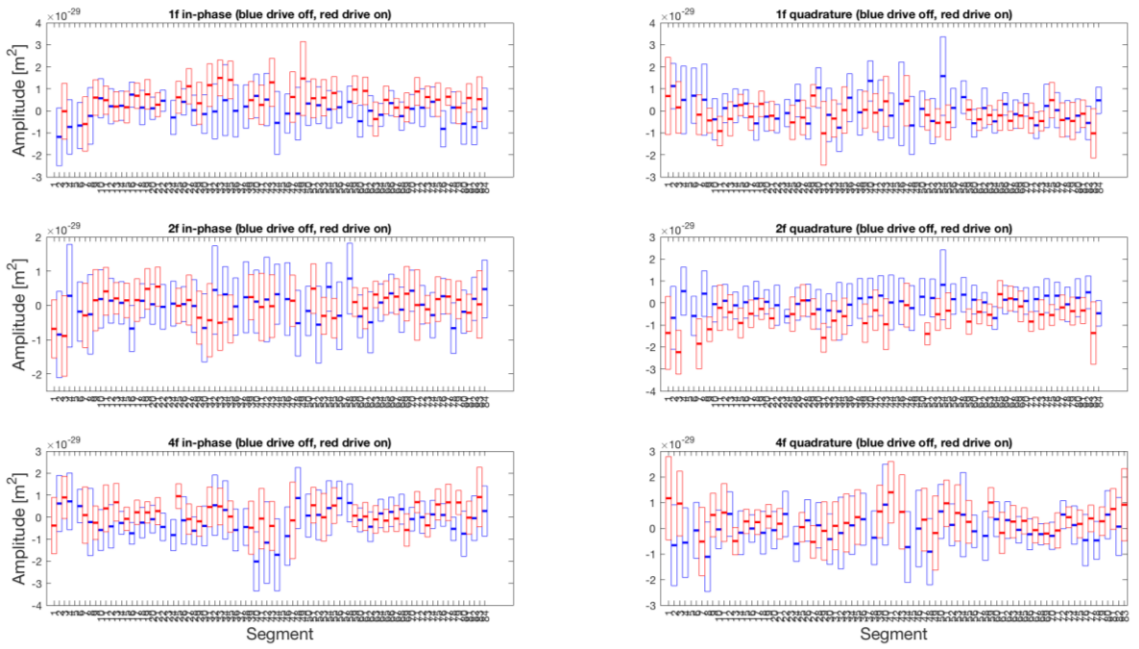

Figure 4.22 Sample demodulated Michelson signal amplitudes in frequency band 30-35 Hz for a 0.19 Hz driving crackling noise experiment in sequent driving ON/OFF segments

Figure 4.22 shows the sample demodulation results $A_{K;\boldsymbol{f}}$ for the Michelson signal in frequency band $\boldsymbol{f} = [30, 35]$ Hz, over numbers of 0.19 Hz driving ON (red) and OFF (blue) segments at multiple frequency components $K = nI/Q$, where $n = 1, 2, 3, 4$. The peak-to-peak driving amplitude is $\sim 30\,\mu m$ according to the OSEM shadow sensor monitoring of the cantilever-tip displacement. The segments with exceedingly large errors are thrown away.

4.6.5 Student-t Test Sample Statistics

A two-sample Student-t test is applied to tell if, by null hypothesis, the average demodulation amplitudes in the driving ON segments and those in the driving OFF segments are independent random samples drawn from the same normal distributions with

equal means. The 95% confidence interval on the difference of the population means, $c_{K;\boldsymbol{f}}$, with lower bound $c_{K;\boldsymbol{f}}^{min}$ and upper bound $c_{K;\boldsymbol{f}}^{max}$, is a statistical evaluation of the demodulation amplitudes upconverted in the ON segments. When $c_{K;\boldsymbol{f}}^{min} \cdot c_{K;\boldsymbol{f}}^{max} > 0$, or when the null hypothesis can be rejected at the 5% significance level, there is a statistically significant difference between demodulation amplitudes in ON segments from those in OFF segments.

Figure 4.23 shows the sample statistical results for the same 0.19 Hz driving experimental data demodulation as the one for Figure 4.22. In the figure, Michelson sensitivity spectrum is plotted in blue for reference. The blue shades around the Michelson mean spectrum shows the maximum and minimum fluctuation of the sensitivity in all measurement segments for the entire test run. The confidence intervals of the demodulated amplitudes are shown as solid boxes in all analyzed frequency bands. Different colors indicate different student-t test results. Red/green boxes represent a positive/negative amplitude detected at the 5% significance levels in that frequency band. The left/right bounds of the boxes indicate the frequency band limits, while the upper/lower bounds of the boxes are confidence intervals. Black lines are the noise amplitude upper bounds for the frequency bands in which Student-t test fails rejecting the null hypothesis, *i.e.* $\emptyset \in [c_{K;\boldsymbol{f}}^{min}, c_{K;\boldsymbol{f}}^{max}]$. The noise upper bound is drawn as the maximum absolute value of the confidence interval.

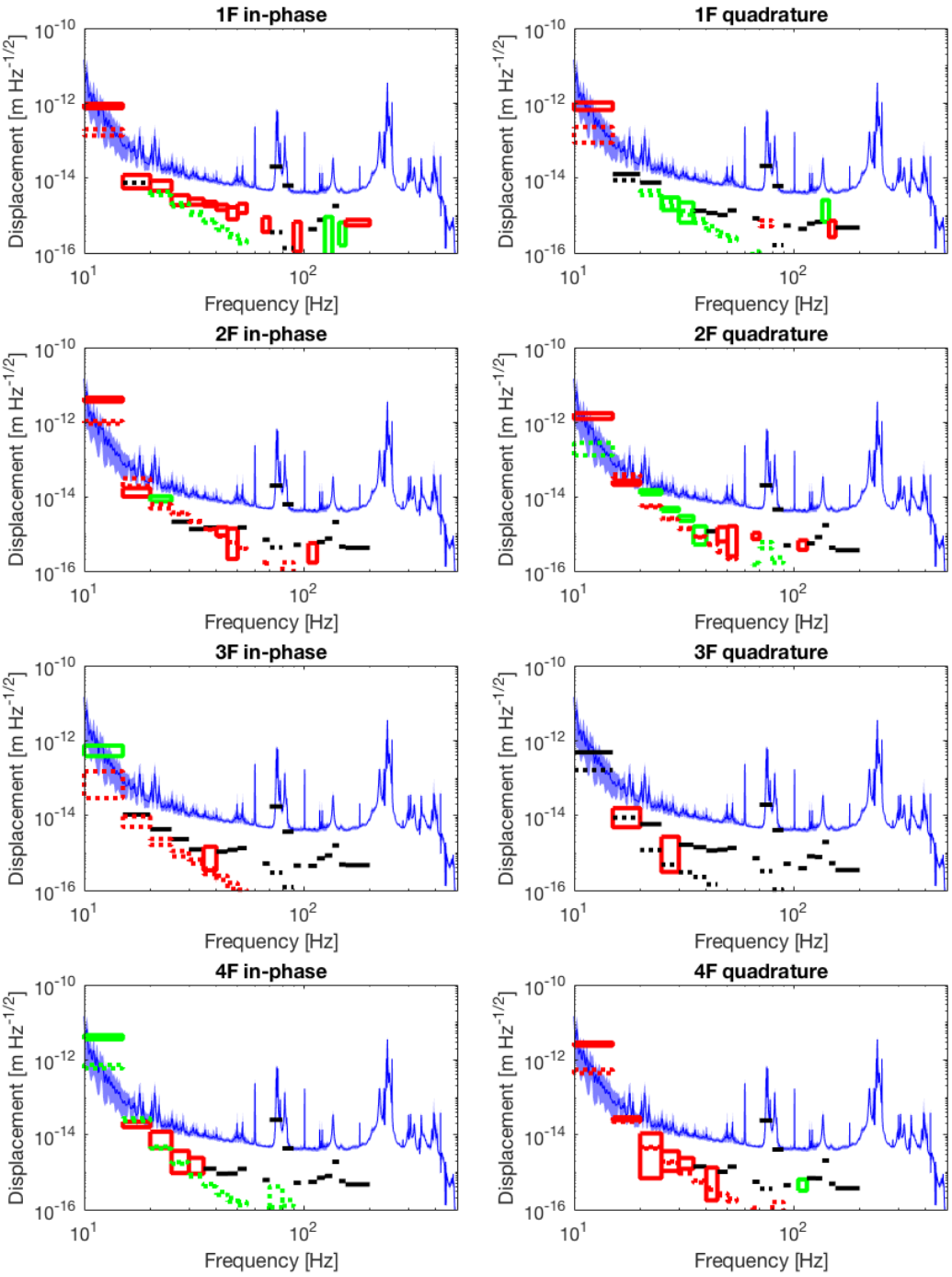

Figure 4.23 Summary spectrum for the 0.19 Hz driving experiment showing the student-t statistical results on demodulation amplitudes from all test segments for Michelson signal in solid boxes, current monitor sum in dashed boxes. Boxes upper/lower bounds indicate the confidence intervals. Red/green/black denotes a positive/negative/failed detection of the demodulated noise amplitudes from Student-t test.

4.6.6 Actuation Noise Subtraction

The demodulation technique incorporating the statistical analysis works to distinguish the noises with amplitude correlated to drive. There could be systematic noises that are also modulated by the common-mode drive. Examples include the actuation noise. The actuation current signals sent to the voice coils to drive or control the cantilever samples are independently measured by the two current monitors (see Section 4.4.9 for details). The electronic source of actuation noise that can couple to the Michelson signal is monitored by the sum of the current monitor outputs, which characterizes the uncorrelated actuation force on the cantilever blades. The same demodulation technique is applied to the current monitor sum to quantify the modulated actuation noise power. The noise can be projected to a differential displacement noise in different frequency bands through the actuation transfer function multiplied by the linear approximate optical gain (see Section 4.3.5 for details).

The actuation noise is analyzed in summary spectrum in the same way as the Michelson demodulation signal. Figure 4.23 projects the statistical demodulation results for the actuation noise in dashed lines for the sample 0.19 Hz test in the Michelson spectrum. Colors indicate positive/negative/no detection following the same convention described in the previous section.

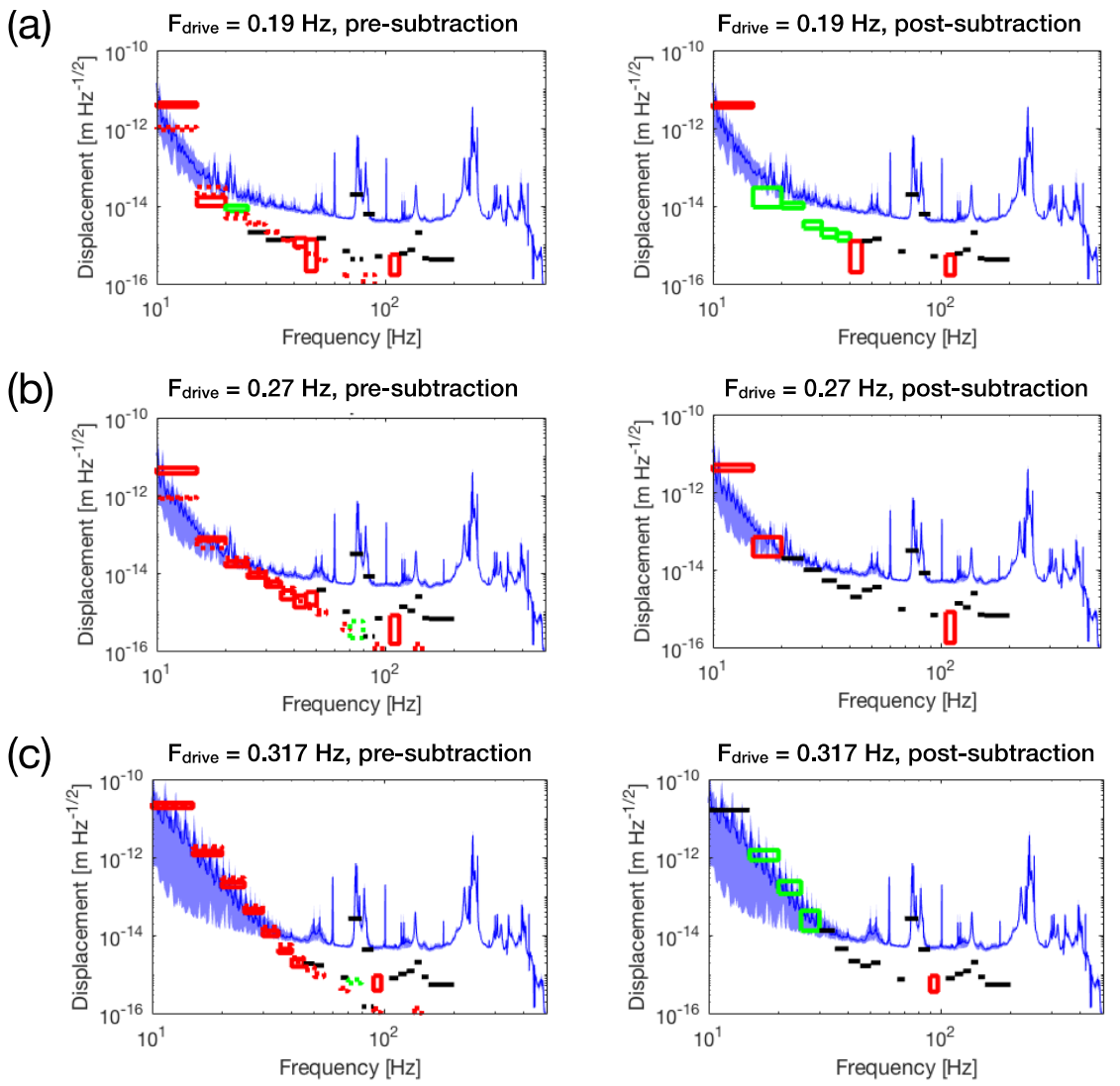

Figure 4.24 Summary spectrum of demodulation results before and after actuation noise subtraction for different frequency driving experiments on maraging steel blades.

The superimposed actuation noise amplitude can be subtracted from the Michelson signal in frequency domain. Figure 4.24 left and right columns compare the sample 2*I* demodulation signal (in solid box) before and after this subtraction.

Figure 4.24 (a), (b) and (c) shows the demodulation results for experiments with different driving frequency at 0.19 Hz, 0.27 Hz and 0.317 Hz, but with the same driving amplitude.

The actuation noise increases with the driving rate. When the actuation noise dominates the differential motion of the cantilever samples, *e.g.* the case with driving frequency of 0.317 Hz, the projected demodulated actuation noise matches reasonably well with the total demodulated Michelson signal as expected.

4.7 Results

4.7.1 Power-law Fitting on Demodulation Amplitudes

The crackling experiment explores test runs with different driving frequencies spanning two orders of magnitude timescale from 0.0317 to 0.317 Hz, but with the same peak-to-peak displacement amplitude of ~ 30 μm. Figure 4.25 shows the sample demodulated actuation-noise-subtracted Michelson signal for the 0.19 Hz driving test.

Throughout all driving frequency measurements, positive $1I$ and negative $2Q$ demodulated noises rise consistently in low frequency range (< 60 Hz). The demodulated noise amplitudes $A_K(f) = A_{K;\boldsymbol{f}}$, where $f = \frac{(f_1+f_2)}{2}$, seems to follow a power law relation with the spectrum frequency f.

For each demodulation components and in the frequency range 15-60 Hz, if demodulated noises with amplitudes of the same sign are detected in more than four 5-Hz interval frequency bands, the average demodulated noise amplitude $A_K(f)$ *vs*. spectrum frequency f can be fitted using a power law model for each demodulation component K:

$$A_K(f) = A_{K,0} f^{-\kappa}, \tag{4.24}$$

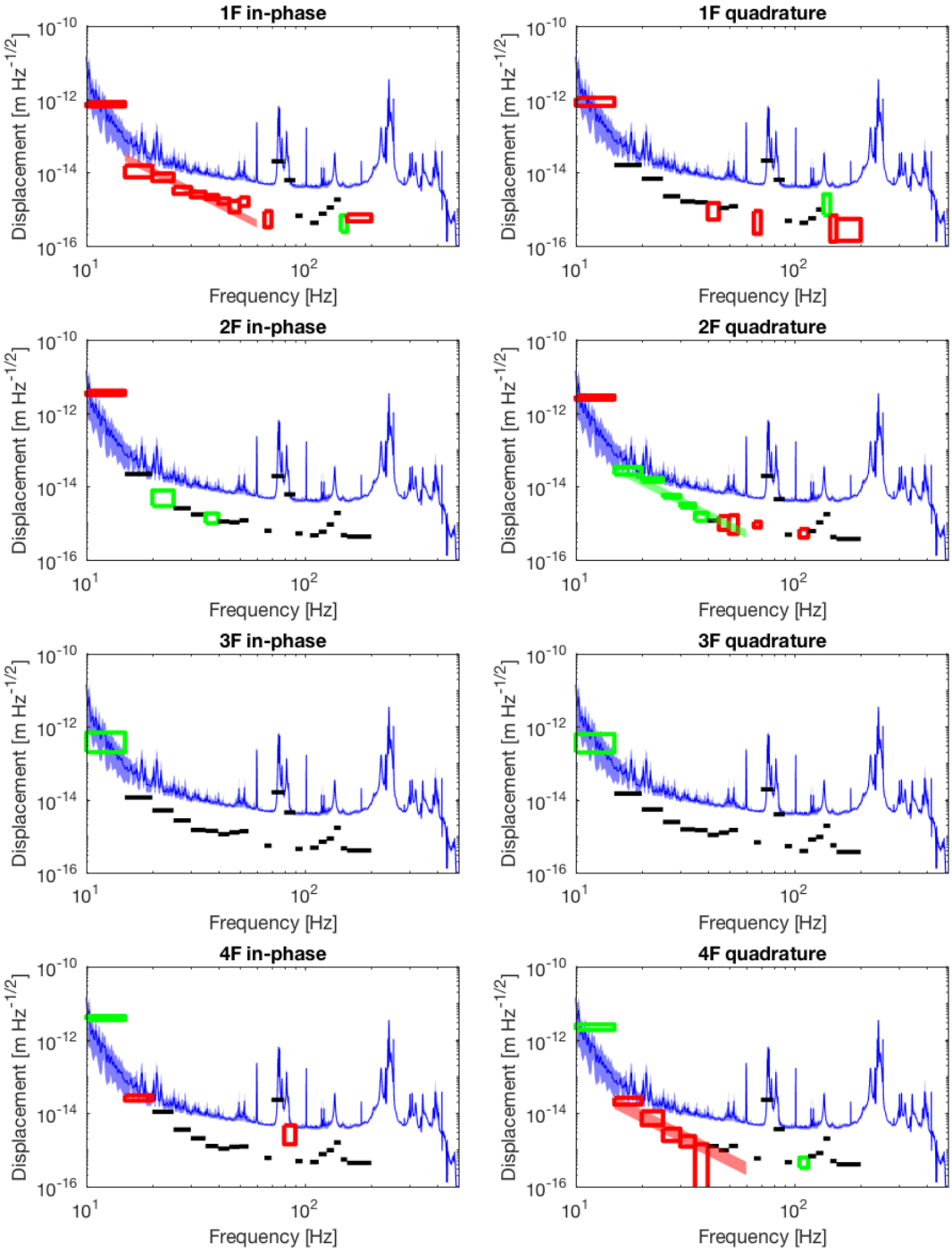

Figure 4.25 Power law fitting of demodulated noise amplitudes in the summary spectrum for sample 0.19 Hz driving experiments on maraging steel blades.

where $A_{K,0}$ is the gain fitted as a measure of the noise level. The power-law exponent is expected to have a value of $\kappa = 3$: the demodulation results from the microplastic simulation give a f^{-1} spectral frequency dependency of differential strain of two independent sample and the cantilever spring structural response gives an additional f^{-2} shape. The parametric estimation on the gain $A_{K,0}$ can be obtained from a weighted non-linear regression on the mean values of demodulation amplitude, $A_K = (c_K^{max} + c_K^{min})/2$. The fit is weighted by $w = 1/\delta A_K^2$, where δA_K is the standard error $\delta A_K = (c_K^{max} - c_K^{min})/2$.

The fitting result A'_K are shaded bands superimposed to the raw demodulation data in Figure 4.25, with the width of the bands indicates the fitting error:

$$A'_{K,max} = (A'_{K,0} + \delta A'_{K,0})\, f^{-3}, \tag{4.25a}$$

$$A'_{K,min} = (A'_{K,0} - \delta A'_{K,0})\, f^{-3}. \tag{4.25b}$$

The noise gain $A'_{K,0}$ obtained from spectrum analysis leaves the demodulation sign information out. The Fourier amplitude can be positive or negative. The final noise gain $A'_{K,\alpha}$ absorbs the sign of the Fourier amplitude mean, α:

$$A'_{K,\alpha} = \alpha A'_{K,0}, \tag{4.26}$$

for a comprehensive characterization of the upconversion noise.

4.7.2 Experimental vs. Simulation Results

The fitted noise gain $A'_{K,\alpha}$ characterizes the demodulated noise at each Fourier component K. Figure 4.26 (a) shows the demodulation noise gain $A'_{K,\alpha}$ obtained from the different

driving frequency but same driving amplitude tests on the maraging steel blades (see previous section, Figure 4.25). In all test runs, no systematic demodulation noises have been detected at components $K = 3I, 3Q, 4I$ for the $A'_{K,0}$ estimation[4]. There is a weak driving frequency dependency: the average value of the absolute noise amplitudes increases with driving frequency for all demodulation components, which means that the demodulated noise level is in general higher when the blades were driven with faster excitations.

Different driving frequency oscillation tests can be done with microplastic simulation on single crystalline copper – simulation parameters are kept the same as prescribed in Section 2.3.3. For each driving frequency, eight independent samples are tested with the same simulation parameters and prescribed stress. The differential strain noise level, measured from a pair of samples, can be estimated as an average of the demodulated strain rate amplitudes over all spectral frequency bands, $A'_{K,0} = < \dot{A}_K(f) >$. Different pairs of independent samples generate demodulation results for the sample statistics for each driving frequency test (Section 4.5.4). Figure 4.26 (b) shows the estimated demodulated noise amplitude $A'_{K,\alpha}$ vs. driving frequency F_{drive} obtained from simulation tests with the same oscillation stress amplitude.

[4] For each Fourier component K, a minimum of four data points of $A_{K;\boldsymbol{f}}$ is required for the power-law fitting estimation for $A'_{K,0}$.

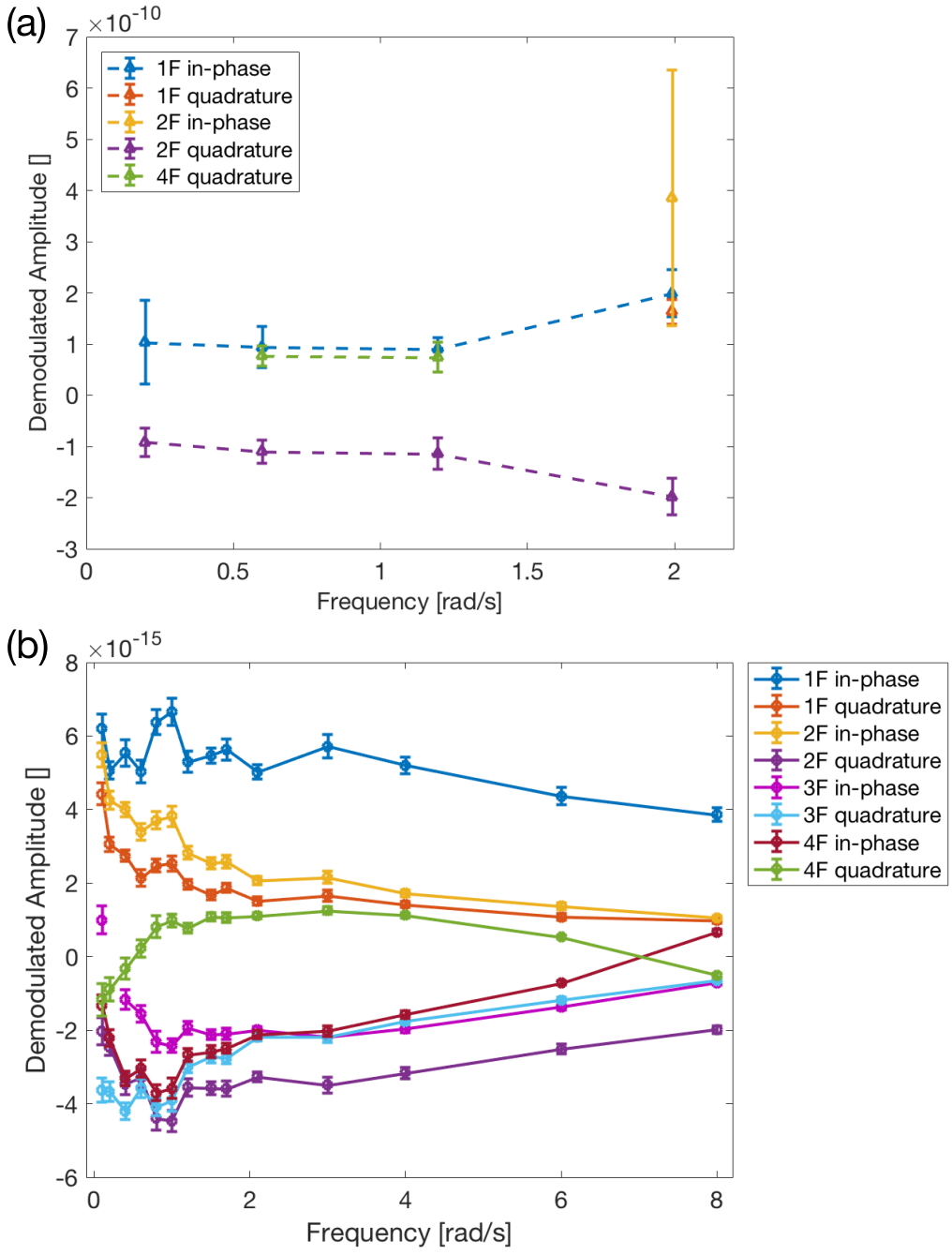

Figure 4.26 Demodulated noise level at different Fourier components vs. driving frequency (a) estimated from the different-driving-frequency but same-driving-amplitude experiments on maraging steel blades, and (b) obtained from different-driving-frequency but same-driving-amplitude micromechanical simulations on single crystalline copper.

Both experimental and simulation results show prominent positive $1I$ and negative $2Q$ noise. However, the experiments and simulations seem to see opposite trends in the frequency dependency of the noise amplitudes. Also, the experiments do not resolved consistent noises in $1Q, 2I, 3I, 3Q, 4I, 4Q$ components as the simulations do.

4.8 Discussion

4.8.1 Demodulated Noise Profile Reconstruction

A demodulation noise profile n_r^2 can be reconstructed using the Fourier series:

$$n_r^2(t) = \sum_K A'_{K,\alpha} F_K(t). \tag{4.27}$$

Figure 4.27 summarizes the representative experimental and simulation demodulation signal reconstruction results for different driving frequency tests. The oscillatory drive amplitude is scaled to unity, while the signal profile is scaled by its standard deviation for visualization purposes.

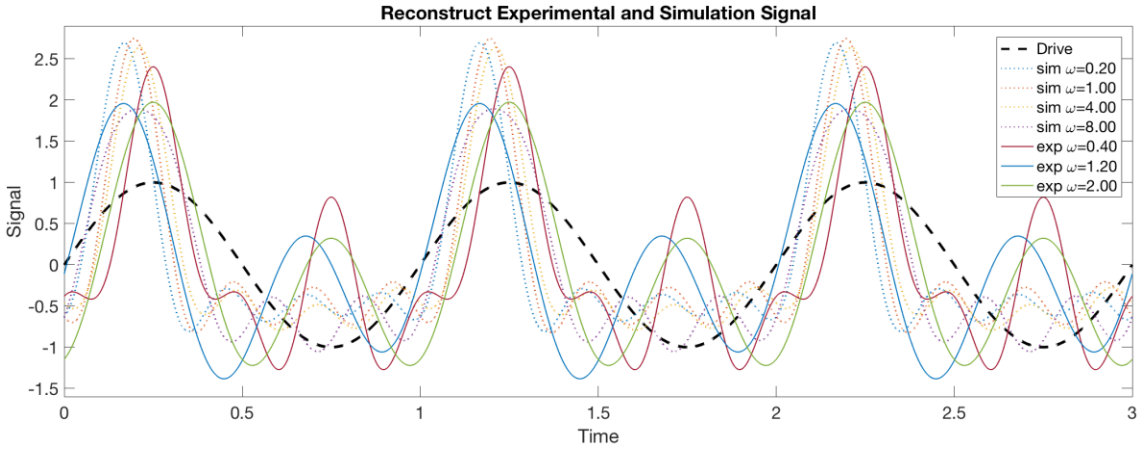

Figure 4.27 The reconstructed experimental and simulation demodulated signals for different driving frequency tests.

Both experimental and simulation reconstructed signals feature a peak noise amplitude around the peak of the drive, where the external drive approaches a global maximum, as the quasi-static load /stress is applied in the positive direction.

However, the current experiments are limited by sensitivity and/or statistics to resolve a more complete Fourier profile of the driving-modulated noise for a more confident comparison with the simulation results. Whether the upconversion noise detected in the experiment is indeed crackling noise due to microplasticity or not still needs further investigation.

4.8.2 Materials Dependency

Preliminary results from crackling noise experiment with high-carbon steel blades (See Section 4.3.6 for more information) shows a similar noise profile dominated by positive $1I$ and negative $2Q$ demodulation. The absolute value of the power-law fitted noise amplitude gain A'_K is plotted in logarithm versus the demodulation components K for both maraging steel and high-carbon steel experiments in Figure 4.28.

The difference between the high-carbon steel and maraging steel setup is the steel materials that the cantilever samples are made from. There is a small engineering difference in the cantilever stiffness. While the load masses load the pre-curved maraging steel blades flat at ~50% of the nominal yielding stress, the high-carbon steel blades are loaded to ~90% of the nominal yielding stress.

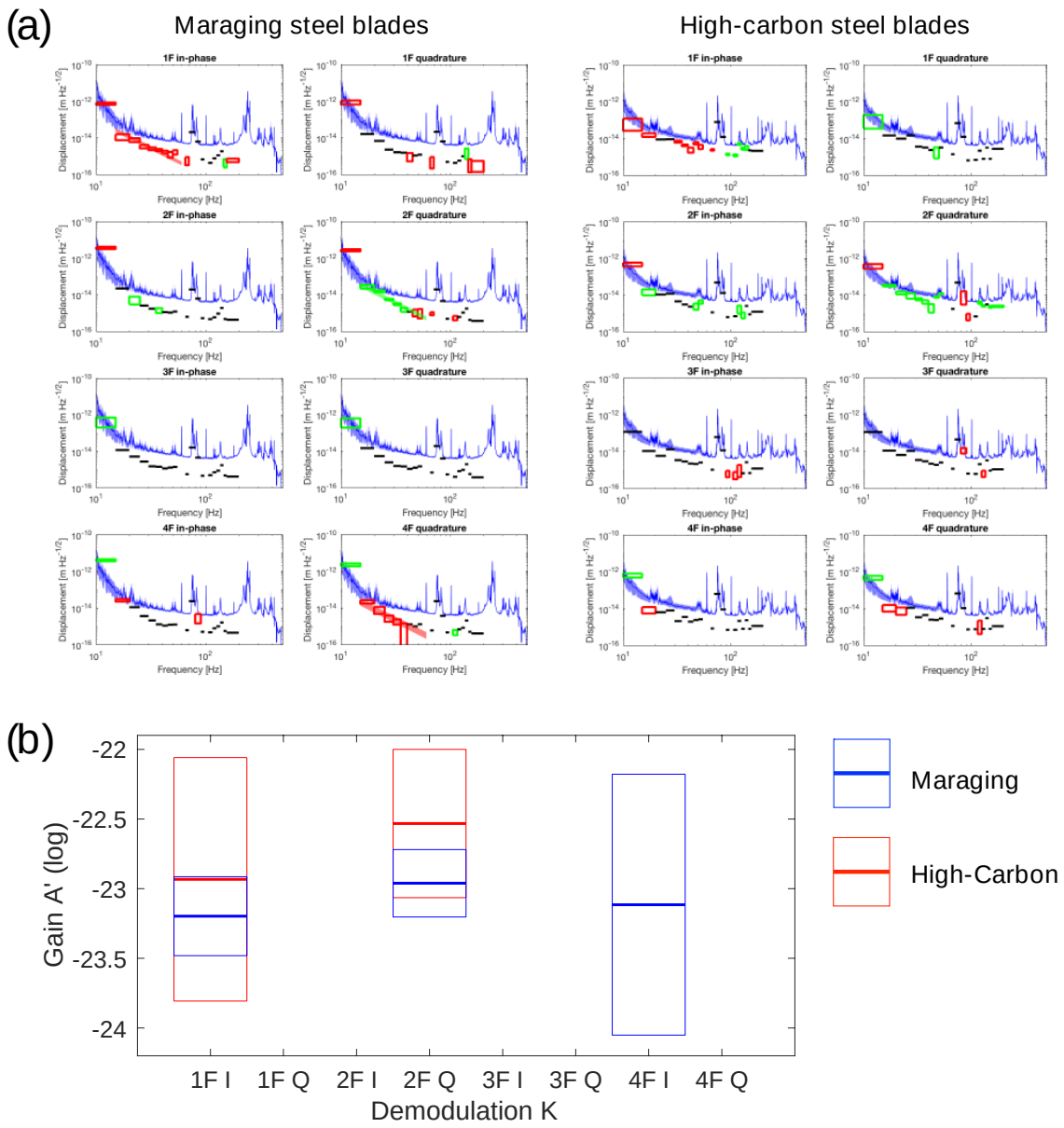

Figure 4.28 Preliminary results from crackling noise experiment with high-carbon steel blades shows a similar feature and level of demodulated noise as maraging steel blades.

A larger amplitude of crackling noise is anticipated in high-carbon steel cantilever samples:

1. Metallic materials exhibiting higher internal friction, acoustic emission, and quasistatic hysteresis are expected to exhibit larger microplastic noise (See Section 4.3.6 for details).
2. Larger microplastic dissipation is expected to occur in samples that are loaded with higher quasistatic stress closer to the yielding point (See Chapter 2 for details)

Up to this point, although the mean values of the noise gain resolved at $1I$ and $2Q$ are higher in the high-carbon steel setup than in the maraging steel one, there is no statistically meaningful way to tell difference between the noise levels of the two materials within error bars. More data as well as more experiments with different driving frequencies are upon request to improve statistical significance.

4.9 Crackling Noise Projection in Advanced LIGO

A mechanical-upconversion noise resolved in the prototype maraging steel blades experiment is expected to rise also in the maraging steel quadruple suspensions (QUAD) and propagate to the test mass. In order to apply the crackling noise experimental results to predict for an upper limit of crackling noise in advanced LIGO (aLIGO), two discrepancies have to be taken into consideration: 1. the maraging steel blades used in aLIGO are almost three times larger than the prototype cantilever samples used in the table-top experiment, and 2. the cantilever blades are integrated to different dynamic system.

A macroscopic model was developed by Vajente[116] to take into account the scaling of crackling noise through blade dimensions and the displacement noise propagation through

blade dynamics, via which the upconverted mechanical noise is projected to a lateral motion of the test mass as an estimation for the level of crackling-induced noise in aLIGO.

4.9.1 Scaling Model

The crackling noise experiment samples and the aLIGO QUAD blades are of the same trapezium geometry, with length L, thickness h, and variable width $b(z) = b_0(1 - \beta z/L)$, where β is a shape factor, b_0 is the major width, and z is the coordinate along the blade length. Similarly, x is the transverse coordinate along the blade width, and y along the blade thickness. The same macroscopic model can be developed and applied to both cantilever blades.

	Large (D060237)	**Small(D080019)**
Length [mm] L	294	91
Maximum width [mm] b_0	49	18
Minimum width [mm] b_1	10	4.2
Geometry β	0.20	0.23
Thickness [mm] h_0	4.2	1.0
Mass [kg] m_B	0.294	0.008
Young's modulus [GPa]	186	
Density [kg/m^3]	8000	

Table 4.1 Summary of the main mechanical and geometrical properties of the large aLIGO and small crackling noise experiment maraging blades.

The sizes of the aLIGO maraging blades and the crackling noise experiment blades are different, as shown in Table 4.1. For a scaling purpose, the crackling noise is assumed to arise locally in microscopic volume of materials and propagate elastically to the cantilever tip. More specifically:

- Each crackling event spans a region of the metallic crystal lattice that is much smaller than the volume of the blade.
- Beside from crackling events, the blade behaves like an ideal elastic body.
- The rate and amplitude of crackling events depend locally only on the stress and stress rate.

Assuming that events are uncorrelated, noise due to a large number of events can be computed through an integration of a Poisson distribution over the entire blade, with amplitude and rate depending on the position, the power spectral density of the vertical test mass motion $S_{TM}(\omega)$ can be written as an incoherent sum of all crackling events,

$$S_{TM}(\omega) = |\tilde{\chi}(\omega)|^2 \int_0^L dz \int_{-\frac{h}{2}}^{\frac{h}{2}} dy \int_{-\frac{b(z)}{2}}^{\frac{b(z)}{2}} dx \; 2r(z,x,y) < f_0(z,x,y)^2 > \left|\tilde{R}(\omega,z,x,y)\right|^2, \quad (4.28)$$

where $r(x,y,z)$ is the local crackling event rate, and $\tilde{R}(\omega,x,y,z)$ is the response of the blade and suspended elements to a single, localized force with an amplitude $f_0(x,y,z)$ and a time evolution in Fourier space $\tilde{\chi}(\omega)$.

The microscopic physics of crackling noise is described by the event rate and amplitude $2r(x,y,z) < f_0(z,x,y)^2 >$. A general power expansion model $C(z,x,y) = 2r(x,y,z) < f_0(z,x,y)^2 >$ is used to encode the crackling noise behavior,

$$C(z,x,y) = C_0 + C_1\sigma + C_2\sigma^2 + C_3\dot{\sigma} + C_4\dot{\sigma}^2 + C_5\sigma\sigma^2. \quad (4.29)$$

4.9.2 Elastic Model

With the assumption that, apart from the crackling noise, the blade can be described as a perfect elastic body. An elastic model of the blade and the suspension is built to compute the equilibrium shape of a pre-curved blade and the corresponding static stress, the response of the blade to low-frequency perturbations (seismic noise in the QUAD, driving force in crackling noise experiment), and the test mass motion due to a single crackling event.

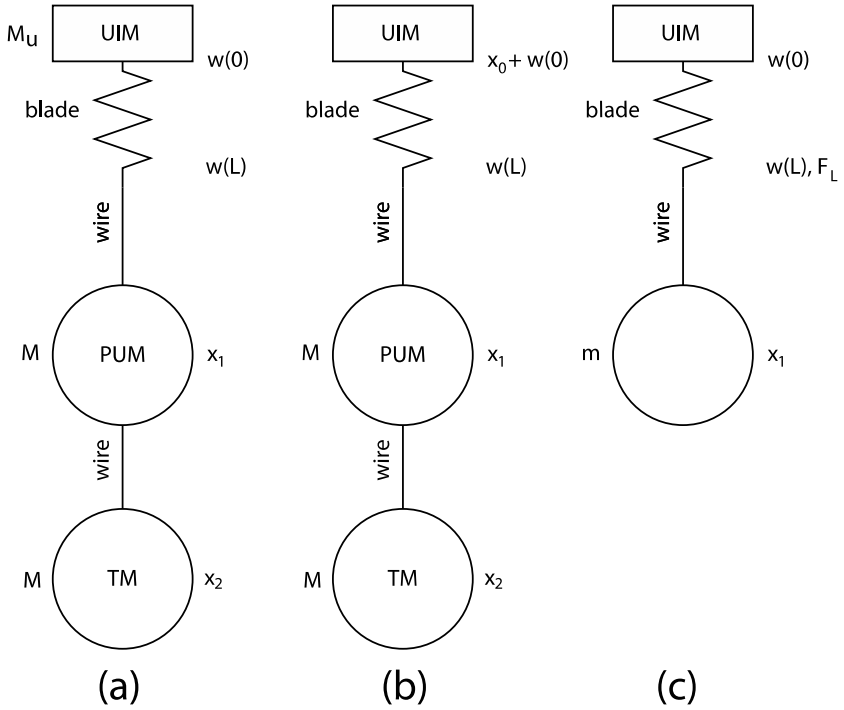

Figure 4.29 Simplified models of the quadruple suspension system for cases that (a) the UIM stage is free to move, (b) the displacement of the UIM stage is prescribed, and (c) the force on the blade tip is prescribed.

For these purposes, in addition to the case where the static equilibrium condition due to the load and initial pre-curvature can be computed with the UIM fixed to ground, three

dynamic cases, as illustrated in Figure 4.29, are considered for the cantilever suspension system modeling:

(a) The response of crackling noise events of interest is above 10 Hz, *i.e.* higher than all resonant frequencies of the QUAD stages above the UIM, hence the UIM can be modeled as a free mass.

(b) To compute the response to seismic noise in the QUAD, the upper stages of the QUAD can be neglected and a motion of the UIM can be prescribed.

(c) in the case of the crackling noise experiment, the blade is clamped to a mass that is much larger than the load, so the upper stage can be approximated as fixed and a prescribed force is acting on the blade tip.

Same equation of motion for the blade tip motion applies to all cases,

$$EI(0)\left(1-\beta\frac{z}{L}\right)w'' - EI(0)\frac{2\beta}{L}w''' + \rho A\ddot{w} = Af - \rho A\ddot{x}_0, \qquad (4.30)$$

where $w(z)$ is the blade neutral surface position as a deviation from the equilibrium. w' denotes derivatives with respect to z and $\dot{w}$ denotes derivative with respect to time. In the equation, E is the young's modulus, ρ is the density, A is the cross-section area, I_0 is the transverse momentum, and f is the force due to single crackling event.

Different boundary conditions for this equation encode the dynamics of the suspended stages. The equations are solved numerically through eigenmode expansion to get the blade tip response to seismic motion and a single crackling event. The eigenfrequencies and modes depend on the suspended elements.

4.9.3 Noise Projection

The numerical results solved from eigenmode expansion for the equation of motion allows an expression of the propagated crackling noise spectrum as a function of integrals of the eigenmodes, factoring out most of the blade dimensions. In frequency space, the prototype experiment suspended block (load mass) response S_{block} and aLIGO test-mass response S_{TM} can be written in terms of the coefficients $\hat{I}$'s that are integrals of the specific functions of the modes.

$$S_{block}(\omega) = \frac{|\tilde{\chi}(\omega)T_1(\omega)|^2}{6\omega^4}\frac{\omega_0^2(L)h^3b_0E^2}{\rho^2A_0^2}\left[\frac{\hat{I}_0}{R_0^2L}C_2 + \frac{\hat{I}_1}{R_0L^3}\left(-2C_2F_0 - C_5\dot{F}_0\right)\right.$$
$$\left. + \frac{\hat{I}_2}{L^5}\left(C_2F_0^2 + C_4\dot{F}_0^2 + C_5F_0\dot{F}_0\right)\right], \qquad (4.31a)$$

$$S_{TM}(\omega) = \frac{|\tilde{\chi}(\omega)T_2(\omega)|^2}{6\omega^4}\frac{\omega_0^2(L)h^3b_0E^2}{\rho^2A_0^2}\left[\frac{\hat{I}_0}{R_0^2L}C_2 + \frac{\hat{I}_1\hat{\Gamma}}{R_0L^3\omega_0^2}(2C_2\ddot{x}_0 + C_5\dddot{x}_0)\right.$$
$$\left. + \frac{\hat{I}_2\hat{\Gamma}^2}{L^5\omega_0^4}(C_2\ddot{x}_0^2 + C_4\dddot{x}_0^2 + C_5\ddot{x}_0\dddot{x}_0)\right]. \qquad (4.31b)$$

In the expression for the prototype experiment (Equation 4.31a), F_0 is the controlled driving force and T_1 is the transfer function from blade tip motion to vertical motion of the suspended block. Using this expression, the demodulation measurements A_K from the crackling noise experiment can be used to estimate for the C coefficients,

$$\begin{pmatrix} A_{1I}(\omega) \\ A_{1Q}(\omega) \\ A_{2I}(\omega) \\ A_{2Q}(\omega) \end{pmatrix}$$

$$= \frac{|\tilde{\chi}(\omega)T_1(\omega)|^2}{6\omega^4}\frac{\omega_0^2(L)h^3b_0E^2}{\rho^2A_0^2}\begin{pmatrix} -2\dfrac{\hat{I}_1}{R_0L^3}F_0 & 0 & 0 \\ 0 & 0 & -\dfrac{\hat{I}_1}{R_0L^3}\Omega F_0 \\ 0 & 0 & \dfrac{\hat{I}_2}{L^5}\dfrac{F_0^2\Omega}{2} \\ -\dfrac{\hat{I}_2}{L^5}\dfrac{F_0^2}{2} & \dfrac{\hat{I}_2}{L^5}\dfrac{F_0^2\Omega^2}{2} & 0 \end{pmatrix}\begin{pmatrix} C_2(\omega) \\ C_4(\omega) \\ C_5(\omega) \end{pmatrix}. \quad (4.32)$$

The system is over constrained and thus non-invertible; however it can be solved through pseudo-inverse and by choosing the best estimates of the coefficients at each frequency in a least square sense.

In the expression for the test mass (Equation 4.31b), x_0 is the seismic residual motion of the UIM stage, and T_2 is the transfer function from the blade tip motion to vertical motion of the test mass. The noise behavior of the test mass can be estimated with a knowledge of the C coefficients acquired from the prototype measurements.

4.9.4 Projection Results

Figure 4.30 shows a projection of the crackling noise experiment demodulation measurements to displacement noise on test mass, following the assumptions that crackling noise indeed scales as derived from the macroscopic model described in previous subsections, and that the coupling from test mass vertical motion to test mass

horizontal motion is of the order of 10^{-3}. Seismic motion data from Hanford is used to estimate the motion of the UIM, x_0.

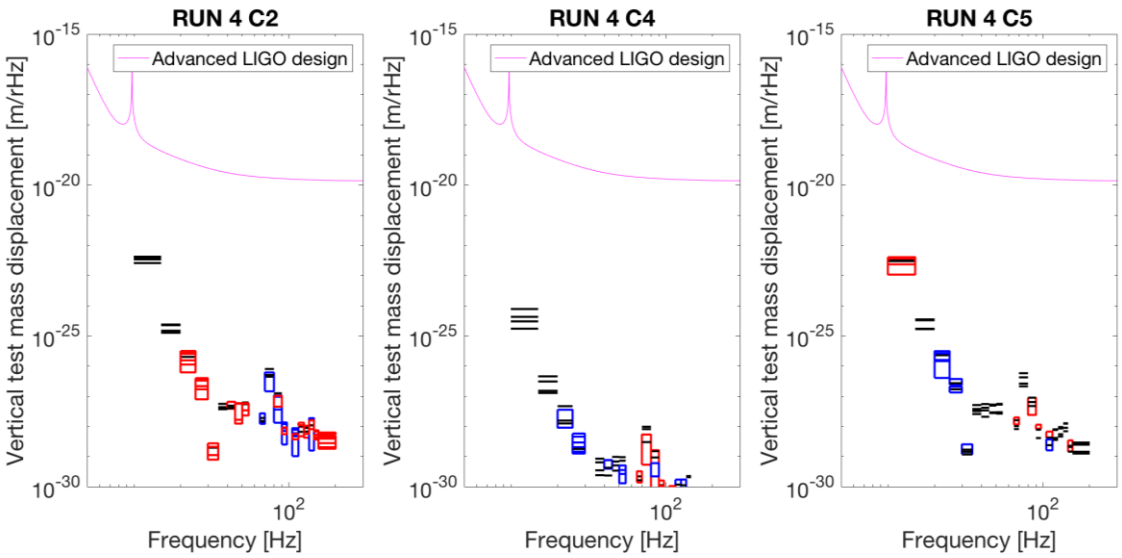

Figure 4.30 Projection of the crackling noise experiment demodulation measurements to displacement noise on test mass through different coupling coefficients.

The final result is summarized in Figure 4.31. The three curves are manually drawn bands through the projections; each corresponds to a possible dependency of crackling noise on the local stress and stress rate. The predicted crackling noise upper limit in aLIGO is significantly lower than $1/10$ of the aLIGO design curve. The projection results conclude that the mechanical upconverted noise arising in the last stage of the maraging steel blades of the QUAD suspension is not limiting the aLIGO sensitivity.

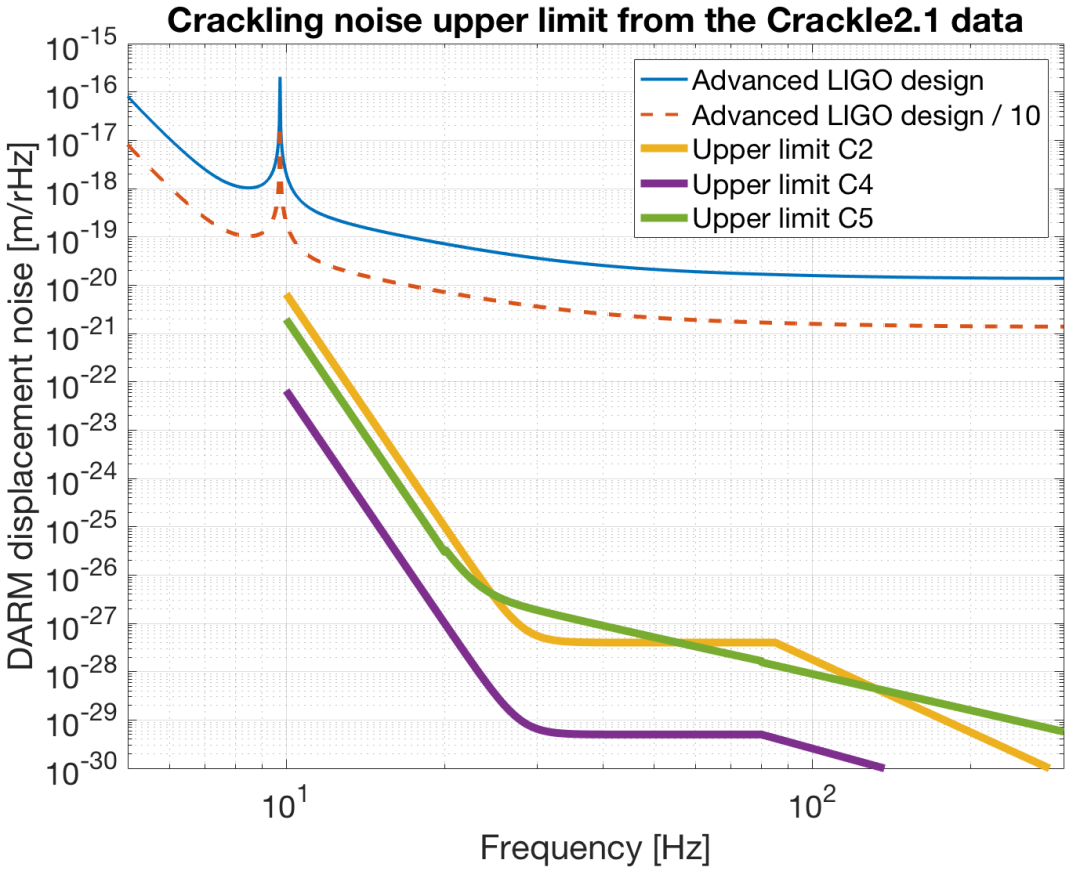

Figure 4.31 The projected crackling noise to the test mass in comparison to aLIGO design curve.

4.10 Summary

The crackling noise experiment is a prototype experiment built to study microplasticity in macroscopic scale. The setup is based on Michelson interferometer and is designed to resolve transient differential motion of two identical cantilever blade tips under prescribed load excitation. Ideally, the differential signal gained by the optical layout would come from the uncorrelated microplastic events occurred in the independent blade samples.

A high displacement resolution of the setup is achieved not only by a careful isolation of the environmental noise but also a systematic design in sensing and control. A variety of

sources noises that can couple to the differential signal through Michelson asymmetries have been discussed and investigated. Noise budgets are generated accordingly for maraging steel and high-carbon steel blades configurations. Both configurations have a differential displacement sensitivity on an order of $10^{-14} m/\sqrt{Hz}$ in the frequency range from 20 to 1000Hz.

According to the microscopic simulation prediction, crackling noise can be mechanically upconverted by the external stress oscillations. The excited noise power is correlated to the external drive. In the macroscopic experiment, a common-mode sinusoidal force is applied to the two blades in sequent drive ON and OFF segments. Similar loading condition can be prescribed to two independent samples in micromechanical simulations. The simulation results resolve a broadband high-frequency component of the differential strain changing with the oscillatory stress.

A signal demodulation analysis (based on Fourier series expansion) is developed to quantify the amplitude of band-limited noise being modulated by the driving force. The demodulated amplitudes measured from ON and OFF segments are compared statistically using Student-t test; the noise level is detected as a difference in statistical mean with a 95% confidence interval. The analysis on experimental data resolves an up-conversion noise, of which the dominant modulated noise behavior shares similarity with that predicted by the micromechanical simulation.

Chapter 5: Conclusions and Outlook

Microplasticity is one of the missing pieces in the study of deformation of metallic materials that encodes profound information about microstructural evolution of the dislocation network that governs the bulk plasticity behavior. The main reason why this important piece has been left out is due to experimental limitations: the conventional bulk mechanical experiments cannot resolve microplastic activities. This thesis focuses on studying microplasticity in both microscopic and macroscopic scale using advanced experimental techniques.

Chapter 2-3 explores microplasticity in micron- and submicron-scale FCC metals. Using nano-DMA and cyclic training experiments on single crystalline copper pillars, and incorporating a minimum model based mesoscopic plasticity simulations, the work shows that microplasticity is present in metallic materials, both pre-yield and post-yield. The mechanism is attributed to a competition between fast avalanches and slow relaxation of dislocations. The work also concludes that the evolution of microplastic dissipation is associated to the smooth elastic-to-plastic transition in the pre-yield regime, as well as a reversible-to-irreversible transition in the post-yield regime. The studies suggest that the quantification of microplasticity can be used to predict global yielding or catastrophic failure of metallic materials.

Chapter 4 presents a macroscopic experiment based on Michelson Interferometry, in which a driving modulated noise has been detected. The resolved noise finds similar characteristics with the microscopic simulation prediction, which indicates a potential mapping from the building block understanding of metallic materials deformation to the

complex engineering-scale observation. The results can give important guidance to scientific instrumental design, such as the noise study for advanced LIGO.

This thesis work has paved a way to probe microplasticity across the scale and explored the connections between the microplastic activities with the metallic materials' susceptibility to plasticity and irreversibility, which points new routes of investigating fatigue or incipient fracture of structural materials via microplasticity or crackling noise. For example, the nano-DMA experiment can be incorporated to fatigue crack tests. Investigating the dissipation behavior of a pre-notched small-scale metallic sample undergoing fatigue cycles would hint on how microstructures change before the large crack initiates. As the work demonstrates that microplasticity in metals encodes fruitful information about deformation history – it opens opportunities for distinguishing 'as-received' metals from 'elastically' loaded ones via mechanical perturbations. The microscopic experimental/simulation results can be directly compared with large-scale crackling noise experimental results. The study can possibly lead to novel non-destructive testing (NDT) methods

The crackling noise experiment has left the future work a large parameter space to explore. For example, the dependency of the crackling noise amplitude on the quasistatic load is worth of further investigation. Another interesting thing to inspect is the materials dependency. The present work compares only maraging steel with high-carbon steel. The study methodology can be applied to extensive lists of metallic materials and even beyond metals.

In the present work, the nature of interferometry study limits the multi-scale investigation of microplastic deformation in the context of uncorrelated mechanical behavior. However, the current work does not exclude the possible existence of coherent microplastic behavior of independent samples that are subjected to the same loading or driving conditions. For future work, the microscopic simulation and experimental methodology presented in this thesis can be adapted to explore the 'common mode' of microplastic deformation.

Last but not the least, the study on microplasticity in metals can offer important experimental-model insights for other systems exhibiting crackling noise, especially for those large rare events are of primary research interest, *e.g.* earthquakes. Recent work has shown that the low-amplitude tidal stresses can have significant correlation with small-quake events, which indicates increased fault susceptibility to large earthquake generation[117]. The intrinsic similarity between dislocation and fault dynamics *etc.* can possibly inspire new ways to improve catastrophic failure event forecasting.

Bibliography

1. Hull, D. & Bacon, D. J. *Introduction to Dislocations*. *Introduction to Dislocations* (2011). doi:10.1016/C2009-0-64358-0
2. Polanyi, M. Über eine Art Gitterstörung, die einen Kristall plastisch machen könnte. *Zeitschrift für Phys.* **89,** 660–664 (1934).
3. Taylor, G. I. The Mechanism of Plastic Deformation of Crystals. Part I. Theoretical. *Proc. R. Soc. A Math. Phys. Eng. Sci.* (1934). doi:10.1098/rspa.1934.0106
4. Orowan, E. Zur Kristallplastizitt. III. *Zeitschrift Für Phys* (1934). doi:10.1007/BF01341480
5. Meakin, J. D. Microstrain Behavior of Body-Centered Cubic Metals. *Can. J. Phys.* (1967). doi:10.1139/p67-082
6. Young, F. W. Elastic-plastic transition in copper crystals as determined by an etch-pit technique. *J. Appl. Phys.* (1961). doi:10.1063/1.1728241
7. Tinder, R. F. & Washburn, J. The initiation of plastic flow in copper. *Acta Metall.* (1964). doi:10.1016/0001-6160(64)90180-4
8. Minari, P., Pichaud, B. & Capella, L. X-ray topographic observation of dislocation multiplication by cross-slip in Cu crystals. *Philos. Mag.* (1975). doi:10.1080/14786437508228931
9. Brandstetter, S. *et al.* From micro- to macroplasticity. *Adv. Mater.* **18,** 1545–1548 (2006).
10. Maaß, R. & Derlet, P. M. Micro-plasticity and recent insights from intermittent and small-scale plasticity. *Acta Materialia* (2018). doi:10.1016/j.actamat.2017.06.023
11. Chalmers, B. Micro-Plasticity in Crystals of Tin. *Proc. R. Soc. London A Math. Phys. Eng. Sci.* **156,** 427–443 (1936).
12. Suresh, S. *Fatigue of Materials*. (Cambridge University Press, 1998).
13. Blanter, M. S., Golovin, I. S., Neuhäuser, H. & Sinning, H. R. *Internal Friction in Metallic Materials: A Handbook*. (Springer Berlin Heidelberg, 2007).
14. Dieter, G. E., Bacon, D., Copley, S. M., Wert, C. a & Wilkes, G. L. *Mechanical Metallurgy*. *Corrosion Engineering* (1988).
15. Radhakrishnan, V. M. Stress ratchetting under tension and cyclic torsion. *Nucl. Eng.*

Des. **34,** 379–387 (1975).

16. Mcdowell, D. L. Stress State Dependence of Cyclic Ratchtting Behavior of Two Rail Steels. *Int. J. Plast.* **11,** 397–421 (1995).
17. Liu, D. *et al.* Anomalous plasticity in the cyclic torsion of micron scale metallic wires. *Phys. Rev. Lett.* **110,** 1–5 (2013).
18. Xiang, Y. & Vlassak, J. J. Bauschinger and size effects in thin-film plasticity. *Acta Mater.* **54,** 5449–5460 (2006).
19. Jennings, A. T. *et al.* Higher compressive strengths and the Bauschinger effect in conformally passivated copper nanopillars. *Acta Mater.* **60,** 3444–3455 (2012).
20. Lee, S. W., Jennings, A. T. & Greer, J. R. Emergence of enhanced strengths and Bauschinger effect in conformally passivated copper nanopillars as revealed by dislocation dynamics. *Acta Mater.* **61,** 1872–1885 (2013).
21. Rajagopalan, J., Han, J. H. & Saif, M. T. A. Plastic Deformation Recovery in Freestanding Nanocrystalline Aluminum and Gold Thin Films. *Science (80-.).* **315,** 1831 LP-1834 (2007).
22. Li, X., Wei, Y., Yang, W. & Gao, H. Competing grain-boundary- and dislocation-mediated mechanisms in plastic strain recovery in nanocrystalline aluminum. *Proc. Natl. Acad. Sci. U. S. A.* **106,** 16108–16113 (2009).
23. Bernal, R. A. *et al.* Intrinsic bauschinger effect and recoverable plasticity in pentatwinned silver nanowires tested in tension. *Nano Lett.* **15,** 139–146 (2015).
24. Wang, Z.-J. *et al.* Cyclic deformation leads to defect healing and strengthening of small-volume metal crystals. *Proc. Natl. Acad. Sci. U. S. A.* **112,** 13502–7 (2015).
25. Sethna, J. P. *et al.* Deformation of Crystals: Connections with Statistical Physics. *Annu. Rev. Mater. Res* **47,** 217–46 (2017).
26. Asaro, R. & Lubarda, V. *Mechanics of Solids and Materials*. (Cambridge University Press, 2006). doi:10.1017/CBO9780511755514
27. Barrett, C. R., Nix, W. D. & Tetelman, A. S. *The principles of engineering materials*. ([Englewood Cliffs, N.J.] : [Prentice-Hall], 1973).
28. Miguel, M. C., Vespignani, A., Zapperi, S., Weiss, J. & Grasso, J. R. Intermittent dislocation flow in viscoplastic deformation. *Nature* **410,** 667–71 (2001).
29. Uchic, M. D. Sample Dimensions Influence Strength and Crystal Plasticity. *Science*

(80-.). **305,** 986–989 (2004).

30. Greer, J. R., Oliver, W. C. & Nix, W. D. Size dependence of mechanical properties of gold at the micron scale in the absence of strain gradients. *Acta Mater.* **53,** 1821–1830 (2005).
31. Dimiduk, D. M. Scale-Free Intermittent Flow in Crystal Plasticity. *Science (80-.).* **312,** 1188–1190 (2006).
32. Uchic, M. D., Shade, P. A. & Dimiduk, D. M. Plasticity of Micrometer-Scale Single Crystals in Compression. *Annu. Rev. Mater. Res.* **39,** 361–386 (2009).
33. Kraft, O., Gruber, P. A., Mönig, R. & Weygand, D. Plasticity in Confined Dimensions. *Annu. Rev. Mater. Res.* **40,** 293–317 (2010).
34. Greer, J. R. & De Hosson, J. T. M. Plasticity in small-sized metallic systems: Intrinsic versus extrinsic size effect. *Prog. Mater. Sci.* **56,** 654–724 (2011).
35. Greer, J. R. & Nix, W. D. Nanoscale gold pillars strengthened through dislocation starvation. *Phys. Rev. B - Condens. Matter Mater. Phys.* **73,** 245410 (2006).
36. Shan, Z. W., Mishra, R. K., Syed Asif, S. A., Warren, O. L. & Minor, A. M. Mechanical annealing and source-limited deformation in submicrometre-diameter Ni crystals. *Nat. Mater.* **7,** 115–119 (2008).
37. Rao, S. I. *et al.* Estimating the strength of single-ended dislocation sources in micron-sized single crystals. *Philos. Mag.* **87,** 4777–4794 (2007).
38. Parthasarathy, T. A., Rao, S. I., Dimiduk, D. M., Uchic, M. D. & Trinkle, D. R. Contribution to size effect of yield strength from the stochastics of dislocation source lengths in finite samples. *Scr. Mater.* **56,** 313–316 (2007).
39. Csikor, F. F., Motz, C., Weygand, D., Zaiser, M. & Zapperi, S. Dislocation Avalanches, Strain Bursts, and the Problem of Plastic Forming at the Micrometer Scale. *Science (80-.).* **318,** 251–254 (2007).
40. Brinckmann, S., Kim, J. Y. & Greer, J. R. Fundamental differences in mechanical behavior between two types of crystals at the nanoscale. *Phys. Rev. Lett.* **100,** 155502 (2008).
41. Minor, A. M. *et al.* A new view of the onset of plasticity during the nanoindentation of aluminium. *Nat. Mater.* **5,** 697–702 (2006).
42. Jennings, A. T., Burek, M. J. & Greer, J. R. Microstructure versus Size: Mechanical

properties of electroplated single crystalline Cu nanopillars. *Phys. Rev. Lett.* **104,** 1–4 (2010).

43. Jennings, A. T., Li, J. & Greer, J. R. Emergence of strain-rate sensitivity in Cu nanopillars: Transition from dislocation multiplication to dislocation nucleation. *Acta Mater.* **59,** 5627–5637 (2011).
44. Kim, J.-Y. & Greer, J. R. Tensile and compressive behavior of gold and molybdenum single crystals at the nano-scale. *Acta Mater.* **57,** 5245–5253 (2009).
45. Kim, J.-Y., Jang, D. & Greer, J. R. Tensile and compressive behavior of tungsten, molybdenum, tantalum and niobium at the nanoscale. *Acta Mater.* **58,** 2355–2363 (2010).
46. Kiener, D., Motz, C., Rester, M., Jenko, M. & Dehm, G. FIB damage of Cu and possible consequences for miniaturized mechanical tests. *Mater. Sci. Eng. A* **459,** 262–272 (2007).
47. Friedman, N. *et al.* Statistics of dislocation slip avalanches in nanosized single crystals show tuned critical behavior predicted by a simple mean field model. *Phys. Rev. Lett.* **109,** 095507 (2012).
48. Maaß, R., Derlet, P. M. & Greer, J. R. Small-scale plasticity: Insights into dislocation avalanche velocities. *Scr. Mater.* **69,** 586–589 (2013).
49. Wraith, M., Uhl, J. T., Greer, J. R. & Dahmen, K. A. Slip statistics of dislocation avalanches under different loading modes. **042403,** 1–8 (2015).
50. Dimiduk, D. M., Woodward, C., Lesar, R. & Uchic, M. D. Scale-free intermittent flow in crystal plasticity. *Science* **312,** 1188–1190 (2006).
51. Sethna, J. P., Dahmen, K. A. & Myers, C. R. Crackling noise. *Nature* **410,** 242–250 (2001).
52. Fisher, D. S., Dahmen, K. & Ramanathan, S. Statistics of Earthquakes in Simple Models of Heterogeneous Faults. 4885–4888 (1997).
53. Fisher, D. S. Collective Transport: From Superconductors to Earthquakes. *Phys. Rep.* **301,** 113 (1997).
54. Kardar, M. Nonequilibrium Dynamics of Interfaces and Lines. *Phys. Rep.* **301,** 85–115 (1998).
55. Marchetti, M. C., Middleton, a. A. & Prellberg, T. Viscoelastic depinning of driven

systems: mean-field plastic scallops. *Phys. Rev. Lett.* **85,** 1104–1107 (2000).

56. Ispanovity, P. D., Groma, I., Gyorgyi, G., Szabo, P. & Hoffelner, W. Criticality of relaxation in dislocation systems. *Phys. Rev. Lett.* **107,** 1–4 (2011).
57. Miguel, M.-C., Vespignani, A., Zaiser, M. & Zapperi, S. Dislocation jamming and andrade creep. *Phys. Rev. Lett.* **89,** 165501 (2002).
58. Laurson, L., Miguel, M. C. & Alava, M. J. Dynamical correlations near dislocation jamming. *Phys. Rev. Lett.* **105,** 015501 (2010).
59. Ispanovity, P. D. *et al.* Avalanches in 2D dislocation systems: Plastic yielding is not depinning. *Phys. Rev. Lett.* **112,** 1–5 (2014).
60. Laurson, L. & Alava, M. J. Dynamic hysteresis in cyclic deformation of crystalline solids. *Phys. Rev. Lett.* **109,** 1–5 (2012).
61. Dahmen, K. a., Ben-Zion, Y. & Uhl, J. T. Micromechanical model for deformation in solids with universal predictions for stress-strain curves and slip avalanches. *Phys. Rev. Lett.* **102,** 175501 (2009).
62. Collaboration, T. L. S. *et al.* Advanced LIGO. *Class. Quantum Gravity* **32,** 74001 (2015).
63. Aasi, J. *et al.* Characterization of the LIGO detectors during their sixth science run. *Class. Quantum Gravity* **32,** 115012 (2015).
64. Abbott, B. P. *et al.* Observation of gravitational waves from a binary black hole merger. *Phys. Rev. Lett.* **116,** 1–16 (2016).
65. Aston, S. M. *et al.* Update on quadruple suspension design for Advanced LIGO. *Class. Quantum Gravity* **29,** 235004 (2012).
66. Camp, J. B., Yamamoto, H., Whitcomb, S. E. & Mcclelland, D. E. Analysis of light noise sources in a recycled Michelson interferometer with Fabry – Perot arms. *J. Opt. Soc. Am. A* **17,** 120–128 (2000).
67. Imanaka, T., Sano, K. & Shimizu, M. Dislocation Attenuation and Acoustic Emission During Deformation in Copper Single Crystals. *Cryst. Lattice Defects* **4,** 57–64 (1973).
68. Wadley, H. N. G. & Mehrabian, R. Acoustic emission for materials processing: a review. *Mater. Sci. Eng.* **65,** 245–263 (1984).
69. Heiple, C. R. & Carpenter, S. H. Acoustic emission produced by deformation of

metals and alloys - A review. *J. Acoust. Emiss.* **6,** 177–204 (1987).

70. Vinogradov, A., Patlan, V. & Hashimoto, S. Spectral analysis of acoustic emission during cyclic deformation of copper single crystals. *Philos. Mag. A Phys. Condens. Matter, Struct. Defects Mech. Prop.* **81,** (2001).
71. Weiss, J. *et al.* Evidence for universal intermittent crystal plasticity from acoustic emission and high-resolution extensometry experiments. *Phys. Rev. B - Condens. Matter Mater. Phys.* **76,** 1–8 (2007).
72. Vinogradov, A. & Yasnikov, I. S. On the nature of acoustic emission and internal friction during cyclic deformation of metals. *Acta Mater.* **70,** 8–18 (2014).
73. Weiss, J. *et al.* From Mild to Wild Fluctuations in Crystal Plasticity. **105504,** 1–5 (2015).
74. Dimiduk, D. M., Uchic, M. D. & Parthasarathy, T. A. Size-affected single-slip behavior of pure nickel microcrystals. *Acta Mater.* **53,** 4065–4077 (2005).
75. Maaß, R. & Uchic, M. D. In-situ characterization of the dislocation-structure evolution in Ni micro-pillars. *Acta Mater.* **60,** 1027–1037 (2012).
76. Cui, Y., Po, G. & Ghoniem, N. Controlling Strain Bursts and Avalanches at the Nano- to Micrometer Scale. *Phys. Rev. Lett.* **117,** 1–5 (2016).
77. Papanikolaou, S. *et al.* Quasi-periodic events in crystal plasticity and the self-organized avalanche oscillator. *Nature* **490,** 517–521 (2012).
78. Zaiser, M. Scale invariance in plastic flow of crystalline solids. *Adv. Phys.* **55,** 185–245 (2006).
79. Zaiser, M. & Moretti, P. Fluctuation phenomena in crystal plasticity - a continuum model. *J. Stat. Mech. Theory Exp.* **2005,** P08004 (2005).
80. Zaiser, M., Marmo, B. & Moretti, P. The'yielding transition'in crystal plasticity-discrete dislocations and continuum models. *Stat. Mech. Plast. Relat. Instab.* **1,** 53 (2006).
81. Ghoniem, N. M., Huang, J. & Wang, Z. Affine covariant-contravariant vector forms for the elastic field of parametric dislocations in isotropic crystals. *Philos. Mag. Lett.* **82,** 55–63 (2002).
82. Bonneville, J., Escaig, B. & Martin, J. L. A study of cross-slip activation parameters in pure copper. *Acta Metall.* **36,** 1989–2002 (1988).

83. Davis, J. R. Copper and Copper Alloys. *ASM Spec. Handb. Copp. Copp. Alloy.* 457–494 (2001). doi:10.1361/autb2001p457

84. Talamali, M., Petäjä, V., Vandembroucq, D. & Roux, S. Avalanches, precursors, and finite-size fluctuations in a mesoscopic model of amorphous plasticity. *Phys. Rev. E - Stat. Nonlinear, Soft Matter Phys.* **84,** 1–9 (2011).

85. Schütze, F. & Nattermann, T. Mean-field theory for driven domain walls in disordered environments. *Phys. Rev. B - Condens. Matter Mater. Phys.* **83,** 1–14 (2011).

86. Mughrabi, H. The cyclic hardening and saturation behaviour of copper single crystals. *Mater. Sci. Eng.* (1978). doi:10.1016/0025-5416(78)90174-X

87. Ambrosi, P., Göttler, E. & Schwink, C. On the dislocation arrangement and flow stress of [111] - copper single crystals deformed in tension. *Scr. Metall.* **8,** 1093–1097 (1974).

88. Nabarro, F. R. N. *Theory of crystal dislocations*. *International series of monographs on physics* (1967). doi:10.1063/1.3035074

89. Pine, D. J., Gollub, J. P., Brady, J. F. & Leshansky, a M. Chaos and threshold for irreversibility in sheared suspensions. *Nature* **438,** 997–1000 (2005).

90. Corté, L., Chaikin, P. M., Gollub, J. P. & Pine, D. J. Random organization in periodically driven systems. *Nat. Phys.* **4,** 420–424 (2008).

91. Regev, I., Lookman, T. & Reichhardt, C. Onset of irreversibility and chaos in amorphous solids under periodic shear. *Phys. Rev. E - Stat. Nonlinear, Soft Matter Phys.* **88,** 1–5 (2013).

92. Regev, I., Weber, J., Reichhardt, C., Dahmen, K. A. & Lookman, T. Reversibility and criticality in amorphous solids. *Nat. Commun.* **6,** 8805 (2015).

93. Fiocco, D., Foffi, G. & Sastry, S. Oscillatory athermal quasistatic deformation of a model glass. *Phys. Rev. E - Stat. Nonlinear, Soft Matter Phys.* **88,** (2013).

94. Jeanneret, R. & Bartolo, D. Geometrically protected reversibility in hydrodynamic Loschmidt-echo experiments. *Nat. Commun.* **5,** 3474 (2014).

95. Hima Nagamanasa, K., Gokhale, S., Sood, A. K. & Ganapathy, R. Experimental signatures of a nonequilibrium phase transition governing the yielding of a soft glass. *Phys. Rev. E - Stat. Nonlinear, Soft Matter Phys.* **89,** 1–7 (2014).

96. Rogers, M. C. *et al.* Echoes in x-ray speckles track nanometer-scale plastic events in colloidal gels under shear. *Phys. Rev. E - Stat. Nonlinear, Soft Matter Phys.* **90,** 1–7 (2014).

97. Möbius, R. & Heussinger, C. (Ir)reversibility in dense granular systems driven by oscillating forces. *Soft Matter* **10,** 4806–12 (2014).

98. Schreck, C. F., Hoy, R. S., Shattuck, M. D. & O'Hern, C. S. Particle-scale reversibility in athermal particulate media below jamming. *Phys. Rev. E - Stat. Nonlinear, Soft Matter Phys.* **88,** 1–9 (2013).

99. Slotterback, S. *et al.* Onset of irreversibility in cyclic shear of granular packings. *Phys. Rev. E - Stat. Nonlinear, Soft Matter Phys.* **85,** 1–5 (2012).

100. Zhou, C., Reichhardt, C. J. O., Reichhardt, C. & Beyerlein, I. Random Organization in Periodically Driven Gliding Dislocations. 1–5 (2013).

101. Marquardt, D. W. An Algorithm for Least-Squares Estimation of Nonlinear Parameters. *J. Soc. Ind. Appl. Math.* **11,** 431–441 (1963).

102. Press, W., Flannery, B., Teukolsky, S. & Vetterling, W. *Numerical Recipes. Cambridge University Press. Cambridge, NY* (1986). doi:10.2307/1269484

103. Haasen, P. & Kelly, A. A yield phenomenon in face-centered cubic single crystals. *Acta Metall.* **5,** 192–199 (1957).

104. Brown, L. M. An interpretation of the Haasen–Kelly effect. *Philos. Mag.* **90,** 4147–4152 (2010).

105. Matichard, F. *et al.* Seismic isolation of Advanced LIGO: Review of strategy, instrumentation and performance. *Class. Quantum Gravity* **32,** 185003 (2015).

106. Braccini, S. *et al.* The maraging-steel blades of the Virgo super attenuator. *Meas. Sci. Technol.* **11,** 467–476 (2000).

107. Blum, W., Eisenlohr, P. & Breutinger, F. Understanding creep-a review. *Metall. Mater. Trans. A* **33,** 291–303 (2002).

108. I.A.Bilenko, A.Yu.Ageev, V.B.Braginsky. Excess noise in the steel suspension wires for the laser gravitational wave detector. *Phys. Lett. A* **246,** 479–484 (1998).

109. Cagnoli, G. *et al.* Mechanical shot noise induced by creep in suspension devices. *Phys. Lett. A* **237,** 21–27 (1997).

110. Beccaria, M. *et al.* The creep problem in the VIRGO suspensions: A possible

solution using Maraging steel. *Nucl. Instruments Methods Phys. Res. Sect. A Accel. Spectrometers, Detect. Assoc. Equip.* **404,** 455–469 (1998).

111. Braccini, S. *et al.* Monitoring the acoustic emission of the blades of the mirror suspension for a gravitational wave interferometer. *Phys. Lett. Sect. A Gen. At. Solid State Phys.* **301,** 389–397 (2002).
112. Vajente, G. *et al.* An instrument to measure mechanical up-conversion phenomena in metals in the elastic regime. *Rev. Sci. Instrum.* **87,** (2016).
113. Staley, A. Locking the Advanced LIGO Gravitational Wave Detector : with a focus on the Arm Length Stabilization Technique. *PhD Thesis, Columbia Univ.* (2015).
114. Nip, K. H., Gardner, L., Davies, C. M. & Elghazouli, A. Y. Extremely low cycle fatigue tests on structural carbon steel and stainless steel. *J. Constr. Steel Res.* **66,** 96–110 (2010).
115. Lyons, T. T., Regehr, M. W. & Raab, F. J. Shot noise in gravitational-wave detectors with Fabry-Perot arms. *Appl. Opt.* (2000). doi:10.1364/AO.39.006761
116. Vajente, G. Crackling noise in advanced gravitational wave detectors: A model of the steel cantilevers used in the test mass suspensions. *Phys. Rev. D* **96,** 1–10 (2017).
117. Brinkman, B. A. W., Leblanc, M., Ben-Zion, Y., Uhl, J. T. & Dahmen, K. A. Probing failure susceptibilities of earthquake faults using small-quake tidal correlations. *Nat. Commun.* **6,** 1–7 (2015).

Appendix A: Exceptional Resilience of Small-Scale Shape Memory Alloys (SMA) under Cyclic Stress-Induced Phase Transformation

Shape memory alloys that produce and recover from large deformation driven by martensitic transformation are widely exploited in biomedical devices and microactuators. Generally, their actuation work degrades significantly within the first few cycles and is reduced at smaller dimensions. Further, alloys exhibiting unprecedented reversibility have relatively small superelastic strain, 0.7%. These raise the questions of whether high reversibility is necessarily accompanied by small work and strain and whether high work and strain is necessarily diminished at small scale. Here we conclusively demonstrate that these are not true by showing that Au30Cu25Zn45 pillars exhibit 12 MJ m−3 work and 3.5% superelastic strain even after 100 000 phase transformation cycles. Our findings confirm that the lattice compatibility dominates the mechanical behavior of phase-changing materials at nano to micron scales and points a way for smart microactuators design having the mutual benefits of high actuation work and long lifetime.

A.1 Introduction

By far, the most successful application of shape memory alloys (SMA) is the stent,[1,2] that is, the expandable tube used to treat narrowed or weakened arteries in the human's body. This application only requires one-time stress-induced phase transformation so that the tube can be easily squeezed into a tiny radius and stand in place after the removal of stress. There are many patents and demonstrations for nano- and microactuation applications

using SMA,[3,4] but the functional degradation of general SMA upon cyclic phase transformations [5–7] strongly hinders such applications in reality. Recent advances in shape memory alloys[8,9] show that small thermal hysteresis and high mechanical fatigue correlate closely with the satisfaction of the cofactor conditions,[10] that is, conditions on lattice parameters that enable the formation of various elastically compatible microstructures during phase trans- formation. These conditions can be achieved by doping and tuning compositional variables. Chluba et al.[9] have demonstrated a Co/Cu doped NiTi-based SMA family in which $Ti_{54}Ni_{34}Cu_{12}$ and $Ti_{54.7}Ni_{30.7}Cu_{12.3}Co_{2.3}$ thin films show ultra-low mechanical fatigue properties over millions of full transformation cycles. Compared with their nearby compositions, the lattice parameters of these alloys satisfy the cofactor conditions closely. The alloy $Ti_{54}Ni_{34}Cu_{12}$ presented nano-precipitates of Ti_2Ni.[11] These were theorized to contribute to the exceptional reversibility: the compatible austenite/marten- site interfaces that follow from the cofactor conditions[10] are also approximately parallel to the interfaces of the coherent precipitates.[11] Using a similar development strategy, the bulk SMA Au Cu Zn [8] was found to satisfy the cofactor [30 25 45] conditions for multiple twin systems. Thermal cycling tests on this alloy showed a nearly zero-migration in transition temperature and latent heat, as well as <2° thermal hysteresis for 16 000 thermal cycles. An important future application area for SMA is nano- to microscale actuation.[2,3,12] Thus, it is particularly interesting to investigate whether the formation of abundant compatible microstructures under the cofactor conditions has implications for work output and reversibility in the small-scale regime.

A.2 Sample Preparation

Previous in situ synchrotron X-ray Laue microdiffraction (μSXRD) analysis of $Au_{30}Cu_{25}Zn_{45}$ confirmed the fact that the phase transformation of this alloy between $L2_1$ austenite and the $P2_1$ martensite is not accompanied by the formation of intermetallic precipitates.[13] The lattice parameters closely satisfy the cofactor conditions for a family of ⟨100⟩ compound twins and ⟨110⟩ type I/II twins simultaneously. Quantitative characterization of microstructures at phase transformation revealed the elimination of elastic transition layers between austenite and single or multiple-twinned martensite variants.[13] In this work, we utilize the geometrically nonlinear theory of martensite and nanomechanical experiments to investigate the cyclic mechanical behavior of 1−2 μm-diameter cylindrical pillars carved from a single austenite grain of $Au_{30}Cu_{25}Zn_{45}$ plate using focused ion beam (FIB) milling. These were subject to uniaxial compressive loading. The crystallographic orientation of the resulting pillars deviated from $[001]_{L2_1}$ by 11.25°.

A.3 Nanomechanical Experiment

Two types of experiments were conducted: (1) ex situ cyclic compression tests in a nanoindenter equipped with a custom-made 8 μm diameter diamond tip (TriboIndenter, Hysitron, Inc.) and (2) in situ compression with a 2 μm diameter diamond tip built in a custom-made instrument comprised of a nanoindenter-like module (PI 85 PicoIndenter, Hysitron, Inc.) inside of a Dual Beam FIB (Versa 3D, FEI) that permits in situ video recording and imaging.

Figure 1 demonstrates the results from the cyclic compression tests conducted in the ex situ TriboIndenter on the sample with ~2 μm diameter and ~6 μm height. At each cycle 10n, n = 0, 1, 2, ... 5, the force−displacement response was acquired for a full phase transformation cycle by quasi-static displacement control, that is, load up to the elastic regime of martensite and unload down to undeformed austenite. The force−displacement data was converted to the true stress− strain curve using the procedure outlined in reference.[14] The result is shown in Figure A.1a for the first cycle (blue) and 100 000th cycle (red). The superelastic plateau strain, defined as the difference between strains at the states of martensite start/finish, and marked as Ms and Mf in Figure A.1a, is ~3.7% for cycle 1 and ~3.5% for cycle 100 000, both corresponding to about 300 MPa transformation stress. At the end of the 100 000th cycle, nearly 7% total strain at 800 MPa peak stress was completely recovered upon unloading. The scanning electron microscopy (SEM) images of post-mortem samples at the end of the first, 1000th, 10 000th, and 100 000th cycles are shown in Figure A.1b−e. These images show the formation of a thin carbon layer on the sample surfaces, typical for performing experiments in vacuum chambers of electron microscopes, which started to peel off at higher cycle numbers. No signs of permanent deformation nor structural damage of the sample were observed at any point during the experiments.

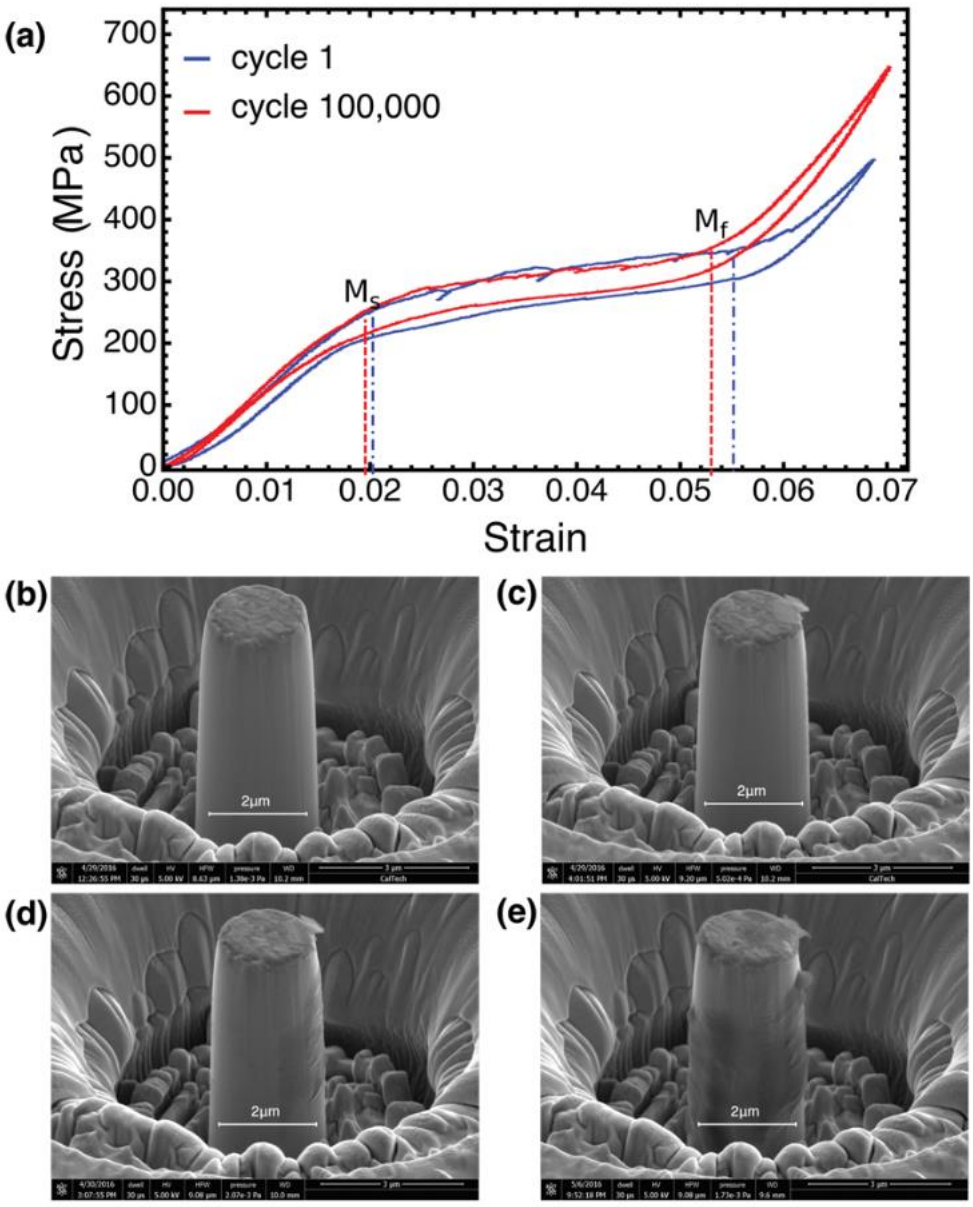

Figure A.1: $Au_{30}Cu_{25}Zn_{45}$ shape memory 2 μm diameter pillar subjected to 100000 compression-induced phase transformation cycles. (a) Stress versus strain data for the first and last cycles of the 2 μm diameter pillar. M_s and M_f mark the martensite start/finish states, respectively. (b−e) Post-mortem SEM images of the 2 μm diameter pillar after cycle 1, 1000, 10 000, and 100 000 respectively. Figure reprinted with permission from [X. Ni, et al. *Nano Lett.* 16, 12, 7621-7625]. Copyright (2017) American Chemical Society.

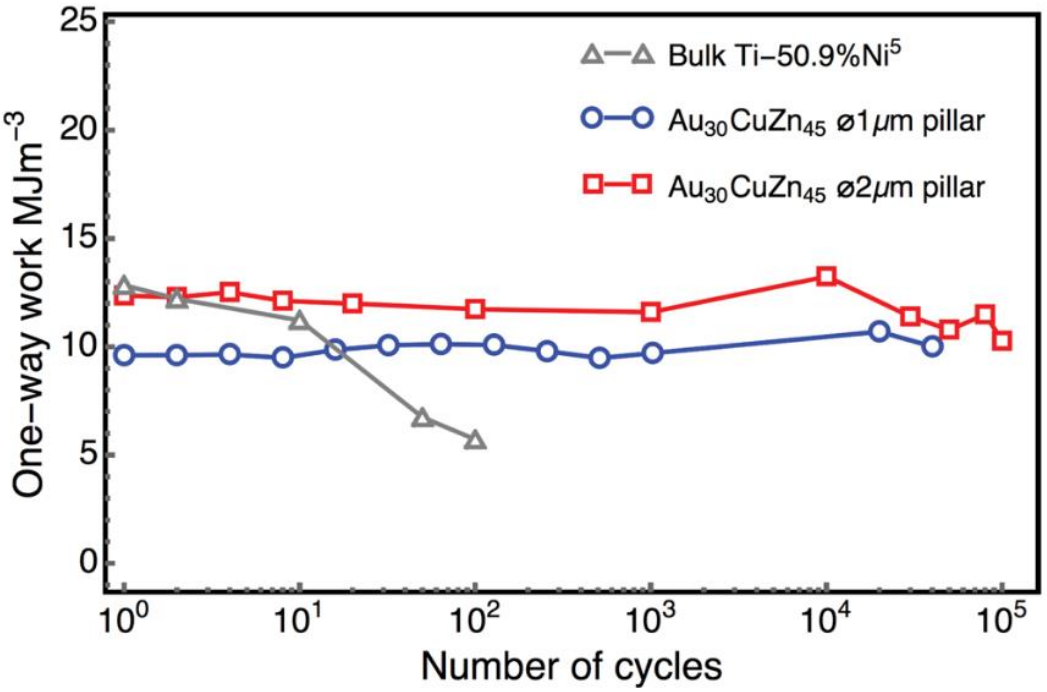

Figure A.2 Comparison of cyclic degradation between nearly equal- atomic NiTi (Miyazaki et al. (1986)5) and Au30Cu25Zn45 micrometer pillars (this work). The work is calculated using eq 1 as the area under the stress−strain curve between Ms and Mf shown in Figure A.1a. Figure reprinted with permission from [X. Ni, et al. *Nano Lett.* 16, 12, 7621-7625]. Copyright (2017) American Chemical Society.

We define the one-way work, W, as the area underneath the stress (σ)−strain (ε) curve between Ms and Mf states during the compression-induced martensitic transformation,

$$W = \int_{M_s}^{M_f} \sigma(\epsilon) d\epsilon. \quad (1)$$

Figure A.2 presents the one-way work calculated using Eq. (1) for 1 and 2 μm diameter $Au_{30}Cu_{25}Zn_{45}$ pillars of the same crystallographic orientation. It reveals a subtle size effect that the 1 μm pillar has less work than the 2 μm pillar. The average work over 100 000 cycles is ~10 MJ m^{-3} for 1 μm pillar and ~12 MJ m^{-3} for 2 μm pillar, either of which

is among the largest values of one-way work used for modern actuation systems[15−19] and is comparable to the bulk NiTi,[5,20] that is, the most successful SMA exploited for actuation systems and self- expandable stents.[2,15,17]

A.4 Results

In contrast to bulk NiTi, which at comparable stresses loses nearly half of its work within only 100 cycles,[5,21,22] these micrometer structures retain their large actuation work over 100,000 cycles. 4~5% one-way superelastic strain was also observed in some shape memory alloys such as ferromagnetic SMAs Ni_2MnX (X = In, Sn, Ga) and Cu-based SMAs; however the phase transformations in these alloys were driven in much lower stress, that is, <50 MPa[23,24] for ferromagnetic SMAs and ~100 MPa for most Cu-based SMAs.[6,16]

We have characterized the superelasticity phenomenon related to martensitic transformation by burst events, defined as sudden jumps in force−displacement response,[25] which varies from cycle to cycle in these samples. This is consistent with the irreproducibility of formation of martensite micro- structure observed in bulk.[8,13] However, the total work remained virtually the same in each cycle. Normally, in uniaxial compression experiments on martensitic pillars a single shear band with sharp re-entrant corners forms,[18,26,27] leading to strong stress concentrations. Despite of the large superelastic plateau strain delivered by the pillars studied in this work, their lateral surfaces remain smooth. Evidently, satisfaction of the cofactor conditions permits

numerous low and zero elastic energy nanostructures exhibiting quite smooth deformations even at such a small scale.

A.5 Discussion

In cubic to monoclinic transformations, there are 12 distinct martensite variants with stretch tensors relative to austenite, related by the point group of austenite ($\mathcal{P}^{24}$): $\mathcal{M} = \{U_1, \ldots, U_{12}\} = \{Q_i U Q_i^T : Q_i \in \mathcal{P}^{24}\}$.[28,29] According to energy minimization, the specific variants of martensite that form upon loading depend on the crystal orientation of the austenite micropillar and on the mechanical loading conditions. We characterized the end-surface normal of the micropillars by synchrotron Laue diffraction to be $\hat{N}$ = (0.150, −0.125, 0.981), that is, close to a high symmetry direction (0, 0, 1) with a slight angular deviation 11.25°. Such a near high symmetry orientation gives rise to four variants that approximately minimize the total free energy. If we assume that only one of these four variants nucleates and grows from the austenite in each of the loading cycles, the resultant compressive strain will be 4.7%, which corresponds to the two shear strains of 7% and 4% determined by the crystallographic equations of martensite.[28,29] However, the measured plateau strain, $M_f - M_s$ = 3.5%, in Figure A.1a is significantly lower than the compressive strain calculated from a single variant of martensite, which implies the existence of multiple martensite variants. Although a multivariant microstructure may compromise the compressive strain, it better accommodates the loading device, which tends to favor neither bending nor shear of the pillar. The satisfaction of the cofactor conditions facilitates this process by allowing for a plethora of elastically compatible austenite/twinned martensite structures.

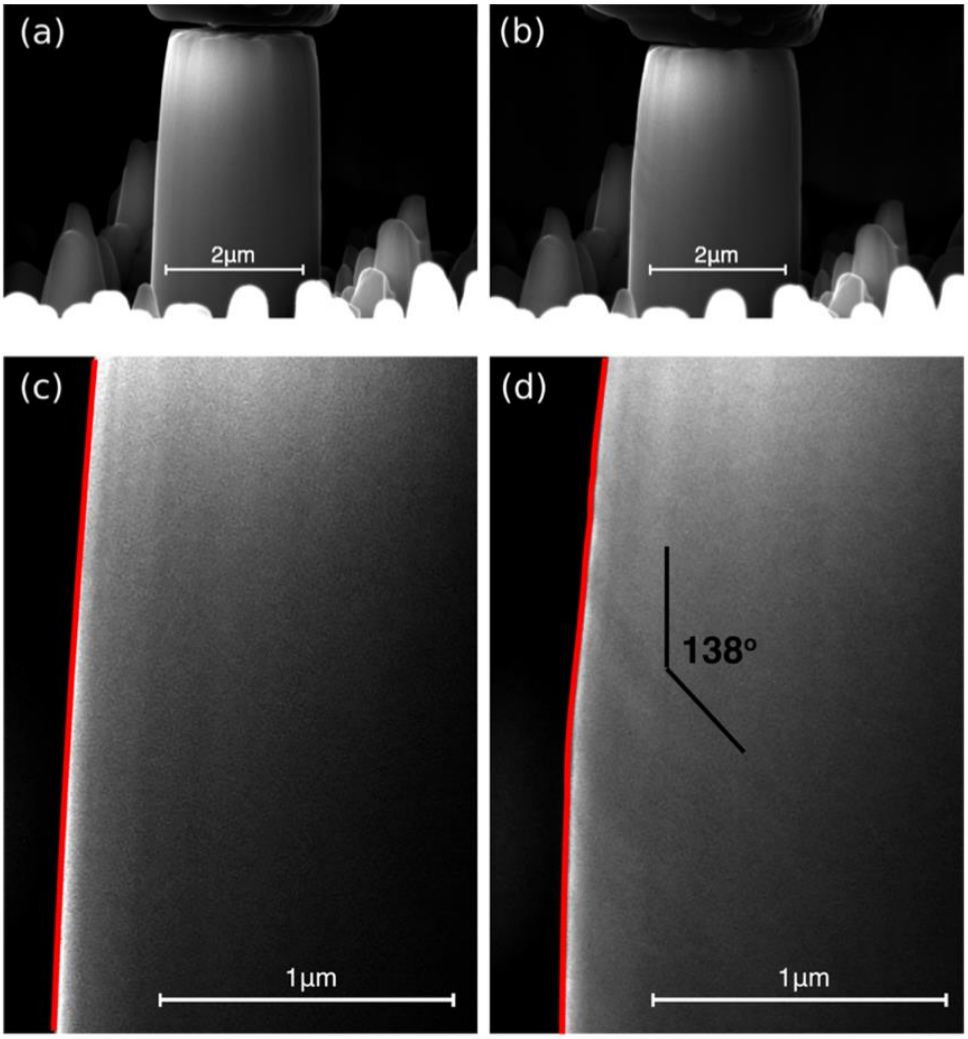

Figure A.3 SEM images of the 2 μm diameter pillar under in situ nanomechanical experiments. (a,c) The undeformed austenite phase; (b,d) the 5% strained martensite phase. Figure reprinted with permission from [X. Ni, et al. *Nano Lett.* 16, 12, 7621-7625]. Copyright (2017) American Chemical Society.

To examine this process in more detail, we utilized a custom- made in situ nanomechanical loading module to observe the formation of martensite inside the electron microscope while simultaneously performing the compression tests. Figure A.3 shows the SEM images for another ~2 μm-diameter pillar sample at 0% and 5% compressive strain. This pillar underwent a significant deformation, ~7%, including elastic deformation and phase

transformation, yet its surface remained smooth and did not exhibit large lateral shear. The SEM image in Figure A.3d, which shows parallel and unequally distributed wavy-patterns of the transformed pillar, is consistent with twinning having varying volume fractions. This microstructure is distinct from what has been observed in ordinary shape memory single-/polycrystals under uniaxial loading,[21,22,26,30] and from the microstructure of nano- and micropillars deformed plastically by the motion of dislocations.[14,31]

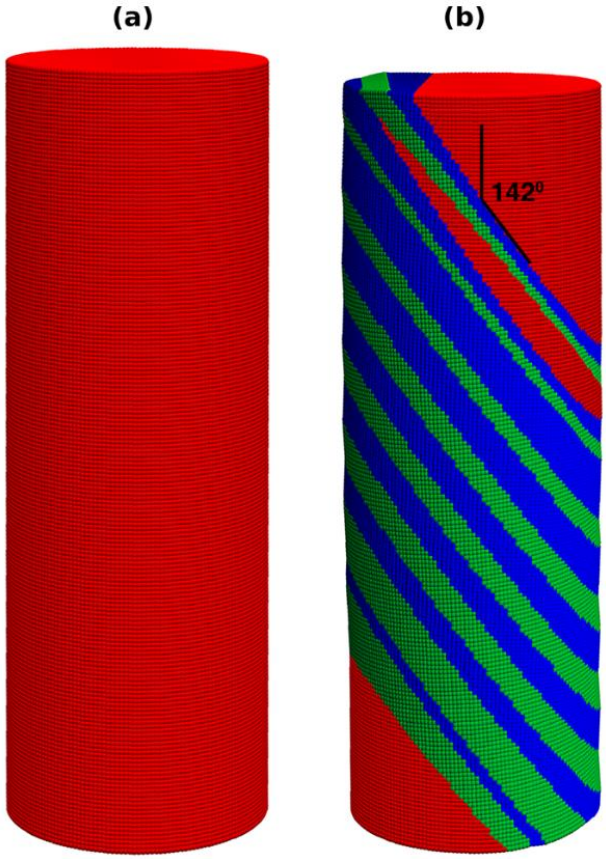

Figure A.4 Formation of microstructure under uniaxial compressive loading predicted by the geometrically nonlinear theory of martensite. (a) Undeformed austenite phase. (b) Twinned martensite satisfying the cofactor conditions subject to the uniaxial loading. Figure reprinted with permission from [X. Ni, et al. *Nano Lett.* 16, 12, 7621-7625]. Copyright (2017) American Chemical Society.

We chose the variant giving the biggest compressive strain upon loading, by which we constructed a $(10\bar{1})$ type I twin system. On the basis of the geometrically nonlinear theory of martensite,10 we postulated a homogeneous deformation that maps the austenite phase, shown in Figure A.4a, to the deformed martensite phase consisting of the $(10\bar{1})$ type I twin lamellae with varying volume fractions, shown in Figure A.4b. The average deformation gradient of a $\hat{N}$ -oriented pillar with 1:3 aspect ratio results in a 3.2% compressive strain and a 1.8% shear strain. Compared to the shear strain caused by forming a single variant, the presence of the compatible $(10\bar{1})$ type I twin reduces the shear deformation by a large margin. In addition, the calculated compressive strain agrees with the plateau strain (Figure A.1a) measured from the ex situ nanocompression experiments. The austenite and martensite interface normals are calculated from the crystallographic equation of martensite (see Supporting Information), m0 = (0.742, 0.092, −0.665) for the blue variant, and m1 = (−0.665, 0.092, 0.742) for the green variant. The formation of these twin lamellae matches the martensite morphology observed from in situ nanomechanical experiments. The angle between the trace of interface and $\hat{N}$ is ~142° shown in Figure A.4b, compared to the angle ~138° measured from the SEM image in Figure A.3d. Under the cofactor conditions satisfied by this alloy, it is possible to have untwinned austenite/martensite interfaces that are nearly parallel to a family of twin boundaries that, in fact, are those favored by the Schmid law. Normally, the scale of micro- structure in a martensitic material is a consequence of the balance between the energy of stressed transition layers and the total interfacial energy on twin boundaries. However, in the microstructure calculated in Figure A.4 there are theoretically no stressed transition layers, and therefore with only the penalty of interfacial energy quite complex microstructures

are possible even below 1 μm scale. As shown in Figure A.3, these microstructures can form without sharp re-entrant corners and with volume fractions of both martensite variants and of austenite/martensite that vary smoothly with the loading condition.

A.6 Summary

In summary, the alloy $Au_{30}Cu_{25}Zn_{45}$, which closely satisfies the cofactor conditions, exhibits unprecedented levels of work and reversibility in nanomechanical experiments. The analysis suggests that this is due to the presence of numerous compatible austenite/twinned martensite structures. As a consequence, the pillar can deform pseudohomogeneously, even at micron scale, by using twinned nanostructures. The results may inspire the design of small-scale superelastic and actuation devices for which high levels of work and reversibility are particularly important.

References

(1) Flomenblit, J.; Budigina, N.; Bromberg, Y. Two way shape memory alloy medical stent. U.S. Patent 5562641 A, 1994.

(2) Zahn, J. D. In Bio-MEMS; Wang, W., Soper, S. A., Eds.; CRC Press: Boca Raton, FL, 2007; Chapter 6, pp 143−176.

(3) Busch, J. D.; Johnson, A. D. Shape-memory alloy micro-actuator. U.S. Patent 5061914 A, 1991.

(4) Kahn, H.; Huff, M. A.; Heuer, A. H. J. Micromech. Microeng. 1998, 8, 213−221.

(5) Miyazaki, S.; Imai, T.; Igo, Y.; Otsuka, K. Metall. Trans. A 1986, 17, 115−120.

(6) San Juan, J.; No, M. L.; Schuh, C. A. Adv. Mater. 2008, 20, 272− 278.

(7) Bechtold, C.; Chluba, C.; de Miranda, R. L.; Quandt, E. Appl. Phys. Lett. 2012, 101, 091903.

(8) Song, Y.; Chen, X.; Dabade, V.; Shield, T. W.; James, R. D. Nature 2013, 502, 85−88.

(9) Chluba, C.; Ge, W.; Lima de Miranda, R.; Strobel, J.; Kienle, L.; Quandt, E.; Wuttig, M. Science 2015, 348, 1004−1007.

(10) Chen, X.; Srivastava, V.; Dabade, V.; James, R. D. J. Mech. Phys. Solids 2013, 61, 2566−2587.

(11) Dankwort, T.; Strobel, J.; Chluba, C.; Ge, W.; Duppel, V.; Wuttig, M.; Quandt, E.; Kienle, L. J. Appl. Crystallogr. 2016, 49, 1009− 1015.

(12) Bhattacharya, K.; James, R. D. Science 2005, 307, 53−54.

(13) Chen, X.; Tamura, N.; MacDowell, A.; James, R. D. Appl. Phys. Lett. 2016, 108, 211902.

(14) Greer, J.; Oliver, W. C.; Nix, W. D. Acta Mater. 2005, 53, 1821− 1830.

(15) Krulevitch, P.; Lee, A. P.; Ramsey, P. B.; Trevino, J. C.; Hamilton, J.; Northrup, M. A. J. Microelectromech. Syst. 1996, 5, 270− 282.

(16) Siredey, N.; Eberhardt, A. Mater. Sci. Eng., A 2000, 290, 171− 179.

(17) Bell, D. J.; Lu, T. J.; Fleck, N. A.; Spearing, S. M. J. Micromech. Microeng. 2005, 15, S153−S164.

(18) Ibarra, A.; San Juan, J.; Bocanegra, E. H.; No, M. L. Acta Mater. 2007, 55, 4789−4798.

(19) Sutou, Y.; Omori, T.; Kainuma, R.; Ishida, K. Mater. Sci. Technol. 2008, 24, 896−901.

(20) Orgeas, L.; Favier, D. Acta Mater. 1998, 46, 5579−5591.

(21) Pelton, A. R.; Huang, G. H.; Moine, P.; Sinclair, R. Mater. Sci. Eng., A 2012, 532, 130−138.

(22) Sun, Q. P.; Li, Z. Q. Int. J. Solids Struct. 2002, 39, 3797−3809.

(23) Karaman, I.; Karaca, H. E.; Basaran, B.; Lagoudas, D. C.; Chumlyakov, Y. I.; Maier, H. J. Scr. Mater. 2006, 55, 403−406.

(24) Xu, X.; Ito, W.; Umetsu, R. Y.; Kainuma, R.; Ishida, K. Appl. Phys. Lett. 2009, 95, 181905.